9-8-2015 12:00 AM

Electromechanical coupling behavior of dielectric elastomer transducers

Jianyou Zhou, *The University of Western Ontario*

Supervisor: Liying Jiang, *The University of Western Ontario*
Joint Supervisor: Roger Khayat, *The University of Western Ontario*

A thesis submitted in partial fulfillment of the requirements for the Doctor of Philosophy degree in Mechanical and Materials Engineering

ELECTROMECHANICAL COUPLING BEHAVIOR OF DIELECTRIC ELASTOMER TRANSDUCERS

(Thesis format: Integrated Article)

by

Jianyou Zhou

Graduate Program in Engineering Science
Department of Mechanical and Materials Engineering

A thesis submitted in partial fulfillment
of the requirements for the degree of
Doctor of Philosophy

The School of Graduate and Postdoctoral Studies
The University of Western Ontario
London, Ontario, Canada

Abstract

Dielectric elastomer transducers with large deformation, high energy output, light weight and low cost have been drawing great interest from both the research and industry communities, and shown potential for versatile applications in biomimetics, dynamics, robotics and energy harvesting. However, in addition to multiple failure modes such as electrical breakdown, electromechanical instability, loss-of-tension and fatigue, the performance of dielectric elastomer transducers are also strongly influenced by the hyperelastic and viscoelastic properties of the material. Also, the interplay among these material properties and the failure modes is rather difficult to predict. Therefore, in order to provide guidelines for the optimal design of dielectric elastomer transducers, it is essential to first develop accurate and reliable models, and efficient numerical methods to investigate their performance.

First, this thesis purposes a boundary-constraint method to eliminate the electromechanical instability of dielectric elastomer actuators under voltage-control loading condition and improve their actuation deformation. Second, based on the finite-deformation viscoelasticity model, the natural frequency tuning process of viscoelastic dielectric elastomer resonators is examined in this work. It is found that the tuned natural frequency is highly affected by the material viscoelasticity. Also, it is concluded that the electrical loading rate only influences the tunable frequency range and the safe operation voltage of the resonator, but not the tuned natural frequency when the applied voltage is within the safe range. Third, with the finite-deformation viscoelasticity model, the energy conversion efficiency of dielectric elastomer generators under equi-biaxial loading is also investigated in this work. Simulation results show that increasing the maximum stretch ratio and the rate of deformation, and choosing a proper bias voltage can lead to an improvement of the energy conversion efficiency. Furthermore, the fatigue life of dielectric elastomer devices under cyclic loading is explored in this work for the first time. Simulation results have demonstrated that the energy conversion efficiency of dielectric elastomer generators is compromised by their fatigue life.

To tackle the critical challenges for the development and design of dielectric elastomers transducers, this research develops theoretical models and numerical methods that are able to capture the nonlinear electromechanical coupling, the material properties, the typical failure modes and different operating conditions of dielectric elastomer transducers. With more accurate and reliable modeling methods, this work is expected to provide a comprehensive understanding on the fundamentals and technologies of dielectric elastomer transducers and trigger more innovative and optimal design of such devices.

Keywords

Dielectric elastomer transducers, electromechanical instability, boundary constraints, electrical breakdown, viscoelasticity, frequency tuning, energy harvesting, fatigue.

Co-Authorship Statement

The following thesis contains articles that are published in technical journals as listed below. These articles are all based on the preliminary ideas from my supervisors Dr. L. Jiang and Dr. R. E. Khayat. The derivation of the formulations and the simulation work presented in these articles were performed by J. Zhou. The manuscripts of these articles were written by J. Zhou, modified and reviewed by Dr. L. Jiang and Dr. R. E. Khayat.

Chapter 2

Title: Failure analysis of a dielectric elastomer plate actuator considering boundary constraints

Authors: J. Zhou, L. Jiang and R. E. Khayat

This work is published in "Journal of intelligent Material Systems and Structures", Vol. 24, 1667-1674 (2013).

Chapter 3

Title: Electromechanical response and failure modes of a dielectric elastomer tube actuator with boundary constraints

Authors: J. Zhou, L. Jiang and R. E. Khayat

This work is published in "Smart Materials and Structures", Vol. 23, 045028 (2014).

Chapter 4

Title: Viscoelastic effects on frequency tuning of a dielectric elastomer membrane resonator

Authors: J. Zhou, L. Jiang and R. E. Khayat

This work is published in "Journal of Applied Physics", Vol. 115, 124106 (2014).

Chapter 5

Title: Investigation on the performance of a viscoelastic dielectric elastomer membrane generator

Authors: J. Zhou, L. Jiang and R. E. Khayat

This work is published in “Softer Matter” Vol. 11, 2983-2992 (2015).

Acknowledgments

First and foremost, I would like to thank the entire UWO community and excellent faculty and staffs. I would also like to express my sincere gratitude to my supervisors Professor Jiang and Professor Khayat, for the opportunity to work on this project, for valuable discussions, as well as for their patient guidance. Their wisdom has taught me a lot about research and life.

Appreciation is also expressed to the following: Professor Asokanthan and Professor Klassen, for their valuable advices on the project. All my colleagues, for their help and friendship. Natural Sciences and Engineering Research Council of Canada (NSERC), for the financial support.

I would also like to thank my parents, my brother, all my friends and an important person, Wei.

Table of Contents

List of Figures

Nomenclature

c=	voltage
E	electric field
Q	electric charges
£$_0$	permittivity of air or vacuum
£	relative dielectric constant
W_s	elastic strain energy density function
G	shear modulus
J_{lim}	stretching limit of the material
c*	dimensionless voltage
E_B	dielectric strength
c$_B$	electrical breakdown voltage
E_Y	Young’s modulus
¬	Poisson’s ratio
k_c	buckling coefficient
V	electric potential
D	electric displacement
$\mathbf{F}$	deformation gradient
$\mathbf{F}^e$	elastic deformation gradient
$\mathbf{F}^i$	inelastic deformation gradient
G_f	total free energy
W	Helmholtz free energy density
W^{EQ}	equilibrium Helmholtz free energy density
W^{NEQ}	non-equilibrium Helmholtz free energy density
°	density of the material
G^{EQ}	equilibrium shear modulus
G^{NEQ}	non-equilibrium shear modulus
$\mathbf{I}$	second order identity tensor
$\mathbf{I}^4$	fourth order symmetric identity tensor
¥$^{-1}$	isotropic rank-four mobility tensor

¦ $_{v}$	shear viscosity
²=	viscoelastic relaxation time
μ_n	natural frequency
t_n	dimensionless natural frequency
c_L	voltage of the power supply
c_H	voltage of the harvesting capacitor
C	capacitance
ΔE_{m}	consumed mechanical energy
ΔE_{e}	harvested electrical energy
a	equi-biaxial stretch ratio
¦	efficiency of the generator
N_{f}	number of cycles of the fatigue life

Chapter 1

1 Introduction

1.1 Dielectric elastomers

Dielectrics are insulating materials that can be polarized when subject to an electric field. As a category of dielectrics, dielectric elastomers (DEs) are soft electroactive materials that can be developed as electromechanical transducers and convert energy from one form to another. When acting in the actuator mode, DEs transduce electrical energy to mechanical energy, while they can also convert (mechanical energy to electrical energy in a reverse mode, i.e., generator mode). Crosslinked above the glass transition temperature of polymer materials, dielectric elastomers have lower shear moduli (a few kilopascal) and are more mechanically compliant compared with the stiff or hard dielectrics with moduli of a few gigapascal and achievable strains typically less than 1% (like piezoelectric crystals and ceramics) (Carpi *et al*., 2008; Saito *et al*., 2004). Under an applied voltage, DEs are capable of undergoing large voltage-induced deformation over 100% (Pelrine *et al*., 2000). Due to their large deformation capability, high energy density, softness and flexibility, DEs have been developed and explored for applications such as artificial muscles, programmable haptic surfaces, conformal loudspeakers, energy harvesters, tunable lens, soft robots, sensors of force and pressure, active noise control devices, oscillators, resonators and adaptive optical elements (Carpi *et al*., 2008; Heydt *et al*., 2006; Huang *et al*., 2013; Karsten *et al*., 2013; Kornbluh *et al*., 2002; McKay *et al*., 2010; O'Halloran *et al*., 2008; Pelrine *et al*., 2002).

As shown in Figure 1.1, the basic element of a DE-based transducer is a dielectric elastomer membrane coated with two compliant electrodes on its two surfaces. When subject to a voltage c, most of opposite charges from the power source accumulate on the compliant electrodes while part of them leak through the membrane due to the defects or impurities in the elastomer. The opposite charges accumulating on the electrodes induce an electric field and polarize the electric charges in the DE, which then induces attractive electrostatic forces that make the DE membrane contract along thickness and expands in area. Depending on particular device applications, the basic element of a DE transducer shown in Figure 1.1 can be further developed into different configurations such as tube, plate, stacks, extenders, roll, bimorphs, unimorphs, etc (see Figure 1.2) (Kornbluh *et al*., 2002; Pei *et al*., 2004; Carpi *et al*., 2007; Cameron *et al*., 2008; Ahmadi *et al*., 2013; Biggs *et al*., 2010).

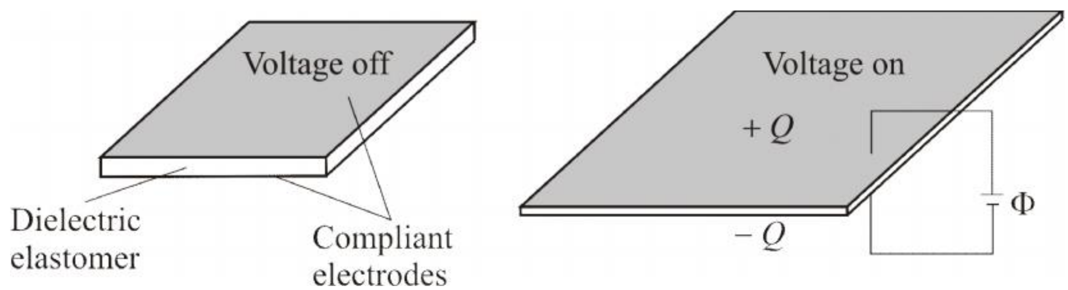

Figure 1.1 Actuation of a dielectric elastomer.

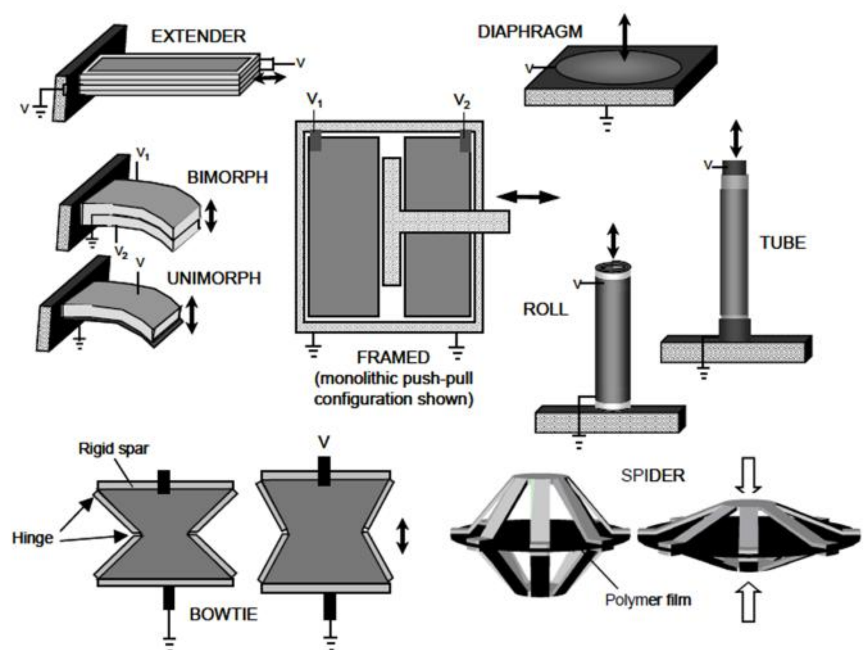

Figure 1.2 Dielectric elastomers in different configurations (Kornbluh et al., 2002).

1.2 Large deformation capability and typical failure modes of dielectric elastomers

Among the merits of DEs, their large-deformation capability draws most interest from the research communities and shows promise for various applications. However, it has been found that the voltage-induced deformation of DEs is strongly affected by multiple failure modes (Pelrine *et al*., 1998; Kofod *et al*., 2003; Plante and Dubowsky 2006; Wissler *et al*., 2007). In addition to the material rapture, the actuation of DEs is also limited by electrical breakdown (EB) failure like any other dielectric materials (Huang *et al*., 2012a; Plante and Dubowsky 2006). Electrical breakdown occurs when the electric field induced by the applied voltage exceeds the dielectric strength of the material. In fact, determining the dielectric strength of DEs has always been challenging since experiments have shown that they are influenced by quite a few factors. Huang *et al.* (2012a) and Gatti *et al.* (2013) observed that the dielectric strength of DEs monotonically increased with the increasing stretch ratio while decreased with the increasing thickness. Sheng *et al*. (2012) found that the dielectric constant of DEs is non-monotonic to the temperature. Also, Trols *et al.* (2013) reported that even the configuration of the electrodes on the DEs and the loading rate of the applied voltage have an significant effect on the dielectric strength of DEs. Since the mechanisms behind these phenomena are still not well understood, a constant dielectric strength is commonly assumed in the theoretical analysis on DEs.

As shown in Figure 1.1, the compliant electrodes coated on the DE membrane exert no constraint to both the top and bottom surfaces. When an electric voltage is applied to the electrodes, the induced electric field along the thickness direction forces the unconstrained DE membrane to contract in thickness and stretch in area. The thickness reduction of the DE membrane in turn causes a higher electric field under the same applied voltage, resulting in a higher attractive electrostatic force to further thin down the DE membrane. At a particular level of the applied voltage, this feedback mechanism may lead to excessive thinning of the DE and result in the electromechanical instability (EMI) (or pull-in instability) (Plante and Dubowsky 2006; Keplinger *et al*., 2012). Depending on the dielectric strength of the DE, this excessive thinning may cause a premature electrical breakdown, or result in a desirable large deformation. To illustrate this phenomenon, Figure 1.3 (Koh *et al*., 2011) shows a typical electromechanical response curve (the applied voltage c versus the equi-biaxial stretch ratio a) and an electrical breakdown curve (the electrical breakdown voltage c_B versus a) of a DE membrane under a monotonically increasing voltage. As the stretch ratio increases, the applied voltage first increases, reaches a peak (the onset of EMI), then drops to a trough and dramatically rises when the DE is close to its extensibility. On the contrary, the electrical breakdown curve is monotonic to the stretch ratio. Thus there are three possibilities for the interaction of these two curves. In Figure 1.3(a), as the applied voltage reaches the level of the breakdown voltage (the intersection point) before the peak, the actuation of DE fails by the electrical breakdown. For Figure 1.3(b) and (c), the applied voltage reaches the peak before the electrical breakdown occurs. Right after the peak, the stretch ratio snaps to the other side of response curve (dotted arrow) since the interval between the peak and trough is proven to be unstable by a perturbation analysis (Leng *et al*., 2009; Huang and Suo, 2011). This snap-through behavior indicates the EMI of DEs. A premature electrical breakdown occurs if the snap-through intersects with the electrical breakdown curve (Figure 1.3(b)), while the actuation survives the EMI if the snap-through does not intersect with the electrical breakdown curve (Figure 1.3(c)), leading to large deformation of the DE. According to the intersection point between the electromechanical response curve and the electrical breakdown curve, Zhao and Suo (2010), and Koh *et al*. (2011) categorized DEs into three types: (I) for DEs with low dielectric strength, EB occurs before the EMI and only small deformation of DEs can be achieved; (II) for DEs with medium dielectric strength, EMI occurs first and leads to a premature EB; (III) for DEs with exceptional high dielectric strength, EMI occurs first but does not result in a premature EB, in which case large deformation of the DE is achieved.

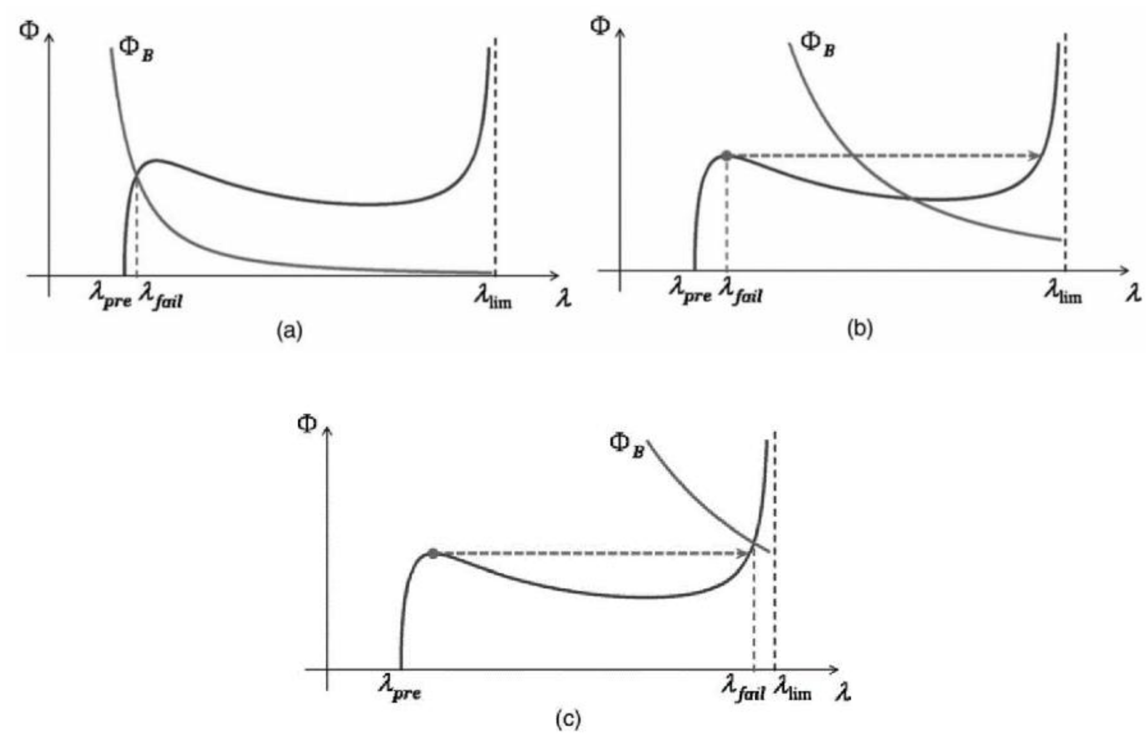

Figure 1.3 Electromechanical response and electrical breakdown of a DE membrane. The DEs are categorized into three groups based on the intersection point of the electromechanical response curve and the electrical breakdown curve: (a) Type I; (b) Type II; (c) Type III (Koh *et al*., 2011).

Since the merit of dielectric elastomers mainly lies in their capability of undergoing large deformation, much effort has been devoted to tackling the EMI for improving the actuation performance, or even harnessing the EMI for giant voltage-induced deformation of DEs. For example, Pelrine *et al*. (2000) improved the in-plane actuation strain of a DE plate from about 30% (Kornbluh *et al*., 1999) to over 100% by pre-stretching the elastomer. Later, Koh *et al*. (2011) theoretically proved that the EMI of DEs could be eliminated by the application of pre-stretch. Lu *et al*. (2012) and Huang *et al*. (2012b) found that dielectric elastomers reinforced by stiff fibers do not exhibit EMI. Kollosche *et al*. (2012) demonstrated that clamping the elastomer along one direction can also eliminate the EMI. Researchers also managed to switch a DE from Type II to Type III by swelling the elastomer with a solvent and harness the EMI to achieve large deformation of the DE (Shankar *et al.*, 2007). Alternatively, actuation strains of DEs over

100% have been attained by using elastomers with interpenetrating networks (Ha *et al.*, 2006) and by using electrode-free elastomers with sprayed-on charges (Keplinger *et al*., 2010). However, these methods are either limited to some particular applications or difficult to implement. Therefore, there is still much room for seeking alternatives to improve the actuation strains of DEs.

Furthermore, in addition to the hyperelastic behavior (large deformation), DEs are also known to exhibit viscoelastic properties (Zhang *et al*., 2004; Plante and Dubowsky, 2007; Bai *et al*., 2014; Kollosche *et al*., 2015), which may induce other failure modes depending on particular applications of DEs. Take DE membrane oscillators and resonators for example, the material viscoelasticity of DEs not only strongly affect their dynamic performance but can also cause loss-of-tension of the DE membrane (Li *et al*., 2012). Also, for DE membrane energy harvesters, both the loss-of-tension failure and the fatigue failure should be examined since the viscoelastic DE membranes are under cyclic loading condition. However, compared to the works on DE actuators, much less studies are available in the literature for DE oscillators and energy harvesters, especially investigation of the influence of the material viscoelasticity on the performance of these DE devices. Therefore, there is a lack of guidance available for the optimal design of these devices.

1.3 Objectives

As introduced above, due to the large-deformation and energy transduction capability, DEs have shown promise for a number of potential applications. However, the nonlinear electromechanical response of DEs is rather complicated and strongly affected by the typical failure modes and the material properties such as viscoelasticity. Moreover, for different DE-based devices, other particular issues depending on the applications could make it more difficult to manage the performance of such devices. Therefore, objective of this work is to provide a comprehensive understanding on the performance of DEs and guidelines to the optimal design of DE-based devices. Attention will be focused on:

(1) Examining the nonlinear electromechanical response of DE actuators with different configurations and uncovering possible alternatives to eliminate EMI of the DE actuators while attaining large deformation;

(2) Studying the dynamic behavior of viscoelastic DEs and developing theoretical models that can make reliable prediction on the frequency tuning and dynamic response of DE-based resonators and oscillators;

(3) Investigating the energy harvesting performance of dissipative DEs and developing possible approaches to improve the energy harvesting efficiency of DE-based generators.

1.5 Thesis Structure

Following the general introduction and objectives in Chapter 1, a literature review is given in Chapter 2. Then the nonlinear electromechanical response of a DE plate actuator with and without boundary constraints is modelled and a boundary-constraint method to eliminate EMI is proposed in Chapter 3. In Chapter 4, the boundary-constraint method is further verified on a constrained DE tube actuator. In the second half of this thesis, modeling work is further developed to cover the dynamic and viscoelastic effects of the DEs. In Chapter 5, based on the finite-deformation viscoelasticity theory, the in-plane oscillation of viscoelastic DE membrane resonator and its natural frequency tuning process is investigated. In Chapter 6, by examining the energy harvesting performance of a dissipative DE membrane generator, the effect of fatigue on DE-based devices under cyclic loading is investigated for the first time and uncover possible approaches to improve the efficiency of DE generators. Last but not least, Chapter 7 summarizes the thesis and suggests avenue for the future work on the modeling of DEs and DE-based devices.

References

Ahmadi, S., Gooyers, M., Soleimani, M. and Menon, C., 2013. Fabrication and electromechanical examination of a spherical dielectric elastomer actuator. Smart Mater. Struct. **22**, 115004.

Bai, Y., Jiang, Y., Chen, B., Foo, C. C., Zhou, Y., Xiang, F., Zhou, J., Wang, H. and Suo, Z., 2014. Cyclic performance of viscoelastic dielectric elastomers with solid hydrogel electrodes. Appl. Phys. Lett. **104**, 062902.

Biggs, S. J. and Hitchcock, R. N., 2010. Artificial muscle actuators for haptic displays: system design to match the dynamics and tactile sensitivity of the human fingerpad. Proc. SPIE **7642**, 76420I.

Cameron, C. G., Szabo, J. P., Johnstone, S., Massey, J. and Leidner, J., 2008. Linear actuation in coextruded dielectric elastomer tubes. Sens. Actuator A **147**, 286–291.

Carpi, F., Rossi, D. D., Kornbluh, R., Pelrine, R. and Sommer-Larsen, P., 2008. Dielectric Elatomers as Electromechanical Transducers. Elsevier, Amsterdam.

Carpi, F., Salaris, C. and Rossi, D. D., 2007. Folded dielectric elastomer actuators. Smart Mater. Struct. **16**, S300–305.

Gatti, D., Haus, H., Matysek, M., Frohnapfel, B., Tropea, C. and Schlaak, H. F., 2014. The dielectric breakdown limit of silicone dielectric elastomer actuators. Appl. Phys. Lett. **104**, 052905.

Ha, S. M., Yuan, W., Pei, Q., Pelrine, R. and Stanford, S., 2006. Interpenetrating polymer networks for high-performance electroelastomer artificial muscles. Adv. Mater. **18**, 887–891.

Heydt, R., Kornbluh, R., Eckerle, J. and Pelrine, R., 2006. Sound radiation properties of dielectric elastomer electroactive polymer loadspeakers. Proc. SPIE **6168**, 61681M.

Huang, J., Shian, S., Diebold, R. M., Suo, Z. and Clarke, D. R., 2012a. The thickness and stretch dependence of the electrical breakdown strength of an acrylic dielectric elastomer. Appl. Phys. Lett. **101**, 122905.

Huang, J., Lu, T., Zhu, J., Clarke, D. R. and Suo, Z., 2012b. Large, uni-directional actuation in dielectric elastomers achieved by fiber stiffening. Appl. Phys. Lett. **100**, 211901.

Huang, J., Shian, S., Suo, Z. and Clarke, D. R., 2013. Maximizing the energy density of dielectric elastomer generators using equi-biaxial laoding. Adv. Funct. Mater. **23**, 5056-5061.

Huang, R. and Suo, Z., 2011. Electromechanical phase transition in dielectric elastomers. Proc. R. Soc. A **468**, 1014–1040.

Karsten, R., Flittner, K., Haus, H. and Schlaak, H. F., 2013. Development of an active isolation mat based on dielectric elastomer stack actuators for mechanical vibration cancellation. Proc. SPIE **8687**, 86870Y.

Keplinger, C., Kaltenbrunner, M., Arnold, N. and Bauer, S., 2010. Rontgen's electrode-free elastomer actuators without electromechanical pull-in instability. Proc. Natl. Acad. Sci. USA **107**, 4505-4510.

Keplinger, C., Li T., Baumgartner, R., Suo Z. and Bauer, S., 2012 Harnessing snap-through instability in soft dielectrics to achieve giant voltage-triggered deformation. Soft Matter **8**, 285-288.

Kofod, G., Sommer-Larsen, P., Kornbluh, R. and Pelrine, R., 2003. Actuation response of polyacrylate dielectric elastomers. J. Intell. Mater. Syst. Struct. **24**, 1667–1674.

Koh, S. J. A., Li, T., Zhou, J., Zhao, X., Hong, W., Zhu, J. and Suo, Z., 2011. Mechanisms of large actuation strain in dielectric elastomers. J. Polym. Sci. B **49**, 504–515.

Kollosche, M., Kofod, G., Suo, Z. and Zhu, J., 2015. Temporal evolution and instability in a viscoelastic dielectric elastomer. J. Mech. Phys. Solids **76**, 47-64.

Kollosche, M., Zhu, J., Suo, Z. and Kofod, G., 2012. Complex interplay of nonlinear processes in dielectric elastomers. Phys. Rev. E **85**, 051801.

Kornbluh, R., Pelrine, R., Joseph, J, Heydt, R., Pei, Q. and Chiba, S., 1999. High-field electrostriction of elastomeric polymer dielectrics for actuation. Proc. SPIE **3669**, 149–161.

Kornbluh, R., Pelrine, R., Pei, Q., Heydt, R., Stanford, S., Oh, S. and Eckerle, J., 2002. Electroelastomers: applications of dielectric elastomer transducers for actuation, generation and smart structures. Proc. SPIE **4698**, 254–270.

Li, T., Qu, S. and Yang, W., 2012. Electromechanical and dynamic analyses of tunable dielectric elastomer resonator. Int. J. Solids Struct. **49**, 3754-3761.

Leng, J., Liu, L., Liu, Y., Yu, Kai. And Sun, S., 2009. Electromechanical stability of dielectric elastomer. Appl. Phys. Lett. **94**, 211901.

Lu, T., Huang, J., Jordi, C., Kovacs, G., Huang, R., Clarke, D. R. and Suo, Z., 2012. Dielectric elastomer actuators under equal-biaxial forces, uniaxial forces, and uniaxial constraint of stiff fibers. Soft Matter **8**, 6167–6173.

McKay, T., O'Brien, B., Calius, E. and Anderson, I., 2010. An integrated, self-priming dielectric elastomer generator. Appl. Phys. Lett. **97**, 062911.

O'Halloran, A., O'Malley, F. and McHugh, P., 2008. A review on dielectric elastomer actuators, technology, applications and challenges. J. Appl. Phys. **104**, 071101.

Pei, Q., Rosenthal, M., Stanford, S., Prahlad, H. and Pelrine, R., 2004. Multiple-degrees-of-freedom electroelastomer roll actuators. Smart Mater. Struct. **13**, N86–92.

Pelrine, R. E., Kornbluh, R. D. and Joseph, J. P., 1998. Electrostriction of polymer dielectrics with compliant electrodes as a means of actuation. Sens. Actuators A **64**, 77-85.

Pelrine, R., Kornbluh, R., Pei, Q. and Joseph, J., 2000. High-speed electrically actuated elastomers with greater than 100%. Science **287**, 836-839.

Pelrine, R., Kornbluh, R.D., Pei, Q., Stanford, S., Oh, S., Eckerle, J., Full, R., Rosenthal, M. and Meijer, K., 2002. Dielectric elastomer artificial muscle actuators: toward biomimetic motion. Proc. SPIE **4695**, 126-137.

Plante, J. and Dubowsky, S., 2006. Large-scale failure modes of dielectric elastomer actuators. Int. J. Solids Struct. **43**, 7727-7751.

Plante, J. and Dubowsky, S., 2007. On the performance mechanisms of dielectric elastomer actuators. Sens. Actuators A **137**, 96-109.

Saito, Y., Takao, H., Tani, T., Nonoyama, T., Takatori, K., Homma, T., Nagaya, T. and Nakamura M., 2004. Lead-free piezoceramics. Nature **432**, 84-87.

Shankar, R., Ghosh, T. K. and Spontak, R.J., 2007. Electroactive nanostructured polymers as tunable actuators. Adv. Mater. **19**, 2218-2223.

Sheng, J., Chen, H., Li B. and Chang, L., 2013. Temperature dependence of the dielectric constant of acrylic dielectric elastomer. Appl. Phys. A **110**, 511-515.

Trols, A., Kogler, A., Baumgartner, R., Kaltseis, R., Keplinger, C., Schwodiauer, R., Graz, I. and Bauer, S., 2013. Stretch dependence of the electrical breakdown strength and dielectric constant of dielectric elastomers. Smart Mater. Struct. **22**, 104012.

Wissler, M. and Mazza, E., 2007. Mechanical behavior of an acrylic elastomer used in dielectric elastomer actuators. Sens. Actuators A **134**, 494-504.

Zhang, X. Q., Wissler, M., Jaehne, B., Broennimann, R. and Kovacs, G., 2004. Effects of crosslinking, prestrain and dielectric filler on the electromechanical response of a new silicone and comparison with acrylic elastomer. Proc. SPIE, **5385**, 78-86.

Zhao, X. and Suo, Z., 2010. Theory of dielectric elastomers capable of giant deformation of actuation. Phys. Rev. Lett. **104**, 178302.

Chapter 2

2 Literature review

In order to predict the performance of DEs and DE-based transducers, and provide guidelines for their optimal design, over a decade, extensive studies have been devoted to investigating the electromechanical response of the DEs, and the complex interplay among the electromechanical response, the typical failure modes, the dynamic behavior and the material properties of DEs. This section presents a review of literature on the modeling of the nonlinear electromechanical response, the dynamic behavior and the finite-deformation viscoelasticity of the DEs.

2.1 Electromechanical coupling of dielectric elastomers

The first model to describe the voltage-induced Maxwell stresses in dielectric elastomers was developed by Pelrine *et al.* (1998), which expresses the Maxwell stresses with an equivalent Maxwell pressure $P = ££_0E^2$, where £ is the dielectric constant, $£_0$ is the permittivity of free space, and E is the voltage-induced electric field. This Maxwell pressure is then considered to be balanced by the local elastic stress of the elastomer, which is assumed to be linear to the strain of the elastomer (Pelrine *et al*., 1998; Kornbluh *et al.*, 1999). Nevertheless, based on linear elasticity, this model is only rather accurate for small-deformation cases, whereas it is inadequate to tackle the large deformation and significant nonlinear behavior of the DEs. To account for the nonlinear electromechanical response of the DEs, hyperelasticity theories with the addition of an empirical Maxwell stress were adopted in the later studies. For example, Goulbourne *et al.* (2005) proposed a nonlinear model for dielectric elastomer membranes, in which the local elastic stress was derived from a mechanical strain energy density function. Considering uniform DEs (isotropic, incompressible and homogeneous), Wissler and Mazza (2005) modeled the electromechanical response of a pre-strained circular DE actuator with the local elastic stress derived from different hyperelastic models. However, the models proposed in these works can only explain some experimental phenomena, leaving many issues unsettled. Later, with the development of the fully coupled field theories for dielectric elastomers

(McMeeking and Landis, 2005; Dorfmann and Ogden, 2005; Suo *et al.*, 2008) which obtain the Cauchy stress from a coupled free energy density function associated with both the strain and the polarization, and are capable of adopting most of the hyperelastic constitutive models (Ogden, 1972; Gent, 1996; Boyce and Arruda, 2000), the nonlinear electromechanical response and electromechanical coupling behavior of the DEs were further studied and better understood.

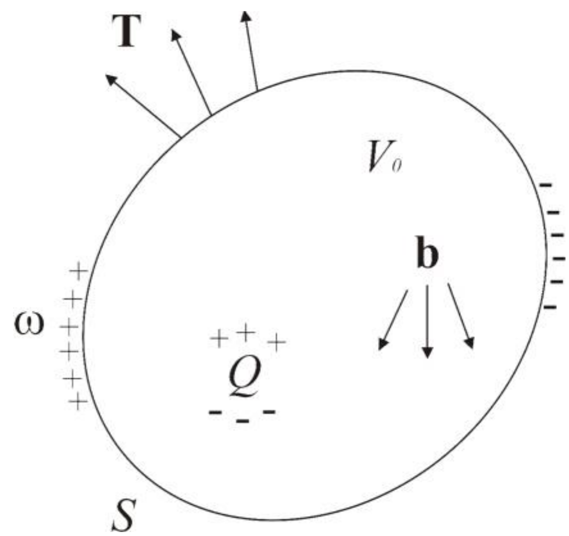

Figure 2.1 A dielectric body with free charges subject to body forces and surface tractions

With the fully coupled field theories, two main difficulties (First, unlike the electric force in a vacuum, force between electric charges inside a dielectric solid is not a measurable quantity. Second, to make a unique distinction between the deformation caused by the electrical forces and that caused by the mechanical forces is a difficult matter) of modeling deformable dielectrics can be circumvented. Figure 2.1 illustrates a dielectric body with free charges subject to body forces $\mathbf{b}(\mathbf{X}, t)$ and surfaces tractions $\mathbf{T}(\mathbf{X}, t)$ in the current state, where $\mathbf{x}$ is the positon of a material particle in the dielectric body in the current state and $\mathbf{X}$ is its position in the reference (undeformed) state. The dielectric body occupies a volume V_0 and is surrounded by a surface S. The free charge per unit volume within V_0 is denoted as $Q(\mathbf{X}, t)$ and the free charge per unit area on surface S is denoted as $\mu(\mathbf{X}, t)$. Also the electric potential of the material particle is denoted as $V(\mathbf{X}, t)$. The deformation gradient tensor of the current state with respect to the reference state is defined as

$$F_{\mathrm{ik}} = \frac{\partial x_{\mathrm{i}}}{\partial X_{\mathrm{k}}} . \tag{2.1}$$

Considering any test functions $\P_{\mathrm{i}}(\mathbf{X})$ and $\text{¦}(\mathbf{X})$,

$$\int_V \frac{\partial \P_{\mathrm{i}}}{\partial X_{\mathrm{k}}} s_{\mathrm{ik}} dV_0 = \int_S T_{\mathrm{i}} \P_{\mathrm{i}} dS - \int_V \P_{\mathrm{i}} \frac{\partial s_{\mathrm{ik}}}{\partial X_{\mathrm{k}}} dV_0 , \tag{2.2}$$

$$\int_V \frac{\partial \text{¦}}{\partial X_{\mathrm{k}}} \tilde{D}_{\mathrm{k}} dV_0 = -\int_S \mu \text{¦} dS - \int_V \text{¦} \frac{\partial \tilde{D}_{\mathrm{k}}}{\partial X_{\mathrm{k}}} dV_0 , \tag{2.3}$$

where s_{ik} is the first Piola-Kirchhoff stress (nominal stress) and $\tilde{D}_{\mathrm{k}}$ is nominal electric displacement. The equilibrium equation of the current state is expressed as

$$\frac{\partial s_{\mathrm{ik}}}{\partial X_{\mathrm{k}}} + b_{\mathrm{i}} = 0 . \tag{2.4}$$

Combining equations (2.2) and (2.4),

$$\int_V \frac{\partial \P_{\mathrm{i}}}{\partial X_{\mathrm{k}}} s_{\mathrm{ik}} dV_0 = \int_S T_{\mathrm{i}} \P_{\mathrm{i}} dS + \int_V \P_{\mathrm{i}} b_{\mathrm{i}} dV_0 . \tag{2.5}$$

According to Maxwell’s laws, the electric field must be curl-free, which leads to

$$\tilde{E}_{\mathrm{k}} = -\frac{\partial V}{\partial X_{\mathrm{k}}} , \tag{2.6}$$

where $\tilde{E}_{\mathrm{k}}$ is the nominal electric field. According to Gauss's law, the divergence of the electric displacement is equal to the free charge per unit volume, which results in

$$\frac{\partial \tilde{D}_{\mathrm{k}}}{\partial X_{\mathrm{k}}} = Q\,. \tag{2.7}$$

Combining equations (2.3) and (2.7) results in,

$$\int_V \frac{\partial \text{¦}}{\partial X_{\mathrm{k}}} \tilde{D}_{\mathrm{k}} dV_0 = -\int_S \text{µ}\,\text{¦}\, dS - \int_V \text{¦}\, Q dV_0\,. \tag{2.8}$$

When subject to a perturbation, the change of the total free energy of the dielectric body in the current state caused by the small changes of the deformation and the free charges is expressed as

$$\delta G_{\mathrm{f}} = \int_V \delta W dV_0 - \int_V b_{\mathrm{i}} \delta x_{\mathrm{i}} dV_0 - \int_S T_{\mathrm{i}} \delta x_{\mathrm{i}} dS - \int_V \delta Q V dV_0 - \int_S \delta \text{µ} V dS\,, \tag{2.9}$$

where G_{f} is the total free energy and $W(\mathbf{F}, \tilde{\mathbf{D}})$ is the Helmholtz free energy density. In equation (2.9), δx_{i} and V can be considered as two test functions $\text{¶}_{\mathrm{i}}(\mathbf{X})$ and $\text{¦}(\mathbf{X})$ in equations (2.5) and (2.8), respectively, which further results in

$$\text{¢} G_{\mathrm{f}} = \int_V \text{¢} W dV_0 - \int_V \text{¢} F_{\mathrm{ik}} s_{\mathrm{ik}} dV_0 - \int_V \tilde{E}_{\mathrm{k}} \text{¢} \tilde{D}_{\mathrm{k}} dV_0\,. \tag{2.10}$$

Since $\text{¢} W = \frac{\partial W}{\partial F_{\mathrm{ik}}} \text{¢} F_{\mathrm{ik}} + \frac{\partial W}{\partial \tilde{D}_{\mathrm{k}}} \text{¢} \tilde{D}_{\mathrm{k}}$, equation (2.10) can be re-written as

$$\text{¢} G_{\mathrm{f}} = \int \left(\frac{\partial W}{\partial F_{\mathrm{ik}}} - s_{\mathrm{ik}} \right) \text{¢} F_{\mathrm{ik}} dV_0 + \int \left(\frac{\partial W}{\partial \tilde{D}_{\mathrm{k}}} - \tilde{E}_{\mathrm{k}} \right) \text{¢} \tilde{D}_{\mathrm{k}} dV_0\,, \tag{2.11}$$

which gives that

$$s_{\mathrm{ik}} = \frac{\partial W\left(\mathbf{F}, \tilde{\mathbf{D}}\right)}{\partial F_{\mathrm{ik}}}, \tag{2.12}$$

$$\tilde{E}_{\mathrm{k}} = \frac{\partial W\left(\mathbf{F}, \tilde{\mathbf{D}}\right)}{\partial \tilde{D}_{\mathrm{k}}}. \tag{2.13}$$

For an ideal elastic dielectric body, its Helmholtz free energy density can be expressed as

$$W\left(\mathbf{F}, \tilde{\mathbf{D}}\right) = W_{\mathrm{s}}(\mathbf{F}) + \frac{F_{\mathrm{KM}} F_{\mathrm{KL}}}{2££_{o} \det\left(\mathbf{F}\right)} \tilde{D}_{\mathrm{M}} \tilde{D}_{\mathrm{L}}, \tag{2.14}$$

where $W_{\mathrm{s}}(\mathbf{F})$ is the strain energy density and the second term on the right side is associated with the polarization energy (Zhao *et al*., 2007). When a specific $W_{\mathrm{s}}(\mathbf{F})$ is selected, the nominal stress and nominal electric field in equations (2.12) and (2.13) can be obtained. Then the true stress ± and true electric field **E** can be obtained by adopting the well-established relations between the true and nominal quantities as follows

$$\pm_{\mathrm{ij}} = \frac{F_{\mathrm{jk}}}{\det(\mathbf{F})} s_{\mathrm{ik}}, \tag{2.15}$$

$$D_{\mathrm{i}} = \frac{F_{\mathrm{ik}}}{\det(\mathbf{F})} \tilde{D}_{\mathrm{k}}, \tag{2.16}$$

$$E_{\mathrm{i}} = H_{\mathrm{ik}} \tilde{E}_{\mathrm{k}}, \tag{2.17}$$

where H_{ik} is the inverse of F_{ik} ($F_{\mathrm{ik}}H_{\mathrm{ik}}$=1). When true stress ± and true electric field **E** are obtained, the electromechanical response of the dielectric body can be determined.

Based on the fully coupled field theories introduced above, Zhao *et al.* (2007) showed that regions of two different states (one being thick and the other thin) can coexist during the deformation of a DE membrane, which eventually leads to wrinkles in the membrane. Later, Huang and Suo (2011) further discussed this electromechanical state transition and coexistence phenomenon under various conditions and identified the critical point for the transition. Zhao and Suo (2007 and 2008) analyzed the electromechanical stability with the Hessian matrix of the free energy density function and proposed methods to attain programmable deformation of DEs. Suo and Zhu (2009) theoretically explained why DEs with interpenetrating networks can survive the electromechanical instability (EMI) and achieve large voltage-induced deformation. The EMI and the corresponding inhomogeneous deformation of DEs was further investigated by Park *et al*. (2012) by using a dynamic finite element model. Vertechy *et al.* (2012) presented a monolithic finite element formulation to model the large out-of-plane axisymmetric deformation of the buckling DE actuators. Adopting the neo-Hookean hyperelastic model, Zhu *et al*. (2010c) examined the large deformation of DE tube actuators and identified the critical actuation strain for the EMI. Instead of the voltage-control operation, Lu *et al*. (2014) investigated the charge-control operation of dielectric elastomer actuators and the charge localization instability. Koh *et al.* (2009) proposed a method to analyze the electromechanical cycles and the energy conversion mechanism of a DE generator.

2.2 Stability of dielectric elastomers subject to mechanical and electrical fields

As introduced in Chapter 1, the actuation of DEs is susceptible to the electromechanical instability, which can cause a premature electrical breakdown of DEs (Plante and Dubowsky 2006; Keplinger *et al*., 2012). It is thus essential to identify the stable and unstable states of DEs during actuation, which can be realized by perturbation analysis (Zhao *et al.*, 2007; Huang and Suo, 2011). When a DE under electromechanical loading is perturbed, the system changes from a state $(\mathbf{F}, \tilde{\mathbf{D}})$ to a nearby sate $(\mathbf{F}+\delta\mathbf{F}, \tilde{\mathbf{D}}+\delta\tilde{\mathbf{D}})$. Correspondingly, the change of the total free energy density is expressed as

$$\begin{aligned}\delta G_{\mathrm{f}} = &\int\left[W\left(\mathbf{F}+\delta\mathbf{F}, \tilde{\mathbf{D}}+\delta\tilde{\mathbf{D}}\right)-W\left(\mathbf{F}, \tilde{\mathbf{D}}\right)\right]\mathrm{d}V_0 \\ &-\int b_{\mathrm{i}}\delta x_{\mathrm{i}}\mathrm{d}V_0-\int T_{\mathrm{i}}\delta x_{\mathrm{i}}dS-\int Q\delta V\mathrm{d}V_0-\int \mu\delta V\mathrm{d}S\end{aligned}, \tag{2.18}$$

where $W(\mathbf{F}+\delta\mathbf{F}, \tilde{\mathbf{D}}+\delta\tilde{\mathbf{D}})-W(\mathbf{F}, \tilde{\mathbf{D}})$ is the change of the Helmholtz free energy density. Expanding δW into Taylor series up to the second order leads to

$$\begin{aligned}\delta W = &\frac{\partial W(\mathbf{F},\tilde{\mathbf{D}})}{\partial F_{\mathrm{ik}}}\text{¢}\, F_{\mathrm{ik}} + \frac{\partial W(\mathbf{F},\tilde{\mathbf{D}})}{\partial \tilde{D}_{\mathrm{N}}}\delta\tilde{D}_{\mathrm{N}} \\ &+\frac{1}{2}\frac{\partial^2 W(\mathbf{F},\tilde{\mathbf{D}})}{\partial F_{\mathrm{ik}}\partial F_{\mathrm{jl}}}\text{¢}\, F_{\mathrm{ik}}\text{¢}\, F_{\mathrm{jl}} + \frac{\partial^2 W(\mathbf{F},\tilde{\mathbf{D}})}{\partial F_{\mathrm{ik}}\partial \tilde{D}_{\mathrm{N}}}\text{¢}\, F_{\mathrm{ik}}\text{¢}\, \tilde{D}_{\mathrm{N}} + \frac{1}{2}\frac{\partial^2 W(\mathbf{F},\tilde{\mathbf{D}})}{\partial \tilde{D}_{\mathrm{N}}\partial \tilde{D}_{\mathrm{M}}}\text{¢}\, \tilde{D}_{\mathrm{N}}\partial\tilde{D}_{\mathrm{M}}\end{aligned} \quad . \tag{2.19}$$

Combining equations (2.18) and (2.19),

$$\begin{aligned}\delta G_{\mathrm{f}} = &\int\left(\frac{\partial W(\mathbf{F},\tilde{\mathbf{D}})}{\partial F_{\mathrm{ik}}} - s_{\mathrm{ik}}\right)\delta F_{\mathrm{ik}}\mathrm{d}V_0 + \int\left(\frac{\partial W(\mathbf{F},\tilde{\mathbf{D}})}{\partial \tilde{D}_{\mathrm{N}}} - \tilde{E}_{\mathrm{N}}\right)\delta\tilde{D}_{\mathrm{N}}\mathrm{d}V_0 \\ &+\int\left(\frac{1}{2}\frac{\partial^2 W(\mathbf{F},\tilde{\mathbf{D}})}{\partial F_{\mathrm{ik}}\partial F_{\mathrm{jl}}}\delta F_{\mathrm{ik}}\delta F_{\mathrm{jl}} + \frac{\partial W(\mathbf{F},\tilde{\mathbf{D}})}{\partial F_{\mathrm{ik}}\partial \tilde{D}_{\mathrm{N}}}\delta F_{\mathrm{ik}}\delta\tilde{D}_{\mathrm{N}} + \frac{1}{2}\frac{\partial^2 W(\mathbf{F},\tilde{\mathbf{D}})}{\partial \tilde{D}_{\mathrm{N}}\partial \tilde{D}_{\mathrm{M}}}\text{¢}\, \tilde{D}_{\mathrm{N}}\text{¢}\, \tilde{D}_{\mathrm{M}}\right)\mathrm{d}V_0\end{aligned} \quad . \tag{2.20}$$

When the state ($\mathbf{F}, \tilde{\mathbf{D}}$) is stable against a small perturbation, its total free energy density G_{f} has to be a local minimum. This requires δG_{f} to be positive-definite for any ($\text{¢}\mathbf{F}, \text{¢}\tilde{\mathbf{D}}$). More specifically, the first derivatives in equation (2.20) has to vanish and the sum of the second derivatives in equation (2.20) must be positive-definite, which recovers equations (2.12) and (2.13) and requires the Hessian matrix of the Helmholtz free energy density to be positive-definite. The Hessian matrix of the Helmholtz free energy density $W(\mathbf{F}, \tilde{\mathbf{D}})$ is given as

$$\mathbf{H} = \begin{bmatrix} \dfrac{\partial^2 W}{\partial F_{\mathrm{ik}}\partial F_{\mathrm{jl}}} & \dfrac{\partial W}{\partial F_{\mathrm{ik}}\partial \tilde{D}_{\mathrm{N}}} \\ \dfrac{\partial W}{\partial F_{\mathrm{jl}}\partial \tilde{D}_{\mathrm{M}}} & \dfrac{\partial^2 W}{\partial \tilde{D}_{\mathrm{N}}\partial \tilde{D}_{\mathrm{M}}} \end{bmatrix} \quad . \tag{2.21}$$

Therefore, to ensure state ($\mathbf{F}, \tilde{\mathbf{D}}$) is a stable state, it is required that

$$\frac{\partial^2 W}{\partial F_{\mathrm{ik}}\partial F_{\mathrm{jl}}} > 0\,, \tag{2.22}$$

$$\det(\mathbf{H}) > 0\,. \tag{2.23}$$

Using equations (2.22) and (2.23), it is found that the range between the peak and the trough of a typical electromechanical response curve is unstable and a snap-through deformation occurs right after the peak (see figure 1.3) (Zhao *et al.*, 2007; Huang and Suo, 2011; Koh *et al*., 2011)

2.3 Material models of hyperelastic materials

As shown in equation (2.14), a specific strain energy density function $W_s(\mathbf{F})$ needs to be selected before the electromechanical response of the dielectric body can be determined. Moreover, a strain energy density function should be selected based on the macromolecular network structure and stress-strain behavior of the material. For hyperelastic materials that can be viewed as incompressible (like dielectric elastomers), there are quite a few material models available in the literature to describe their strain energy density. The development of these hyperelastic material models are mainly based on three approaches: statistical mechanics treatments, invariant-based continuum mechanics treatments and stretch-based continuum mechanics treatments (Boyce and Arruda, 2000).

For the statistical mechanics approaches, it is assumed that the material is a structure of randomly-oriented long polymer chains (Treloar, 1975). When the elongation of the polymer chains is significantly less than their fully extended length, the strain energy density of the material can be described with the Gaussian model (Treloar, 1944)

$$W_G = \frac{1}{2} N k \theta \left(\lambda_1^2 + \lambda_2^2 + \lambda_3^2 - 3 \right), \tag{2.24}$$

where N is the number of chains, k is Boltzmann's constant, θ is the absolute temperature, λ_1, λ_2 and λ_3 are the principal stretch ratios (In this section, the deformation of material is considered in a principal stretch state). However, when the elongation of the polymer chains approaches to their extensibility, the prediction by the Gaussian model significantly differs from the observation in experiments. To account for the non-Gaussian nature of the polymer chains and more accurate individual chain statistics, material models that based on the assumption of a representative network structure have been proposed, such as the “3-chain” model (Wang and Guth, 1952), the four chain tetrahedral model (Flory and Rehner, 1943) and the “8-chain” model (Arruda and Boyce, 1993). As given below, polymer chains in the “8-chain” model are assume to rotate towards the principal axes of the stretching.

$$\mathrm{a}_{\text{chain}} = \left(\frac{1}{3}\left(\mathrm{a}_1^2 + \mathrm{a}_2^2 + \mathrm{a}_3^2 - 3\right)\right)^{1/2}, \tag{2.25}$$

$$W_{8\text{ch}} = Nk\bar{\ } \sqrt{n}\left[\ _{\text{chain}}\mathrm{a}_{\text{chain}} + \sqrt{n}\ln\left(\frac{\ _{\text{chain}}}{\sinh\ _{\text{chain}}}\right)\right], \tag{2.26}$$

$$_{\text{chain}} = L^{-1}\left(\frac{\mathrm{a}_{\text{chain}}}{\sinh\ _{\text{chain}}}\right), \tag{2.27}$$

where n is the number of links in the chain and L^{-1} is the inverse Langevin function. Although these “chain” models adopting non-Gaussian treatments can tackle large deformation of the material (close to its extensibility), they are not so accurate for small to moderate deformation.

As introduced above, the strain energy density of an isotropic and hyperelastic material can also be modeled under continuum mechanics treatments, for which the strain energy density of the material is always a function of three invariants I_1, I_2 and I_3.

$$I_1 = \mathrm{a}_1^2 + \mathrm{a}_2^2 + \mathrm{a}_3^2, \tag{2.28}$$

$$I_2 = \mathrm{a}_1^2\mathrm{a}_2^2 + \mathrm{a}_2^2\mathrm{a}_3^2 + \mathrm{a}_1^2\mathrm{a}_3^2, \tag{2.29}$$

$$I_3 = \mathrm{a}_1^2\mathrm{a}_2^2\mathrm{a}_3^2. \tag{2.30}$$

Moreover, for incompressible materials, $\mathrm{a}_1\mathrm{a}_2\mathrm{a}_3 = 1$ and $I_3 = 1$. As proposed by Rivlin (Rivlin, 1948), a general form of the strain energy density based on these three invariants is expressed as

$$W_{\mathrm{R}} = \sum_{i,j=0}^{\infty} C_{ij} \left(I_1 - 3\right)^i \left(I_2 - 3\right)^j , \tag{2.31}$$

where C_{ij} are material constants. When only invariant I_1 is retained, the neo-Hookean model is obtained,

$$W_{\mathrm{NH}} = C_{10} \left(I_1 - 3\right). \tag{2.31}$$

When only (i, j) = (0, 1) and (i, j) = (1, 0) are considered, the Mooney-Rivlin model (Mooney, 1940) is obtained,

$$W_{\mathrm{MR}} = C_{10} \left(I_1 - 3\right) + C_{01} \left(I_2 - 3\right). \tag{2.32}$$

In addition to the neo-Hookean and Mooney-Rivlin models, researchers have also attempted to develop some higher order I_1 models and found that they work better in capturing moderate to large deformation, such as the Yeoh model (Yeoh, 1993):

$$W_{\mathrm{Y}} = C_{10} \left(I_1 - 3\right) + C_{20} \left(I_1 - 3\right)^2 + C_{30} \left(I_1 - 3\right)^3 . \tag{2.33}$$

From equations (2.31), (2.32) and (2.33), it can be noticed that these models do not take the extensibility of the material (the limit of the stretch ratios) into account. While in a real polymer network, there is a limit of the extension of the polymer chains. To account for the extensibility of hyperelastic materials, Gent (Gent, 1996) proposed an alternate high order I_1 model which is in the form

$$W_{\mathrm{Gent}} = -\frac{G J_{\mathrm{lim}}}{2} \ln\left[1 - \left(I_1 - 3\right) / J_{\mathrm{lim}}\right], \tag{2.34}$$

where G is the shear modulus of the material, material parameter J_{lim} indicates the stretching limit of the material. Due to the logarithm function in equation (2.34), the stretch ratios have to satisfy $\left[1 - \left(I_1 - 3\right) / J_{\mathrm{lim}}\right] > 0$ and the maximum stretch ratios are limited by the value of J_{lim}.

In addition to the invariant-based continuum mechanics treatments, stretch-based continuum mechanics treatments are alternatives to model the strain energy density of hyperelastic materials. Under stretch-based continuum mechanics treatments, the strain energy density consists of three same functions of the principal stretch ratios, i.e., $w(\lambda_i)_{i=1,2,3}$, where $w(\lambda_i)_{i=1,2,3}$ are experimentally obtained. One model of this type is the Ogden model (Ogden, 1972) with the strain energy given as

$$W_{\mathrm{O}} = \sum_n \frac{\mu_n}{\alpha_n}\left(\lambda_1^{\alpha_n} + \lambda_2^{\alpha_n} + \lambda_3^{\alpha_n} - 3\right), \tag{2.35}$$

where the μ_n and α_n are material constants. The advantage of this type of model is that the degree of the sum (the value of n in equation (2.35)) can be adjusted to fit different experimental data.

2.4 Dynamic behaviors of dielectric elastomers

Focusing on the electromechanical coupling of the DEs, the modeling works above mainly studied their electromechanical deformation under the quasi-static assumption, without specifically considering the effect of inertia and the dynamic response. On the other hand, as DEs have been developed as resonators and oscillators in recent years (Zhang *et al*., 2005; Bonwit *et al*., 2006; Biggs and Hitchcock, 2010; O'Brien *et al*., 2012; O'Brien and Anderson, 2012), much interest has been drawn to study the dynamic behavior of DEs. For example, Mockensturn and Goulbourne (2006), Fox and Goulbourne (2008 and 2009), and Zhu *et al*. (2010a) examined the dynamic behaviors of the axisymmetric DE membranes. Son and Goulbourne (2010) proposed a numerical model for the dynamic response of tubular dielectric elastomer transducers. Yong *et al*. (2011) and Zhu *et al*. (2010b) investigated the nonlinear oscillation of balloon-like DE membranes. Moreover, one of the key merits of DE-based resonators and oscillators lies in the fact that their natural frequency can be actively tuned by changing the applied voltage on the DEs, which enables DE oscillators to have a wide range of resonant frequency and compensate for fabrication imperfection and environmental changes (Dubois *et al*., 2008). To better understand this useful feature, researchers have also conducted parametric studies on the natural frequency tuning process of DE-based resonators and oscillators. For example, Feng *et al.* (2011) investigated the active frequency tuning of a DE micro-beam resonator using the Euler-Bernoulli beam model. Li *et al.* (2012a) analyzed the nonlinear oscillation of a tunable DE membrane resonator by adopting the Gent model.

Another recent application of dielectric elastomers in dynamics is the tunable waveguides capable of actively filtering waves in the prescribed ranges of frequencies (Gei *et al.*, 2011). These ranges of frequencies corresponding to the filtered waves are within the "bandgaps" of the device, which can be determined from the dispersion diagrams of the waveguide. To change the bandgaps of a waveguide in a conventional way, one has to change the geometry of the structure, usually through adjustment of the pre-stress, phase transformation and thermal expansion. With the development of DE waveguides, controlling the bandgaps can be realized in a more active way, by changing the applied voltage on the DE. The modeling of dielectric elastomer waveguides can be tracked back to the studies on electrostatic wave propagation in finitely deformed dielectric solids. With reference to the propagation of small amplitude waves in electroactive materials, Dorfmann and Ogden (2010) proposed an electromechanical coupling theory to describe the plane waves propagating in a finitely deformed dielectric material. Shmuel et al. (2012) investigated the Rayleigh-Lamb wave propagation in the dielectric elastomer membranes undergoing large deformation. Based on these studies, Shmuel and deBotton (2012) investigated the voltage-controlled bandgaps in dielectric elastomer laminates using Bloch-Floquet theorem along with the transfer matrix method. Later, Shmuel and deBotton (2013) further analyzed the axisymmetric wave propagation in a dielectric elastomer tube subject to large deformation. Moreover, Shmuel (2013) has also explored the electrostatically tunable bandgaps in square dielectric elastomer composites with circular fibers.

2.5 Material viscoelasticity of dielectric elastomers

In addition to the hyperelastic behavior, the performance of DEs is also affected by their viscoelastic properties (Zhang *et al.*, 2004; Plante and Dubowsky, 2007; Bai *et al.*, 2014; Kollosche *et al.*, 2015). In fact, over a decade, various models have been developed to capture the material viscoelasticity of DEs. At the early stage, Wissler Mazza (2005b) proposed a quasi-linear viscoelasticity model to investigate the time-dependent response of a circular DE membrane. Based on the Christensen's theory of viscoelasticity (Christensen, 1980), Yang *et al*. (2005) developed a non-linear viscoelastic model for finite deformation of DE membranes. Later, Plante and Dubowsky (2007) studied the dynamic performance of DEs using a modified hyperelasticity theory to deal with the finite-deformation viscoelasticity. However, these models are either only congruous with relatively small deformation or could only explain some of the finite-deformation experimental phenomena.

Recently, based on the finite-deformation viscoelasticity theory by Reese and Govindjee (1998) and the fully coupled field theory for dielectric solids by Suo *et al*. (2008), Hong (2011) developed a model that can account for the effects of both electrostatics and finite-deformation viscoelasticity, which is capable of adopting most hyperelastic constitutive models and evolution laws for viscoelastic solids. Figure 2.2 shows the rheological model of the material regarding the finite-deformation viscoelasticity theory for dielectric elastomers by Hong (Hong, 2011). The rheological model illustrates two types of polymer chains in dielectric elastomers. The upper one (spring 1) is purely elastic while the lower one (spring 2 and the dashpot) relaxes with time and dissipates energy. For this rheological model, the strain energy of the material consists of two parts, i.e., the strain energy stored in spring 1 and the strain energy stored in spring 2. Due to possible large deformation of the elastomers, hyperelastic material models introduced above are commonly adopted to describe the strain energy density of the two springs in figure 2.2. With the framework of Hong's theory (Hong, 2011), Park and Nguyen (2013) presented a computational study on the electromechanical behavior of viscoelastic DEs. Wang *et al*. (2013) analyzed the inhomogeneous viscoelastic deformation of a DE membrane.

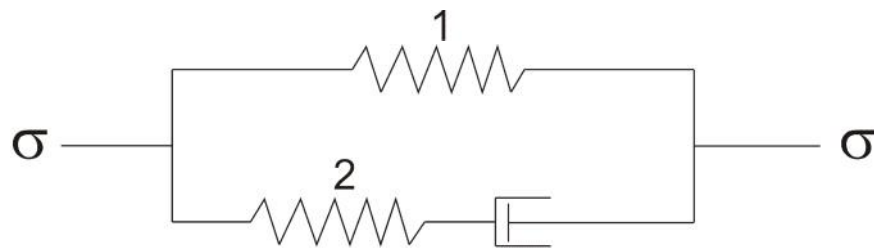

Figure 2.2 Rheological model of the material

In addition, it has been proven that the time-dependent inelastic deformation and stress relaxation induced by the material viscoelasticity can affect the dynamic response of the DEs (Hong, 2011; Foo *et al*., 2012a; Liu *et al*., 2014). Sheng *et al*. (2013) found that the influence of the material viscoelasticity on the dynamic response of the DE was more significant when the applied electric voltage was at low frequencies. Moreover, in addition to alternating electric load, Zhang *et al*. (2014) further investigated the dynamic performance of the dissipative DEs subject to alternating mechanical load, which provides useful information for comprehensively evaluating the performance of viscoelastic DE resonators and oscillators. Another typical application of DEs that strongly affected by the material viscoelasticity is DE generators and energy harvesters (Pelrine *et al.*, 2001; Huang *et al*., 2013; Shian *et al.*, 2014). Due to the material viscoelasticity of the DE, part of the scavenged energy from external sources dissipates through the inelastic deformation, which lowers the efficiency of the DE generator. In order to improve their efficiency, effort has also been devoted to the modeling of viscoelastic DE generators. For example, focusing on the viscoelasticity and current leakage, Foo *et al*. (2012b) studied the electromechanical conversion cycles of dissipative DE generators. Li *et al.* (2012b) presented an analytical model to characterize the energy harvesting of the viscoelastic DE generators under inhomogeneous fields.

From the introduction and review above, although much effort has been devoted to investigating the actuation, dynamic and energy harvesting performance of DEs, many of the critical issues in the applications of DEs have not been well settled yet. Therefore, further investigations regarding these issues will be discussed in the following chapters.

References

Arruda, E. M. and Boyce, M. C., 1993. A three-dimensional model for the large stretch behavior of rubber elastic materials. J. Mech. Phys. Solids **41**, 389-412.

Bai, Y., Jiang, Y., Chen, B., Foo, C. C., Zhou, Y., Xiang, F., Zhou, J., Wang, H. and Suo, Z., 2014. Cyclic performance of viscoelastic dielectric elastomers with solid hydrogel electrodes. Appl. Phys. Lett. **104**, 062902.

Biggs, S. J. and Hitchcock, R. N., 2010. Artificial muscle actuators for haptic displays: system design to match the dynamics and tactile sensitivity of the human fingerpad. Proc. SPIE **7642**, 76420I.

Bonwit, N., Heim, J., Rosenthal, M., Dunchenon, C. and Beavers, A., 2006. Design of commercial applications of EPAM technology. Proc. SPIE **6168**, 616805.

Boyce, M. C. and Arruda, E. M., 2000. Constitutive models of rubber elasticity: a review. Rubber Chem. Technol. **73**, 504–523.

Christensen, R. M., 1980. A nonlinear theory of viscoelasticity of application to elastomers. Transaction of the ASME **47**, 762-768.

Dorfmann, A. and Ogden, R. W., 2005. Nonlinear electroelasticity. Acta Mech. **174**, 167–183.

Dorfmann, A. and Ogden, R. W., 2010. Electroelastic waves in a finitely deformed electroactive material. IMA J. Appl. Math. **75**, 603-636.

Dubois, P., Rosset, S., Niklaus, M., Dadras, M. and Shea, H., 2008. Voltage control of the resonance frequency of dielectric electroactive polymer (DEAP) membranes. J. Microelectromech. Syst. **17**, 1072-1081.

Feng, C., Jiang, L. and Lau, W. M., 2011. Dynamic characteristics of a dielectric elastomer-based microbeam resonator with small vibration amplitude. J. Micromech. Microeng. **21**, 095002.

Flory, P. J. and Rehner, J., 1943. Statistical mechanics of cross-linked polymer networks II. Swelling. J. Chem. Phys. **11**, 521-526.

Foo, C. C., Cai, S., Koh, S. J. A., Bauer, S. and Suo, Z., 2012a. Model of dissipative dielectric elastomers. J. Appl. Phys. **111**, 034102.

Foo, C. C., Koh, S. J. A., Keplinger, C., Kaltseis, R., Bauer, S. and Suo, Z., 2012b. Performance of dissipative dielectric elastomer generators. J. Appl. Phys. **111**, 094107.

Fox, J. W. and Goulbourne, N. C., 2008. On the dynamic electromechanical loading of dielectric elastomer membranes. J. Mech. Phys. Solids **56**, 2669-2686.

Fox, J. W. and Goulbourne, N. C., 2009. Electric field-induced surface transformations and experimental dynamic characteristics of dielectric elastomer membranes. J. Mech. Phys. Solids **57**, 1417-1436.

Gei, M., Roccabianca, S. and Bacca M., 2011. Controlling bandgap in electroactive polymer-based structures. IEEE/ASME Transactions on Mechatronics **16**, 102-107.

Gent, A. N., 1996. A new constitutive relation for rubber. Rubber Chem. Technol. **69**, 59-61.

Goulbourne, N., Mockensturm, E. and Frecker, M., 2005. A nonlinear model for dielectric elastomer membranes. J. Appl. Mech. **72**, 899-906.

Hong, W., 2011. Modeling viscoelastic dielectrics. J. Mech. Phys. Solids **59**, 637-650.

Huang, J., Shian, S., Suo, Z. and Clarke, D. R., 2013. Maximizing the energy density of dielectric elastomer generators using equi-biaxial laoding. Adv. Funct. Mater. **23**, 5056-5061.

Huang, R. and Suo, Z., 2011. Electromechanical phase transition in dielectric elastomers. Proc. R. Soc. A **468**, 1014–1040.

Keplinger, C., Li T., Baumgartner, R., Suo Z. and Bauer, S., 2012 Harnessing snap-through instability in soft dielectrics to achieve giant voltage-triggered deformation. Soft Matter **8**, 285-288.

Koh, S. J. A., Zhao, X. and Suo, Z., 2009. Maximal energy that can be converted by a dielectric elastomer generator. Appl. Phys. Lett. **94**, 262902.

Koh, S. J. A., Li, T., Zhou, J., Zhao, X., Hong, W., Zhu, J. and Suo, Z., 2011. Mechanisms of large actuation strain in dielectric elastomers. J. Polym. Sci. B **49**, 504–515.

Kornbluh, R., Pelrine, R., Joseph, J, Heydt, R., Pei, Q. and Chiba, S., 1999. High-field electrostriction of elastomeric polymer dielectrics for actuation. Proc. SPIE **3669**, 149–161.

Li, T., Qu, S. and Yang, W., 2012a. Electromechanical and dynamic analyses of tunable dielectric elastomer resonator. Int. J. Solids Struct. **49**, 3754-3761.

Li, T., Qu, S. and Yang, W., 2012b. Energy harvesting of dielectric elastomer generators concerning inhomogeneous fields and viscoelastic deformation. J. Appl. Phys. **112**, 034119.

Liu, L., Chen, H., Sheng, J., Zhang, J., Wang, Y. and Jia, S., 2014. Experimental study on the dynamic response of in-plane deformation of dielectric elastomer under alternating electric load. Smart Mater. Struct. **23**, 025037.

Lu, T., Huang, J., Jordi, C., Kovacs, G., Huang, R., Clarke, D. R. and Suo, Z., 2012. Dielectric elastomer actuators under equal-biaxial forces, uniaxial forces, and uniaxial constraint of stiff fibers. Soft Matter **8**, 6167–6173.

McMeeking, R. M. and Landis, C. M., 2005. Electrostatic forces and stored energy for deformable dielectric materials. J. Appl. Mech. **72**, 581–590.

Mockensturm, E. M. and Goulbourne, N., 2006. Dynamic response of dielectric elastomers. Int. J. Nonlinear Mech. **41**, 388-395.

Mooney, M., 1940. A theory of large elastic deformation. J. Appl. Phys. **11**, 582-592.

O'Brien, B. M. and Anderson, I. A., 2012. An artificial muscle ring oscillator IEEE/ASME Transactions on Mechatronics **17**, 197-200.

O'Brien, B. M., Rosset, S., Shea, H. R. and Anderson, I. A., 2012. Cutting the fat: artificial muscle oscillators for lighter, cheaper and slimmer devices. Proc. SPIE **8340**, 834008.

Ogden, R. W., 1972. Large deformation isotropic elasticity-on the correlation of theory and experiment for incompressible rubberlike solids. Proc. R. Soc. Lond. A. **326**, 565-584.

Park, H. S. and Nguyen, T. D., 2013. Viscoelastic effects on electromechanical instabilities in dielectric elastomers. Soft Matter **9**, 1031-1042.

Park, H. S., Suo, Z., Zhou, J. and Klein, P. A., 2012. A dynamic finite element method for inhomogeneous deformation and electromechancial instability of dielectric elastomer transducers. Int. J. Solids Struct. **49**, 2187–2194.

Pelrine, R., Kornbluh, R. D., Eckerle, J., Jeuck, P., Oh, S., Pei, Q. and Stanford, S., 2001. Dielectric elastomers: generator mode fundamentals and applications. Proc. SPIE **4329**, 148-156.

Pelrine, R. E., Kornbluh, R. D. and Joseph, J. P., 1998. Electrostriction of polymer dielectrics with compliant electrodes as a means of actuation. Sens. Actuators A **64**, 77-85.

Plante, J. and Dubowsky, S., 2006. Large-scale failure modes of dielectric elastomer actuators. Int. J. Solids Struct. **43**, 7727-7751.

Plante, J. and Dubowsky, S., 2007. On the performance mechanisms of dielectric elastomer actuators. Sens. Actuators A **137**, 96-109.

Reese, S. and Govindjee, S., 1998. A theory of finite viscoelasticity and numerical aspects. Int. J. Solids Struct. **35**, 3455-3482.

Rivlin, R. S., 1948. Large elastic deformations of isotropic materials. IV. Further developments of the general theory. Philos. Trans. R. Soc. London. Ser. A 241, 379-397.

Sheng, J., Chen, H., Li B. and Chang, L., 2013. Temperature dependence of the dielectric constant of acrylic dielectric elastomer. Appl. Phys. A **110**, 511-515.

Shian, S., Huang, J., Zhu, S. and Clarke, D. R., 2014. Optimizing the electrical energy conversion cycle of dielectric elastomer generators. Adv. Mater. **26**, 6617-6621.

Shmuel, G., 2013. Electrostatically tunable band gaps in finitely extensible dielectric elastomer fiber composites. Int. J. Solids Struct. **50**, 680-686.

Shmuel, G. and deBotton, G., 2012. Band-gaps in electrostatically controlled dielectric laminates subjected to incremental shear motions. J. Mech. Phys. Solids **60**, 1970–1981.

Shmuel, G. and deBotton, G., 2013. Axisymmetric wave propagation in finitely deformed dielectric elastomer tubes. Proc. R. Soc. A **469**, 20130071.

Shmuel, G., Gei, M. and deBotton, G., 2012. The Rayleigh-Lamb wave propagation in dielectric elastomer layers subjected to large deformations. Int. J. Nonlinear Mech. **47**, 307-316.

Suo, Z., Zhao, X. and Greene, W. H., 2008. A nonlinear field theory of deformable dielectrics. J. Mech. Phys. Solids **56**, 467–486.

Suo, Z. and Zhu, J., 2009. Dielectric elastomers of interpenetrating networks. Appl. Phys. Lett. **95**, 232909.

Treloar, L. R. G., 1975. The physics of rubber elasticity. Oxford University Press, USA.

Treloar, L. R. G., 1944. Stress-strain data for vulcanised rubber under various types of deformation. Trans. Faraday Soc. **40**, 59-70.

Vertechy, R., Frisoli, A., Bergamasco, M., Carpi, F., Frediani, G. and Rossi, D. D., 2012. Modeling and experimental validation of buckling dielectric elastomer actuators. Smart Mater. Struct. **21**, 094005.

Wang, M. C. and Guth, E., 1952. Statistical theory of networks of non-gaussian flexible chains. J. Chem. Phys. **20**, 1144-1157.

Wang, H., Lei, M. and Cai, S., 2013. Viscoelastic deformation of a dielectric elastomer membrane subject to electromechanical loads. J. Appl. Phys. **113**, 213508.

Wissler, M. and Mazza, E., 2005. Modeling of a pre-strained circular actuator made of dielectric elastomers. Sens. Actuators A **120**, 184-192.

Yang, E., Frecker, M. and Mockensturm, E., 2005. Viscoelastic model of dielectric elastomer membranes. Proc. SPIE **5759**, 82-93.

Yeoh, O. H., 1993. Some forms of the strain energy function for rubber. Rubber Chem. Technol. **66**, 754-771.

Yong, H., He, X. and Zhou, Y., 2011. Dynamics of a thick-walled dielectric elastomer spherical shell. Int. J. Eng. Sci. **49**, 792-800.

Zhang, G., Gaspar, J., Chu, V. and Conde, J. P., 2005. Electrostatically actuated polymer microresonators. Appl. Phys. Lett. **87**, 104104.

Zhang, J., Chen, H., Sheng, J., Liu, L., Wang, Y. and Jia, S., 2014. Dynamic performance of dissipative dielectric elastomers under alternating mechanical load. Appl. Phys. A **116**, 59-67.

Zhang, X. Q., Wissler, M., Jaehne, B., Broennimann, R. and Kovacs, G., 2004. Effects of crosslinking, prestrain and dielectric filler on the electromechanical response of a new silicone and comparison with acrylic elastomer. Proc. SPIE, **5385**, 78-86.

Zhao, X., Hong, W. and Suo, Z., 2007. Electromechanical hysteresis and coexistent states in dielectric elastomers. Phys. Rev. B **76**, 134113.

Zhao, X. and Suo, Z., 2007. Method to analyze electromechanical stability of dielectric elastomers. Appl. Phys. Lett. **91**, 061921.

Zhao, X. and Suo, Z., 2008. Method to analyze programmable deformation of dielectric elastomer layers. Appl. Phys. Lett. **93**, 251902.

Zhu, J., Cai, S. and Suo, Z., 2010a. Resonant behavior of a membrane of a dielectric elastomer. Int. J. Solids Struct. **47**, 3254-3262.

Zhu, J., Cai, S. and Suo, Z., 2010b. Nonlinear oscillation of a dielectric elastomer balloon. Polym. Int. **59**, 378-383.

Zhu, J., Stoyanov, H., Kofod, G. and Suo, Z., 2010c. Large deformation and electromechanical instability of a dielectric elastomer tube actuator. J. Appl. Phys. **108**, 074113.

Chapter 3

3 Failure analysis of a dielectric elastomer plate actuator considering boundary constraints

3.1 Introduction

Compared with traditional smart materials in actuation (e.g. piezoelectric ceramics), which are known for their high electromechanical coupling and brittleness, dielectric elastomers (DEs) are characterized by their softness, flexibility, large deformation capability, lightweight and high coupling efficiency. As reviewed by Bar-Cohen and Zhang (2008), these properties make DEs an interesting alternative to conventional technologies in transduction and have extensive potential applications, such as artificial muscles, adaptive optical elements, energy harvesting, programmable haptic surfaces, active noise control, frequency tuning, conformal loudspeakers, binary actuation and sensors of force and pressure, and other biomimetic applications (Carpi *et al*., 2008; Pelrine *et al*., 1998, 2002; Stoyanov *et al*., 2008). The actuation performance of DE actuators with a variety of configurations has been experimentally studied, including stack, extender, bimorph, unimorph, diaphragm and tube actuators (Cameron *et al*., 2008; Carpi *et al*., 2008; Zhu *et al*., 2010c).

The actuation mechanism of DE actuators can be explained by a simple configuration: a planar DE actuator, as shown in Figure 3.1. The actuator is envisaged as a plate of DE, coated with compliant electrodes. Subject to a voltage between the electrodes, the DE planar actuator expands in area and exhibits a reduction in thickness. This expansion in area can produce strains from 30% to 40% (Kornbluh *et al*., 1999). It has been experimentally demonstrated that the application of pre-stretch can further improve the actuation performance of the planar DE actuators. For example, more than 100% in-plane strain of a DE plate has been achieved by pre-stretching the elastomer (Pelrine *et al*., 2000). Alternatively, using the elastomer with interpenetrating networks (Ha *et al*., 2006), swelling the elastomer with a solvent (Shankar *et al*., 2007) or controlling the electric charge during actuation (Bochobza-Degani *et al*., 2003; Keplinger *et al*., 2010) can also increase the actuation strains of the DE actuators. Some studies have even shown that it is possible to achieve actuation strains over 500% by choosing or designing a DE with a suitable stress–strain curve (Zhao and Suo, 2010). In order to clarify the actuation mechanisms of the DE actuators, hyperelastic constitutive models were used to illustrate the large and non-linear deformation of DE planar actuators. Kofod (2001) adopted the neo-Hookean, Mooney–Rivlin and Ogden models to investigate this non-linear deformation. Furthermore, Suo and colleagues used the Arruda–Boyce model and Gent model to investigate the electromechanical response of DEs (Koh *et al*., 2011b; Li et al., 2011; Suo, 2010; Suo and Zhu, 2009; Zhao *et al*., 2007)

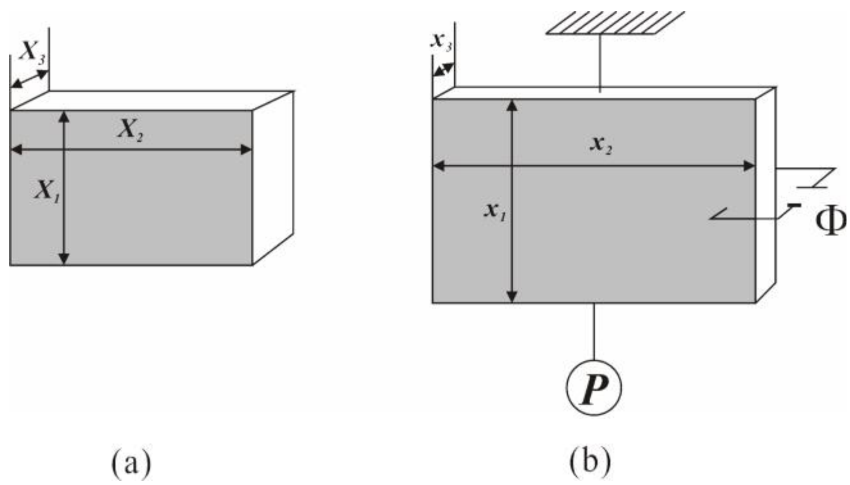

Figure 3.1 Actuation of a DE plate actuator: (a) undeformed state and (b) deformed state due to an electric voltage c with mechanical pre-stretch force P. DE: dielectric elastomer

The actuation of the planar DE actuators, however, is limited by multiple failure modes of the DEs (Plante and Dubowsky, 2006). In addition to material strength and electrical breakdown (EB), DE actuators are also susceptible to electromechanical instability (EMI), that is, the applied voltage causes excessive thinning of the DE, resulting in a premature EB. As reported by Plante and Dubowsky (2006), the EMI, also known as pull-in instability, may also cause the DE to deform into a complex wrinkling pattern. Both the EMI and the EB inhibit the full potential deformation actuation of DEs, warranting considerable attention recently.

Zhao and Suo (2010) categorized DEs into three groups by using an ideal dielectric model to interpret the diverse failure modes observed in experiments: the dielectric may suffer EB prior to EMI with only small deformation of actuation, fail at limited stretch when the voltage reaches the peak or survive the snap-through EMI with a large deformation of actuation. Another type of DE has been further identified by Koh *et al.* (2011b), which demonstrates a monotonic increase in actuation strain with voltage. Correspondingly, EMI does not occur during actuation, and the maximum actuation strain is simply limited by the dielectric strength. It is now well established that the EMI can be suppressed or eliminated by pre-stretching the DEs or restricting the stretch limit of the DEs, which could be realized by adding interpenetrating networks in the polymers (Koh *et al*., 2011b; Li *et al*., 2011; Wissler and Mazza, 2005).

Obviously, large deformation actuation without failure is desirable for the DE actuators. Therefore, this work aims to uncover possible mechanisms for a DE plate actuator to avoid EMI while achieving large actuation.

3.2 Actuation of an unconstrained DE plate under uniaxial stretch

As mentioned in the previous section, the EMI may inhibit the full potential actuation of DE actuators. In order to investigate how the EMI can be controlled by boundary constraints, the electromechanical response of a DE plate actuator with and without boundary constraints is considered. For an actuator without constraints, as illustrated in Figure 3.1(a), in the undeformed state, the dimensions of the plate are X_1, X_2 and X_3. When the plate is pre-stretched by a uniaxial force P, it elongates in the X_1-direction and contracts in the other two directions. The plate is then subject to an electric voltage c between the two electrodes, which induces electric charges on both electrodes. Meanwhile, the applied electric voltage causes a reduction in the X_3-direction, leading to an expansion of the area of the plate. Under the pre-stretch mechanical load and the applied electric voltage, the DE plate deforms to the current state as shown in Figure 3.1(b) with x_1, x_2 and x_3 being the current dimensions. The stretch ratios are defined as $a_1 = x_1/X_1$, $a_2 = x_2/X_2$ and $a_3 = x_3/X_3$, respectively. For the DE actuator shown in Figure 3.1, the stresses $\pm_1$, $\pm_2$ and $\pm_3$ along the x_1, x_2 and x_3 directions satisfy the following (Huang and Suo, 2011; Zhao *et al*., 2007)

$$\pm_1 - \pm_3 + \pounds\pounds_0 E^2 = \text{ª}_1 \frac{\partial W_s\left(\text{ª}_1, \text{ª}_2, \text{ª}_3\right)}{\partial \text{ª}_1} - \text{ª}_3 \frac{\partial W_s\left(\text{ª}_1, \text{ª}_2, \text{ª}_3\right)}{\partial \text{ª}_3}, \quad (3.1)$$

$$\pm_2 - \pm_3 + \pounds\pounds_0 E^2 = \text{ª}_2 \frac{\partial W_s\left(\text{ª}_1, \text{ª}_2, \text{ª}_3\right)}{\partial \text{ª}_2} - \text{ª}_3 \frac{\partial W_s\left(\text{ª}_1, \text{ª}_2, \text{ª}_3\right)}{\partial \text{ª}_3}, \quad (3.2)$$

where $\pounds_0$ is the permittivity of air or vacuum, $\pounds$ is the relative dielectric constant of the material, E is the electric field induced by the applied voltage and $W_s\left(\text{ª}_1, \text{ª}_2, \text{ª}_3\right)$ is the elastic strain energy density function of the elastomer. As stated by Huang and Suo (2011) that when an elastomer undergoes large deformation, the change in the shape of the elastomer is much more significant than the change in the volume. Under this condition, the DE can be assumed as incompressible with stretching ratios satisfying $\text{ª}_3 = 1/(\text{ª}_1\text{ª}_2)$. This assumption has been widely used in studying the electromechanical coupling of DEs in literature (Koh *et al*., 2011b; Wissler and Mazza, 2005). The electric field E in the x_3-direction is related to the applied voltage c by $E = \text{c:ª}_1 \text{ª}_2/X_3$, and the stress in the x_1-direction can be expressed as $\pm_1 = P\text{ª}_1 / X_2 X_3$ under homogeneous deformation assumption. Among the constitutive models of rubber elasticity (Boyce and Arruda, 2000), a particular one is the Gent model (Gent, 1996), in which the strain energy density function is expressed as

$$W_s = -\frac{G J_{\lim}}{2} \ln\left(1 - \frac{\text{ª}_1^2 + \text{ª}_2^2 + \text{ª}_3^2 - 3}{J_{\lim}}\right), \quad (3.3)$$

where G is the shear modulus and $J_{\lim}$ is a dimensionless parameter related to the stretching limit of the material. Since the elastomer is free in the X_2- and X_3-directions, $\pm_2 = \pm_3 = 0$. Combining equations (3.1), (3.2) and (3.3) results in

$$\frac{P}{GX_2X_3} = \frac{J_{\lim}\left(\lambda_1 - \lambda_1^{-1}\lambda_2^{2}\right)}{J_{\lim} - \lambda_1^2 - \lambda_2^2 - \lambda_1^{-2}\lambda_2^{-2} + 3}, \tag{3.4}$$

$$\left(\frac{\Phi}{X_3}\sqrt{\frac{\varepsilon\varepsilon_0}{G}}\right)^2 = \frac{J_{\lim}\left(\lambda_1^{-2} - \lambda_1^{-4}\lambda_2^{-4}\right)}{J_{\lim} - \lambda_1^2 - \lambda_2^2 - \lambda_1^{-2}\lambda_2^{-2} + 3}. \tag{3.5}$$

These non-linear coupled equations govern the electromechanical response of the DE actuator, in which P / GX_2X_3 is the normalized mechanical load denoted as P^* and $\Phi / \left(X_3\sqrt{G/\varepsilon\varepsilon_0}\right)$ is the normalized electrical load denoted as Φ^*. Once these loads are prescribed, the stretch ratios λ_1 and λ_2 in the current state of the planar DE can be determined by solving these nonlinear equations

The typical electromechanical response for the DE actuator with various pre-stretches (P^*), i.e., Φ^*–λ_1, is plotted in Figure 3.2. Here, $J_{\lim}$ may vary within a large range of values depending on the extensibility limit of the polymer chains of the DE. However, it is set as $J_{\lim} = 125$ in this work (Kollosche *et al*., 2012). As shown in Figure 3.2, for small applied voltage (Φ^*), the DE stretch response λ_1 increases with the Φ^* for any fixed P^*. Once the Φ^* reaches a peak value, the electromechanical response curve then drops down. However, as the stretch becomes very large, Φ^* increases again. When the DE reaches its limit of extensibility, the response curves become almost vertical. Following the perturbation analysis (Huang and Suo, 2011; Leng *et al*., 2009), the interval between the peak and the trough of the response curve reflects EMI, and the stretch ratio corresponding to the peak of the Φ^* is the onset of the EMI. Under an Φ^*-control actuation, at the onset of the EMI, λ_1 may snap through the unstable interval from a small value to a very large value as shown by the dotted arrow in Figure 3.2, which is desirable for the DE actuator to achieve large actuation. However, the DE may not survive the snap-through due to the EB.

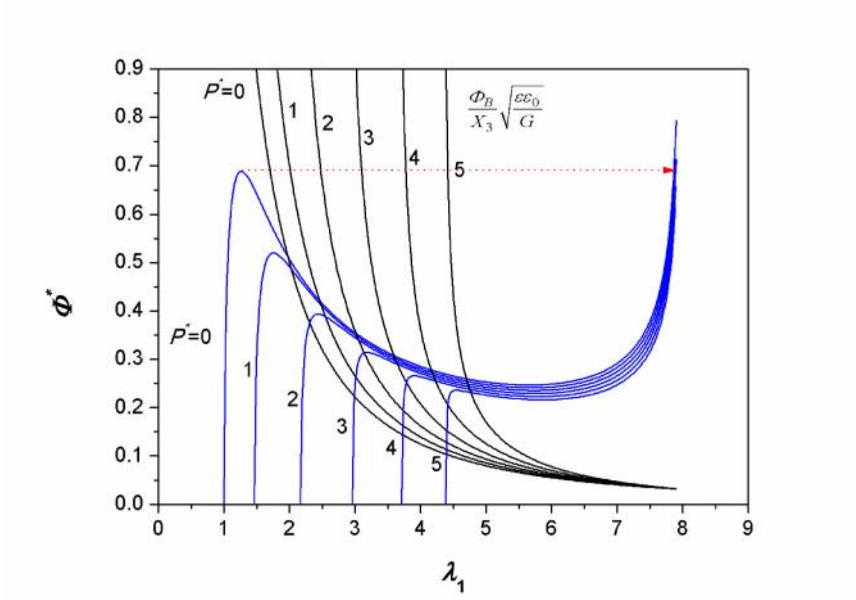

Figure 3.2 Electromechanical response curves (Φ^*–λ_1 curve) and electrical breakdown curves of a DE plate actuator without boundary constraints.

As a typical failure mode of DEs, EB occurs when the electric field exceeds the dielectric strength E_B. Although the dielectric strength may change during deformation (Kofod *et al*., 2003; Plante and Dubowsky, 2006), it is still reasonable to assume a fixed E_B in a theoretical treatment (Koh *et al*., 2011b; Li *et al*., 2011; Zhao and Suo, 2010). The voltage corresponding to the EB is $\Phi_B = E_B X_3 \lambda_3$. Introducing a dimensionless parameter $d = E_B\sqrt{\varepsilon\varepsilon_0 / G}$ (Koh *et al*., 2011b), the voltage, according to the EB of the actuator in Figure 3.1, is determined from

$$\frac{\Phi_B}{X_3}\sqrt{\frac{\varepsilon\varepsilon_0}{G}} = d\lambda_1^{-1}\lambda_2^{-1}. \tag{3.6}$$

The $\Phi_B/\left(X_3\sqrt{G/\varepsilon\varepsilon_0}\right)-\lambda_1$ curves are also plotted in Figure 3.2 with different P^* and d = 2. With the considered values of the material constants, the snap-through line interacts with the EB curve, which indicates that the EB occurs during the snap-through process. In other words, the DE actuator does not survive the snap-through due to the EB, and its stretch limit is at the onset point. It should be noted that the value of the dimensionless parameter *d* depends on the material properties since the dielectric strength E_B is regarded as independent of deformation (Zhao and Suo, 2010). As discussed by Zhao and Suo (2010), for the DE with a smaller d, the DE actuator may fail before it reaches the onset of the EMI. However, for a DE with exceptionally large dielectric strength, the actuator may survive the snap-through and reach a stable state.

Koh *et al.* (2011b) showed that larger actuation can be obtained by minimizing the magnitude of the snap-through or eliminating the EMI. This can be realized, e.g., by moving the material limiting stretch ratio λ_{lim} closer to the peak of Φ^* or applying pre-stretch (P^*). Obviously, with the increase in the P^*, the peak is effectively suppressed as in Figure 3.2. In this work, whether the EMI could be suppressed by applying boundary constraints to the DE actuator is investigated.

3.3 Actuation of a constrained DE plate under uniaxial stretch

In order to see the effect of the boundary constraints on the electromechanical response of a planar DE actuator, a sliding constraint along the X_1-direction is artificially set by attaching rollers at the ends of the DE actuator as in Figure 3.3. In the undeformed state (Figure 3.3(a)), some space is left between the fixed wall and the DE in the X_2-direction in order for the free deformation of the DE in this direction. The distance h between the DE actuator and the walls can be controlled by setting it relative to a particular stretch ratio $x_2/X_2 = \lambda^*$, that is, $2h = (\lambda^*-1)\, X_2$, where λ^* is the value of λ_2 when the DE reaches the onset point of the EMI (i.e. $\lambda_1 = \lambda_{onset}$). Once the DE actuator is subject to the electric voltage Φ in the X_3-direction and the pre-stretching mechanical force P in the X_1-direction, the actuator deforms to the current state (Figure 3.3(b)) with dimension $x_1x_2x_3$. Before the actuator reaches the walls, its electromechanical response is governed by equations (3.4) and (3.5). However, when the DE actuator reaches the walls, the deformation in the X_2- direction is constrained with $x_2/X_2 = \lambda^*$ thereafter, while the deformation in the other two directions keeps changing since the actuator can still slip in the X$_1$-direction. With x_2/X_2 = a* and ±$_1$ = P/x_2x_3, combining equations (3.1) and (3.3) results in

$$P^* + \left(c^*\right)^2 a_1 a^2 = \frac{J_{\lim}\left[a_1 - a_1^{-3}\left(a^*\right)^{-2}\right]}{J_{\lim} - a_1^2 - \left(a^*\right)^2 - a_1^{-2}\left(a^*\right)^{-2} + 3}, \tag{3.7}$$

which governs the electromechanical response of the DE after it touches the constrained walls. For the actuator in Figure 3.3, if the EB occurs before the actuator touches the constrained walls, the electrical breakdown voltage is the same as that in equation (3.6). Otherwise, such a voltage for a_2 = a* is determined as

$$\frac{c_B}{X_3}\sqrt{\frac{££_0}{G}} = d\,a_1^{-1}\left(a^*\right)^{-1}. \tag{3.8}$$

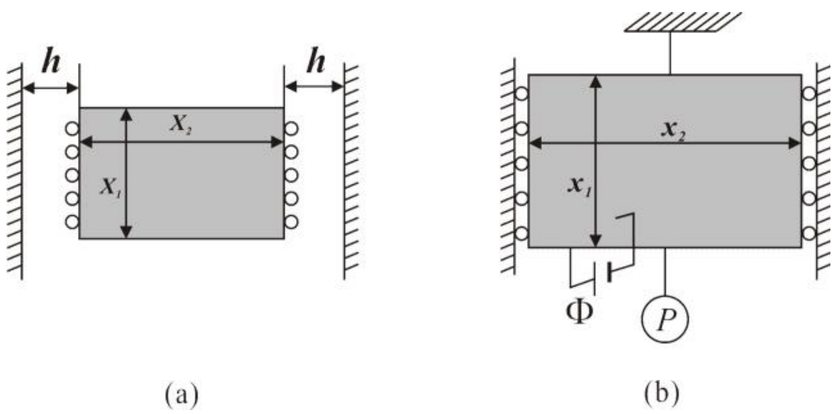

Figure 3.3 Actuation of a DE plate actuator constrained in X$_2$-direction: (a) undeformed state; (b) deformed state due to an electric voltage c with a mechanical pre-stretch force P.

Figure 3.4 depicts the electromechanical response for a constrained DE. The monotonicity of the response curves indicates that EMI has been eliminated by constraining the DE actuator. Compared with Figure 3.2, all the intersection points between the electrical breakdown curves and the electromechanical response curves have been shifted significantly to a larger deformation ª$_1$. These results indicate that the actuation performance in one direction is improved by constraining the deformation in the perpendicular direction.

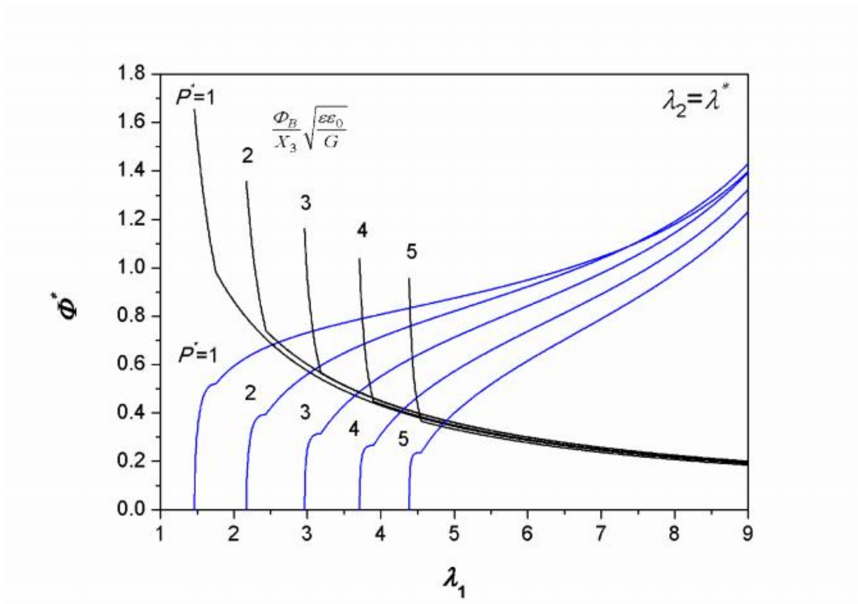

Figure 3.4 Electromechanical response curves (c*–ª$_1$ curve) and electrical breakdown curves of a DE plate actuator constrained in X_2-direction (ª$_2$=ª$*$).

To see the maximum actuation stretch in the X_1-direction due to the electromechanical coupling, ª$_{EB}$–ª$_{pre}$ as a function of P^* is plotted in Figure 3.5, in which ª$_{EB}$ and ª$_{pre}$ represent the stretch ratio at the electrical breakdown and stretch ratio caused by the pre-stretching mechanical load, respectively. Compared to the DE that is free in the X_2-direction, the constrained DE has a much higher actuation stretch, particularly with smaller pre-stretch P^*. For example, when P^* = 1, the voltage-induced stretch ratio varies from 0.29 to 1.07. The dramatic increase in the stretch indicates that the DE actuation performance could be significantly improved by applying boundary constraints. Nevertheless, the buckling failure mode should be taken into account for the DE with boundary constraints, which may reduce the actuation stretch improvement as shown in Figure 3.5.

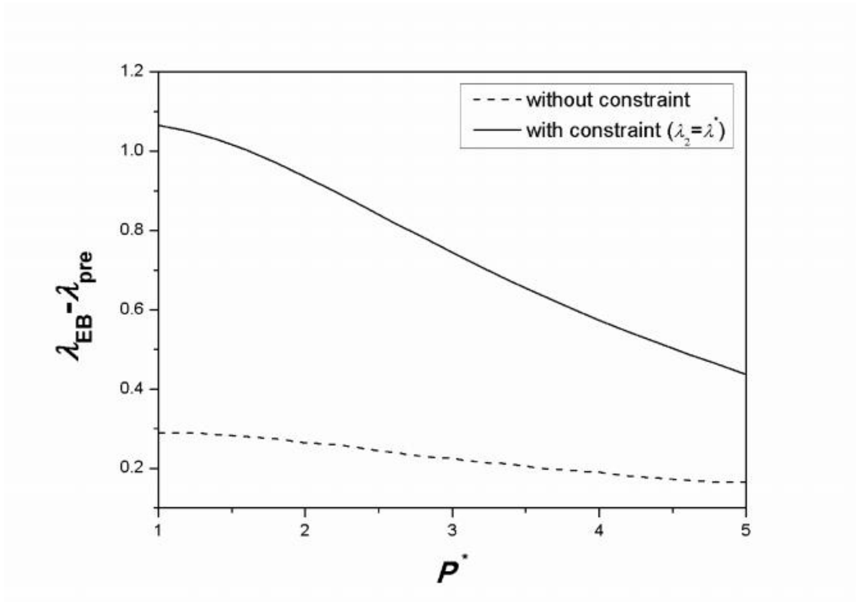

Figure 3.5 Actuation stretch **(**α_{EB}-α_{pre}) in X_1-direction for a DE plate actuator at electrical breakdown.

As constrained by the walls, the DE is no longer free in the X_2-direction when $a_2 = a^*$. As a consequence, a compressive reaction will be generated by the walls to the actuator in the X_2-direction. Such a compression stress is determined as

$$\pm_2 = \frac{GJ_{\lim}\left(a^{*2} - a_1^{-2} a^{*-2}\right)}{J_{\lim} - a_1^2 - a^{*2} - a_1^{-2} a^{*-2} + 3} - ££_0 E^2 . \tag{3.9}$$

Correspondingly, the reaction force from the walls is expressed as

$$F_2 = -\pm_2 X_1 X_3 / a^* . \tag{3.10}$$

Substituting equation (3.9) into equation (3.10) results in

$$\frac{F_2}{X_1 X_3 G} = \left(c^*\right)^2 a_1^2 a^* - \frac{J_{\lim}\left(a^* - a_1^{-2} a^{*-3}\right)}{J_{\lim} - a_1^2 - a^{*2} - a_1^{-2} a^{*-2} + 3} . \tag{3.11}$$

It should be noted that this compression may cause another failure mode of the structure, that is, the mechanical buckling of the actuator, which needs further investigation. The critical force for plate buckling with different boundary conditions is in general expressed as (Akesson, 2007; Brush and Almroth, 1975)

$$F_{\mathrm{c}} = \frac{®^2 k_{\mathrm{c}} E_{\mathrm{Y}} \left(X_3 ª_3\right)^3}{12(1-¬^2) X_1 ª_1} \tag{3.12}$$

where E_{Y} is Young's modulus, ¬ is Poisson's ratio and k_{c} is the buckling coefficient that depends on the panel aspect ratio $X_2 ª_2 / X_1 ª_1$, the buckled mode and the boundary conditions. Recalling that the stretch ratios of the plate satisfy $ª_3 = 1/(ª_1 ª^*)$ gives

$$\frac{F_{\mathrm{c}}}{X_1 X_3 G} = c ª_1^{-4} ª^{*-3}, \tag{3.13}$$

where $c = \frac{®^2 k_c E_Y}{12\left(1-¬^2\right) G} \left(\frac{X_3}{X_1}\right)^2$. Once the reaction compressive force F_2 from the boundary constraints reaches the critical buckling force in equation (3.13), mechanical buckling of the DE actuator occurs.

When buckling occurs, the maximum stretch ratio $ª_{\mathrm{MB}}$ in the X_1-direction can be obtained by combining equations (3.11) and (3.13) and is smaller than the values determined by the EB. Figure 3.6 shows $ª_{\mathrm{MB}} – ª_{\mathrm{pre}}$ versus P^* for various buckling parameter c. For smaller P^*, it is observed from Figure 3.6 that the constrained DE actuator has a higher actuation stretch ratio than the DE actuator without constraints, especially when P^* is relatively low. However, as P^* increases to a certain level, the maximum actuation stretch ratio for a constrained DE actuator is not significantly different from that for a DE actuator without constraints. From equation (3.13), it is observed that a higher value of c indicates a higher resistance against buckling. As shown in Figure 3.6, the constrained DE has a better actuation performance with an increase in c.

For example, when c = 2 and P^* = 1 (Figure 3.6(b)), the actuation stretch ratio is improved over 18% by constraining the DE actuator.

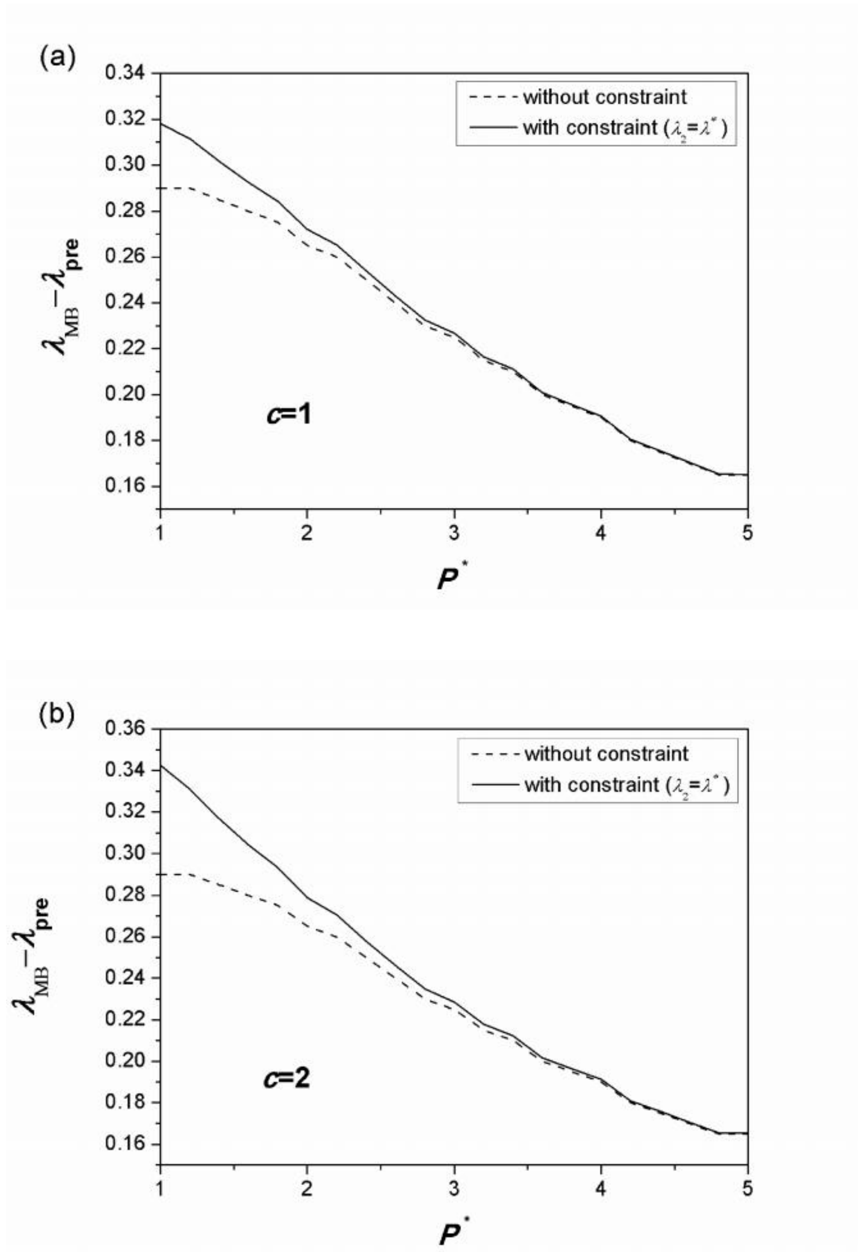

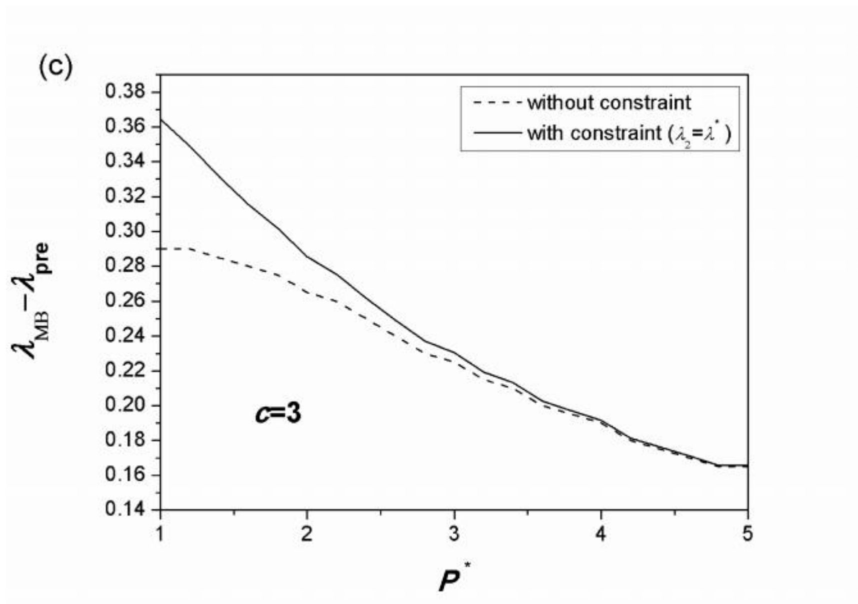

Figure 3.6 Actuation stretch (λ_{MB}-λ_{pre}) in X_1-direction for a DE plate actuator at buckling: (a) *c*=1; (b) *c*=2; (c) *c*=3.

For a DE plate actuator constrained in the X_2-direction, the comparison results as shown in Figures 3.5 and 3.6 indicate that the actuation stretch is limited, either by the electrical breakdown or the possible mechanical buckling. Therefore, it is necessary to identify which failure mode occurs first during the actuation process of the DE actuator. Once the material properties and the dimensions of the DE actuator are selected (i.e. the parameters *c* and *d* defined previously are determined), one can find the critical stretch ratios for these two failure modes. Based on these critical stretch ratios, phase diagrams can be drawn to define the regions of the electrical breakdown and mechanical buckling at various levels of the P^* as shown in Figure 3.7. These phase diagrams indicate that under a certain P^*, if the values of *c* and *d* for the actuator fall into the region on the left, it fails predominantly by EB, otherwise, it fails by mechanical buckling. For example, for a constrained DE with c = 2 and d = 2 subject to P^* = 1, its failure mode as the mechanical buckling can be determined from Figure 3.7(a). Correspondingly, the maximum obtainable actuation stretch of the actuator is the critical stretch ratio for buckling. These phase diagrams also show that the DE actuator is more prone to buckling due to the large thickness reduction caused by the high in-plane mechanical stretch. Therefore, with the increase in the P^*, the buckling failure mode tends to be more dominant by comparison of Figure 3.7(a) to 3.7(c). The results in these figures also suggest that the failure mode of this constrained DE planar actuator can be switched by choosing suitable values of c and d. In other words, choosing appropriate materials or modifying the initial dimensions of the DE actuator opens new avenues for improving the actuation performance of the DE actuators. It should be mentioned that d may change with the deformation of the DE since the electrical breakdown field E_B may vary with strains as evidenced by the experimental data (Kofod *et al*., 2003). However, the variation mechanisms have not been well understood as discussed by Zhao and Suo (2010). In addition, c depends on the boundary constraints of the DE system, which may vary within a scattered range. All these factors should be considered in the realistic DE actuators. This work aims to theoretically predict the actuation performance of a DE system through a parametric study by choosing representative values of c and d; however, how to realize the boundary constraints for better actuation performance of the DE system in reality is challenging and should be further explored through experiments.

This work focuses on a plate model of the DE, which may sustain compression during the actuation deformation. It is concluded that the boundary constraints for the plate may significantly improve the actuation performance of the DE actuator. For some membrane configurations of the DE actuators in the literature (Koh *et al*., 2011a, 2011b; Li *et al*., 2011; Wissler and Mazza, 2007), the current analysis is limited in application since the membrane cannot sustain compression. However, the results from this work suggest that the performance of the membrane actuators can be enhanced if the structures can be altered to sustain compression, for example, by adding reinforcing elements into the membrane. It should also be mentioned that this work focuses on DEs that have small to intermediate values of parameter d. If a DE has a larger d value, it may survive the snap-through deformation and reach a stable state at a large stretch (Koh *et al*., 2011b). Under this condition, it is unnecessary to constrain the boundaries in order to achieve a large actuation. Moreover, further experimental work should be developed to validate against the theoretical modeling presented in this article.

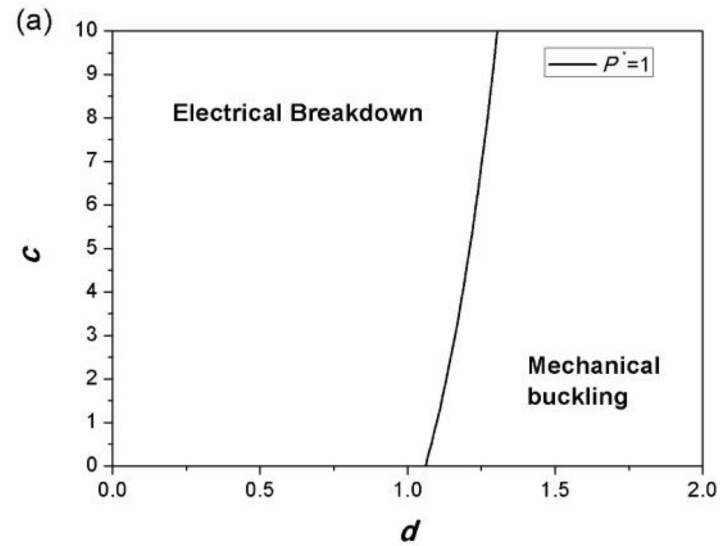
(a)
P* =1
Electrical Breakdown
Mechanical buckling
c
d
0.0
0.5
1.0
1.5
2.0
0
1
2
3
4
5
6
7
8
9
10

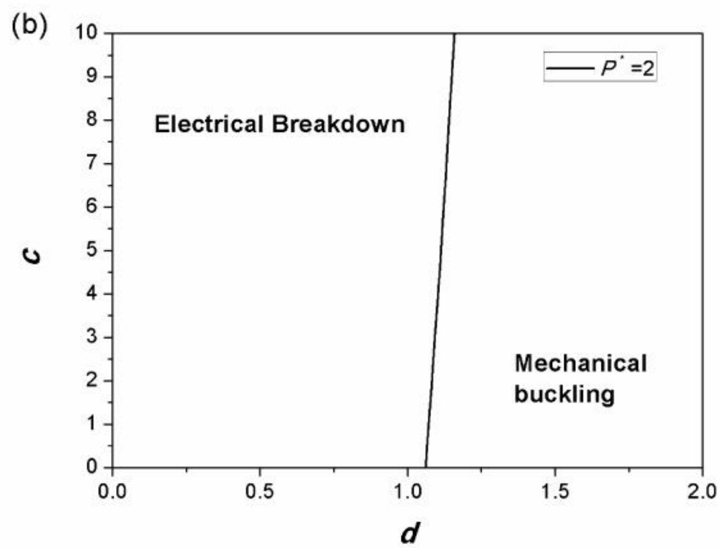
(b)
P* =2
Electrical Breakdown
Mechanical buckling
c
d
0.0
0.5
1.0
1.5
2.0
0
1
2
3
4
5
6
7
8
9
10

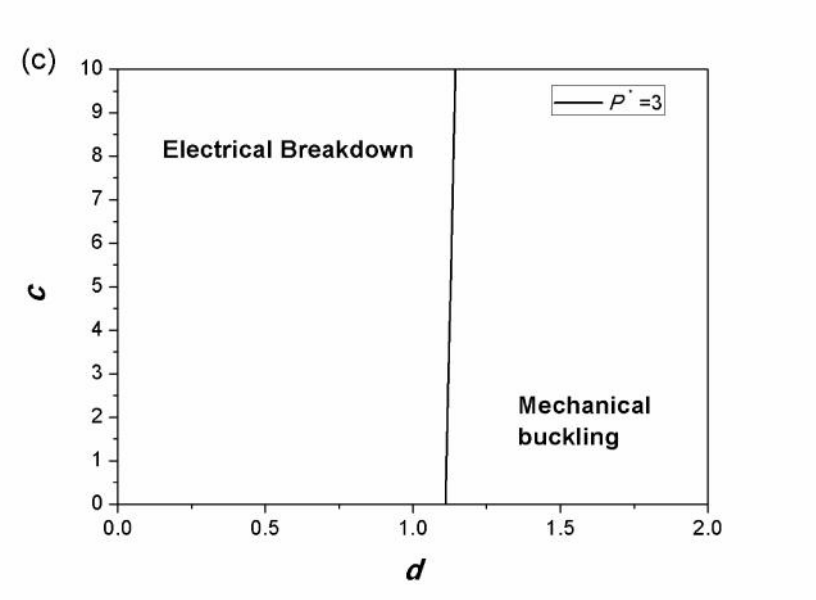

Figure 3.7 Phase diagrams for failure modes of a constrained DE plate actuator: (a) P^*=1; (b) P^*=2; (c) P^*=3.

3.4 Conclusion

Based on the Gent model for hyperelastic materials, the electromechanical responses of a DE plate actuator are investigated in this study. The mechanisms of the EMI are elucidated, suggesting that the EMI may severely inhibit the full actuation of a DE plate actuator with some particular material properties. In order to eliminate the EMI, boundary constraints are applied to obtain monotonic response behaviour of the actuation for the DE actuator. It is observed that the actuation strains can be improved by constraining the boundaries of a DE actuator. With control of the boundary conditions, considerations should be given to the possible mechanical buckling failure mode that may occur. Therefore, two possible failure modes, EB and mechanical buckling, are investigated and interpreted via phase diagrams. Simulation results based on Gent model suggest that the failure modes of a constrained DE actuator can be controlled by choosing the appropriate material properties and dimensions of the actuator. This work is envisaged to be useful for understanding the electromechanical responses of the DEs and guiding the optimization design of planar DE actuators with desirable actuation deformation.

References

Akesson, B., 2007. Plate Buckling in Bridges and other Structures. Taylor & Francis, London/New York, pp. 5-10.

Bar-Cohen, Y. and Zhang, Q., 2008. Electroactive polymer actuators and sensors. MRS BULLETIN **33**, 173-181.

Bochobza-Degani, O., Elata, D. and Nemirovsky, Y., 2003. A general relation between the ranges of stability of electrostatic actuators under charge or voltage control. Appl. Phys. Lett. **82**, 302-304.

Boyce, M. C. and Arruda, E. M., 2000. Constitutive models of rubber elasticity: A Review. Rubber Chem. Technol. **73**, 504-523.

Brush, D. O. and Almroth, B. O., 1975. Buckling of Bars, Plates, and Shells. McGraw-Hill, New York, pp. 75-99.

Cameron, C. G., Szabo, J. P., Johnstone, S., Massey, J. and Leidner, J., 2008. Linear actuation in coextruded dielectric elastomer tubes. Sens. Actuators A **147**, 286-291.

Carpi, F., Rossi, D. D., Kornbluh, R., Pelrine, R. and Sommer-Larsen, P., 2008. Dielectric Elatomers as Electromechanical Transducers. Elsevier, Amsterdam.

Gent, A. N., 1996. A New Constitutive relation for rubber. Rubber Chem. Technol. **69**, 59-61.

Ha, S. M., Yuan, W., Pei, Q., Pelrine, R. and Stanford, S., 2006. Interpenetrating polymer networks for high-performance electroelastomer artificial muscles. Adv. Mater. **18**, 887-891.

Huang, R. and Suo, Z., 2011. Electromechanical phase transition in dielectric elastomers. Proc. R. Soc. A **468**, 1014-1040.

Keplinger, C., Kaltenbrunner, M., Arnold, N. and Bauer, S., 2010 Röntgen's electrode-free elastomer actuators without electromechanical pull-in instability. Proc. Natl. Acad. Sci. USA **107**, 4505-4510.

Kofod, G., 2001. Dielectric elastomer actuators. Ph.D. thesis, The Technical University of Denmark, Denmark.

Kofod, G., Sommer-Larsen, P., Kornbluh, R. and Pelrine, R., 2003. Actuation response of polyacrylate dielectric elastomers. J. Intell. Mater. Syst. Struct. **14**, 787-793.

Koh, S. J. A., Li, T., Zhou, J., Zhao, X., Hong, W., Zhu, J. and Suo, Z., 2011a. Mechanisms of large actuation strain in dielectric elastomers. J. Polym. Sci. B **49**, 504-515.

Koh, S. J. A., Keplinger, C., Li, T., Bauer, S. and Suo, Z., 2011b. Dielectric elastomer generators: How much energy can be converted? IEEE/ASME Transactions on Mechatronics **16**, 33-41.

Kollosche, M., Zhu, J., Suo, Z. and Kofod, G., 2012. Complex interplay of nonlinear processes in dielectric elastomers. Phys. Rev. E **85**, 051801.

Kornbluh, R., Pelrine, R., Joseph, J., Heydt, R., Pei, Q. and Chiba, S., 1999. High-field electrostriction of elastomeric polymer dielectrics for actuation. Proc. SPIE **3669**, 149-161.

Leng, J., Liu, L., Liu, Y., Yu, K. and Sun, S., 2009. Electromechanical stability of dielectric elastomer. Appl. Phys. Lett. **94**, 211901.

Li, B., Liu, L. and Suo, Z., 2011. Externsion limit, polarization saturation, and snap-through instability of dielectric elastomers. International Journal of Smart and Nano Materials **2**, 59-67.

Pelrine, R., Kornbluh, R., Pei, Q. and Joseph, J., 2000. High-speed electrically actuated elastomers with greater than 100%. Science **287**, 836-839.

Pelrine, R., Kornbluh, R. D., Pei, Q., Stanford, S., Oh, S., Eckerle, J., Full, R., Rosenthal, M. and Meijer, K., 2002. Dielectric elastomer artificial muscle actuators: toward biomimetic motion. Proc. SPIE **4695**, 126-137.

Pelrine, R. E., Kornbluh, R. D. and Joseph, J. P., 1998. Electrostriction of polymer dielectrics with compliant electrodes as a means of actuation. Sens. Actuators A **64**, 77-85.

Plante, J. and Dubowsky, S., 2006. Large-scale failure modes of dielectric elastomer actuators. Int. J. Solids Struct. **43**, 7727–7751.

Shankar, R., Ghosh, T. K. and Spontak, R.J., 2007. Electroactive nanostructured polymers as tunable actuators. Adv. Mater. **19**, 2218-2223.

Stoyanov, H., Kodod, G. and Gerhard, R. 2008. A co-axial dielectric elastomer actuator. Adv. Sci. Tech. **61**, 81-84.

Suo, Z., 2010. Theory of dielectric elastomers. Acta Mechanica Solida Sinica **23**, 549-578.

Suo, Z. and Zhu, J., 2009. Dielectric elastomers of interpenetrating networks. Appl. Phys. Lett. **95**, 232909.

Wissler, M. and Mazza, E., 2005. Modeling of a pre-strained circular actuator made of dielectric elastomers. Sens. Actuators A **120**, 184-192.

Wissler, M. and Mazza, E., 2007. Mechanical behaviour of an acrylic elastomer used in dielectric elastomer actuators. Sens. Actuators A **134**, 494–504.

Zhao, X., Hong, W. and Suo, Z., 2007. Electromechanical hysteresis and coexistent statesin dielectric elastomers. Phys. Rev. B **76**, 134113.

Zhao, X. and Suo, Z., 2010. Theory of dielectric elastomers capable of giant deformation of actuation. Physical Phys. Rev. Lett. **104**, 178302.

Zhu, J., Stoyanov, H., Kofod, G. and Suo, Z., 2010. Large deformation and electromechanical instability of a dielectric elastomer tube actuator. J. Appl. Phys. **108**, 074113.

Chapter 4

4 Electromechanical response and failure modes of a dielectric elastomer tube actuator with boundary constraints

4.1 Introduction

As one of the promising actuation materials capable of converting electrical energy to mechanical energy, dielectric elastomers (DEs) have received much attention in recent years. DEs are generally characterized by their softness, flexibility, and large deformation capability that are not possessed by conventional materials in transduction technologies, such as piezoelectric materials. Due to these unique properties desirable for actuation, DEs have been widely used to design functional DE actuators with different configurations in practical applications, such as MEMS, artificial muscles, soft robots, adaptive optical elements, programmable haptic surfaces, portable force feedback device, binary actuation, prosthetics, orthotics and other biomimetic applications (Carpi *et al*., 2008; Kornbluh *et al*., 2002; O'Halloran *et al*., 2008; Carpi *et al*., 2007; Pei *et al*., 2004). Depending on the particular application, the DE actuators have been designed as stack, extender, bimorph, unimorph, diaphragm, plate, tube, etc (Carpi *et al*., 2008; Kornbluh *et al*., 2002; O'Halloran *et al*., 2008; Carpi *et al*., 2007; Pei *et al*., 2004; Zhu *et al*., 2010a and 2010b; Cameron *et al*., 2008; Pelrine *et al*., 2002).

In order to achieve reliable designs of DE actuators, significant efforts have been devoted to understanding their actuation mechanisms. Early models simplified the electromechanical coupling of the materials by extending elasticity theory (Pelrine et al., 1998) for small deformation and hyperelasticity theory (Pelrine *et al*., 2000; Goulbourne *et al*., 2005) for finite deformation into dielectrics with the addition of an empirical Maxwell stress. The analyses based on these models could only explain experimental phenomena for some particular cases. Later, fully coupled nonlinear field theories for dielectric elastomers with the capability of capturing finite deformation were developed

(McMeeking and Landis, 2005; Dorfmann and Ogden, 2005; Suo *et al*., 2008). These coupled nonlinear theories have been implemented to rigorously predict the actuation performance of selected actuator configurations (Zhao *et al*., 2007; Zhao and Suo, 2007; Zhao and Suo, 2008a; Zhou *et al*., 2008). Moreover, these nonlinear field theories have laid the foundation for employing finite-element methods to computationally simulate homogeneous and especially inhomogeneous deformation of DEs (Zhao and Suo, 2008a; Zhou *et al*., 2008; Park *et al*., 2012). Based on the nonlinear field theory proposed by Suo *et al*. (2008), recent models accounted for the DEs' viscoelastic properties, which were shown to strongly affect their dynamic performance (Hong, 2011; Park and Nguyen, 2013) in some experimental studies. Regardless of mechanical rupture, it was reported in these existing studies that the failure modes of DE actuators were mainly governed by electrical breakdown (EB) and electromechanical instability (EMI). Electrical breakdown occurs once the electric field in the dielectric exceeds its electrical strength. Electromechanical instability, also known as the pull-in instability, is the result of the applied voltage causing excessive thinning of the DE, leading to premature electrical breakdown, which inhibits further mechanical deformation. The EMI of planar DE actuators has been well studied in the open literature (Lu *et al*., 2012 Li *et al*., 2011; Plante and Dubowsky, 2006; Zhao and Suo, 2008b; Wissler and Mazza, 2005).

Among various configurations of DE actuators is the cylindrical one, first proposed by Pelrine *et al*. (1998), which is also called as DE tube actuator. DE tube actuators have wider applications, and are less bulky compared to DE actuators with other configurations (for example, plate or membrane actuators) (Cameron *et al*., 2008; Stoyanov *et al*., 2008; Huang *et al*., 2012; Arora *et al*., 2007). Figure 4.1(a) depicts a DE tube hanging on a fixed wall and coated with compliant electrodes on both its inner and outer surfaces, which is based on the schematic of the DE tube actuator in the work of Zhu *et al*. (2010b). When subject to a voltage between the two electrodes, the DE tube exhibits a reduction in its thickness and an elongation in the axial direction. The elongation ratio of the DE tube depends on its dimensions (Pelrine *et al*., 1998; Huang *et al*., 2012). Early modeling of the DE tube actuator by Carpi and Rossi (2004) was based on the theory of infinitesimal deformation. Such a model, which assumes a linear stress-strain constitutive relation of the material, is reliable only when the actuation deformation is relatively small. Recently, Zhu *et al*. (2010b) conducted a theoretical analysis on a DE tube actuator with finite deformation by employing the neo-Hookean constitutive model. Their work revealed that the DE tube actuator was also susceptible to the EMI. Since the merit of DE actuators mainly lies in their large deformation capability in applications, uncovering possible methods to avoid the EMI while achieving larger actuation is a crucial issue, which has attracted much interest. It is well established that the EMI can be suppressed or eliminated either by pre-stretching the DEs before the voltage is applied (Lu *et al*., 2012; Koh *et al*., 2011; Pelrine *et al*., 2000), or restraining the stretch limit of the DEs by adding interpenetrating networks (Ha *et al*., 2006; Suo and Zhu, 2009). However, the EMI issue is still not entirely settled because these two methods are either limited to a particular range of applications or difficult to manage (Suo and Zhu, 2009; Zhao and Suo, 2010). Therefore, an alternative method to avoid the EMI of a DE tube actuator is the main focus of the current work. The tube configuration studied by Zhu *et al*. (2010b) will be revisited to uncover possible mechanisms of the DE tube actuators without the EMI failure. Following the methodology previously developed for a DE plate actuator (Zhou *et al*., 2013), the electromechanical response of a DE tube actuator with and without boundary constraints will be investigated to reveal how the EMI is affected by boundary constraints. Meanwhile, some other possible failure modes that may occur during the actuation of the DE tube will also be analyzed.

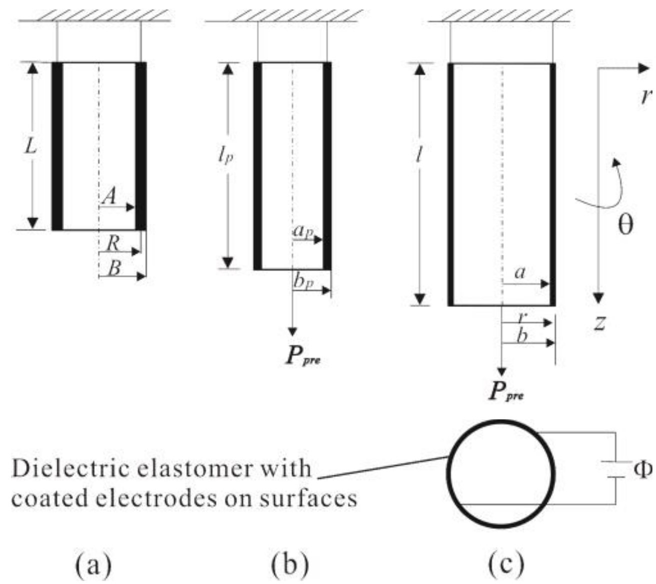

Figure 4.1 Actuation of a DE tube actuator: (a) undeformed state; (b) pre-stretched state under a mechanical pre-stretch force P_{pre}; (c) deformed state under a mechanical pre-stretch force P_{pre} and an electric voltage Φ.

4.2 Actuation of an unconstrained DE tube under axial stretch

To investigate how the EMI is affected by boundary constraints, the DE tube actuator studied by Zhu *et al*. (2010b) is revisited by first considering its electromechanical response without boundary constraints. As shown in Figure 4.1(a), in the undeformed state, L, A and B denote the length, the inner radius and the outer radius of the tube, respectively. Under an axial load P_{pre} (Figure 4.1(b)), the tube deforms to the pre-stretched state with the length l_p, the inner radius a_p, the outer radius b_p and the pre-stretch ratio $\lambda_{pre}=l_p/L$. Then, a voltage Φ is applied between the inner and outer surfaces of the tube, forcing the tube to deform to the current state (Figure 4.1(c)) with the length l, the inner radius a, the outer radius b and the axial stretch ratio $\lambda_z=l/L$. During the deformation process, an arbitrary material point moves from radial position R in the undeformed state to radial position r in the current state. The DEs are commonly assumed to be incompressible (Zhu *et al*., 2010b; Koh *et al*., 2011; Pelrine *et al*., 2000; Huang and Suo, 2011). Thus,

$$\left(B^2 - A^2\right) = \lambda_z \left(b^2 - a^2\right). \tag{4.1}$$

From equation (4.1), the hoop stretch of the tube, defined by $\lambda_\theta = r/R$ for a material point, can be written in terms of the axial stretch as

$$\lambda_\theta = \frac{r}{\sqrt{A^2 + \lambda_z\left(r^2 - a^2\right)}}. \tag{4.2}$$

Moreover, the incompressibility of the material, i.e., $\lambda_r \lambda_\theta \lambda_z = 1$, gives the radial stretch of the tube in terms of the axial stretch.

The applied voltage, $\Phi = V(\mathrm{b}) - V(\mathrm{a})$, induces an electric field E in the radial direction, which can be expressed in terms of the electric potential $V(r)$ according to Maxwell's law:

$$E = -\mathrm{d}V / \mathrm{d}r. \tag{4.3}$$

Also, the electric field is associated with the electric displacement D as (Zhu *et al*., 2010b; Huang and Suo, 2011)

$$D = \varepsilon \varepsilon_0 E, \tag{4.4}$$

where ε_0 is the permittivity of air or vacuum and ε is the relative dielectric constant of the DE. Gauss's law requires that the divergence of the electric displacement equals to the density of free charge in the volume of the dielectric medium. Since the electric displacement D is only in the radial direction in this case, the free charge density q equals to $\mathrm{d}D/\mathrm{d}r$, which leads to

$$D = \frac{Q}{2\pi r \lambda_z L} \tag{4.5}$$

for the electric displacement distribution, with Q being the charge on the outer surface of the tube (Zhu *et al*., 2010b). Combining equations (4.3), (4.4) and (4.5), and integrating equation (4.3) from the inner radius a to the outer radius b yields

$$\Phi = \frac{Q}{2\pi\lambda_z L\varepsilon\varepsilon_0}\ln\frac{b}{a} \tag{4.6}$$

For the DE tube actuator in Figure 4.1, the constitutive equation relates the stress components in the r-, θ-, z-directions through (Zhu *et al*., 2010b; Huang and Suo, 2011)

$$\sigma_\theta - \sigma_r + \varepsilon\varepsilon_0 E^2 = \lambda_\theta \frac{\partial W_s\left(\lambda_\theta, \lambda_z\right)}{\partial\lambda_\theta}, \tag{4.7}$$

$$\sigma_z - \sigma_r + \varepsilon\varepsilon_0 E^2 = \lambda_z \frac{\partial W_s\left(\lambda_\theta, \lambda_z\right)}{\partial\lambda_z}. \tag{4.8}$$

$W(\lambda_\theta, \lambda_z)$ is the elastic strain energy density function of the elastomer. Among the constitutive models of rubber elasticity (Boyce and Arruda, 2000), the Gent model (Gent, 1996) is one that accounts for the effect of extensibility, with the strain energy density function given by

$$W_s = -\frac{GJ_{\lim}}{2}\ln\left(1-\frac{\lambda_\theta^{-2}\lambda_z^{-2}+\lambda_\theta^2+\lambda_z^2-3}{J_{\lim}}\right). \tag{4.9}$$

where G is the shear modulus, and $J_{\lim}$ is a dimensionless parameter related to the extensibility (stretching limit) of the material (Boyce and Arruda, 2000; Gent, 1996). The value of $J_{\lim}$ may change corresponding to the extensibility of the polymer chains in the DE. For example, Kollosche *et al*. (2012) set $J_{\lim}$=125 for an acrylic elastomer VHB4905 produced by 3M. Lu *et al*. (2012) used $J_{\lim}$ =120 for both VHB4905 and VHB4910 produced by 3M. Nevertheless, Huang and Suo (2011) set $J_{\lim}$ =69 for a dielectric elastomer for theoretical modeling purpose. As VHB4905 and VHB4910 are the most commonly studied dielectric elastomers in literature, J_{lim}=125 is set in our work for simulation purpose. Combining equations (4.7), (4.8) and (4.9) gives that

$$\sigma_\theta - \sigma_r = GJ_{\mathrm{lim}} \frac{\lambda_\theta^2 - \lambda_\theta^{-2}\lambda_z^{-2}}{J_{\mathrm{lim}} - \lambda_z^2 - \lambda_\theta^2 - \lambda_\theta^{-2}\lambda_z^{-2} + 3} - \varepsilon\varepsilon_0 E^2, \tag{4.10}$$

$$\sigma_z - \sigma_r = GJ_{\mathrm{lim}} \frac{\lambda_z^2 - \lambda_\theta^{-2}\lambda_z^{-2}}{J_{\mathrm{lim}} - \lambda_z^2 - \lambda_\theta^2 - \lambda_\theta^{-2}\lambda_z^{-2} + 3} - \varepsilon\varepsilon_0 E^2 . \tag{4.11}$$

In the deformed state of the DE tube actuator in Figure 4.1(c), the mechanical equilibrium requires:

$$\frac{\mathrm{d}\sigma_r}{\mathrm{d}r} + \frac{\sigma_r - \sigma_\theta}{r} = 0 . \tag{4.12}$$

Substituting equation (4.10) into equation (4.12), replacing λ_θ and E through equations (4.2), (4.4) and (4.5), and integrating equation (4.12) from *a* to *b* yields that

$$\sigma_r(b) - \sigma_r(a) = \int_a^b \frac{-Q^2}{4\pi^2\lambda_z^2 L^2 \varepsilon\varepsilon_0 r^3} dr + \int_a^b \frac{\dfrac{GJ_{\mathrm{lim}} r}{A^2 + \lambda_z\left(r^2 - a^2\right)} - GJ_{\mathrm{lim}}\lambda_z^{-2}\dfrac{A^2 + \lambda_z\left(r^2 - a^2\right)}{r^3}}{J_{\mathrm{lim}} - \lambda_z^2 - \dfrac{r^2}{A^2 + \lambda_z\left(r^2 - a^2\right)} - \lambda_z^{-2}\dfrac{A^2 + \lambda_z\left(r^2 - a^2\right)}{r^2} + 3} dr , \tag{4.13}$$

Since the inner and outer surfaces of the DE tube are assumed to be stress free, i.e., $\sigma_r(a)=\sigma_r(b)=0$, then equation (4.13) gives

$$Q = 2\pi\lambda_z L\sqrt{2\varepsilon\varepsilon_0 GJ_{\mathrm{lim}}}\sqrt{\frac{F_1}{a^{-2} - b^{-2}}} , \tag{4.14}$$

where

$$F_1 = \ln\frac{b}{a} + \frac{1}{4}\ln\frac{m_2 a^4 + m_1 m_2 a^2 - m_1^2}{m_2 b^4 + m_1 m_2 b^2 - m_1^2} + \frac{2m_1 + \dfrac{m_1 m_2}{2}}{\sqrt{4m_1^2 m_2 + m_1^2 m_2^2}}\left[\arctan\left(\frac{2m_2 b^2 + m_1 m_2}{\sqrt{4m_1^2 m_2 + m_1^2 m_2^2}}\right) - \arctan\left(\frac{2m_2 a^2 + m_1 m_2}{\sqrt{4m_1^2 m_2 + m_1^2 m_2^2}}\right)\right],$$

$m_1=A^2/\lambda_z-a^2$ and $m_2=J_{\lim}\lambda_z+3\lambda_z-\lambda_z^3-2$. Inserting expression (4.14) into equation (4.6), the applied voltage can be related to the tube deformation, i.e.,

$$\frac{\Phi}{B-A}\sqrt{\frac{\varepsilon\varepsilon_0}{G}}=\ln\frac{b}{a}\sqrt{\frac{2J_{\lim}}{\left(B-A\right)^2}}\sqrt{\frac{F_1}{a^{-2}-b^{-2}}}\ . \tag{4.15}$$

Similarly, the radial stress $\sigma_r(r)$ can be obtained at any position. Then inserting $\sigma_r(r)$ into equations (4.10) and (4.11), the distribution of the axial stress $\sigma_z(r)$ and hoop stress $\sigma_\theta(r)$ can be determined. Correspondingly, the equivalent axial force P_{pre} is expressed as

$$P_{\text{pre}}=\int_a^b 2\pi r\sigma_z(r)dr=2\pi GJ_{\lim}\left\{\frac{a^2b^2\ln\frac{b}{a}\left(2m_1+\frac{m_1m_2}{2}\right)+\left(a^2-b^2\right)\left(\frac{m_1^2}{2}-\frac{m_1^2m_3}{m_2}\right)}{\left(a^2-b^2\right)\sqrt{4m_1^2m_2+m_1^2m_2^2}}\left[\arctan\left(\frac{2m_2b^2+m_1m_2}{\sqrt{4m_1^2m_2+m_1^2m_2^2}}\right)\right.\right.$$
$$\left.\left.-\arctan\left(\frac{2m_2a^2+m_1m_2}{\sqrt{4m_1^2m_2+m_1^2m_2^2}}\right)\right]+\frac{a^2b^2\ln^2\frac{b}{a}}{a^2-b^2}-\frac{m_3}{2m_2}\left(a^2-b^2\right)+\frac{a^2b^2\ln\frac{b}{a}}{4\left(a^2-b^2\right)}\ln\frac{m_2a^4+m_1m_2a^2-m_1^2}{m_2b^4+m_1m_2b^2-m_1^2}\right\}. \tag{4.16}$$

Equation (4.16) relates the mechanical load P_{pre} to the deformation of the DE tube. The coupled equations (4.15) and (4.16) govern the electromechanical response of the DE tube actuator. Noting that b is a function of a and λ_z from equation (4.1), once P_{pre} and Φ are prescribed, the deformation of the tube can be determined by solving for a and λ_z from equations (4.15) and (4.16). Here, it is more convenient to prescribe the pre-stretch load P_{pre} by defining a pre-stretch ratio λ_{pre}. Due to the homogeneous deformation in the pre-stretched state (Figure 4.1(b)), the stretching of the tube is determined as $\lambda_{\text{pre}}=l_p/L$ and $\lambda_r=\lambda_\theta=\lambda_z^{-1/2}$. Correspondingly, the pre-stretch load P_{pre} can be expressed in terms of the pre-stretch ratio λ_{pre} by combining equations (4.1), (4.11) and (4.16) with the condition that $\Phi=0$, i.e.,

$$P_{\text{pre}}=\pi GJ_{\lim}\left(B^2-A^2\right)\frac{\lambda_{pre}-\left(\lambda_{pre}\right)^{-2}}{J_{\lim}-\left(\lambda_{pre}\right)^2-2\left(\lambda_{pre}\right)^{-1}+3}. \tag{4.17}$$

Figure 4.2 displays the electromechanical response curves of a DE tube at several levels of pre-stretch, namely the $\lambda_z - \Phi\left(\varepsilon\varepsilon_0/G\right)^{0.5}/(B-A)$ curves, in which the applied voltage is expressed as a normalized electrical load $\Phi\left(\varepsilon\varepsilon_0/G\right)^{0.5}/(B-A)$. As shown in Figure 4.2, for a small applied electrical load, the induced axial stretch increases very slowly with the voltage for any pre-stretch ratios. Once the electrical load reaches a peak value, the electromechanical response curve starts to drop down. After the peak, the axial stretch continues to increase until the DE reaches its limit of extensibility, at which the electromechanical response curve becomes vertical. The typical behavior of such an electromechanical response is that the interval between the peak and the trough is unstable, which has been well investigated from perturbation analysis (Huang and Suo, 2011; Leng *et al*., 2009). Therefore, under a voltage-controlled actuation, λ_z may snap through the unstable interval from the peak to the other side of the response curve, following the red arrow as show in Figure 4.2, resulting in a very large actuation strain. Although this snap-through is desirable for achieving large strain, the DE tube may not survive it because of a pre-mature electrical breakdown due to the sudden decrease in the tube thickness. Under this situation, the EMI occurs and the peak of the electromechanical response curve corresponds to the onset of the EMI. From our numerical calculation, the voltage-induced deformation in the radial direction can be interpreted as an "inflation" of the tube, i.e., both *a* and *b* increase as the voltage increases, while a increases at a higher rate than b, leading to the reduction of the tube thickness.

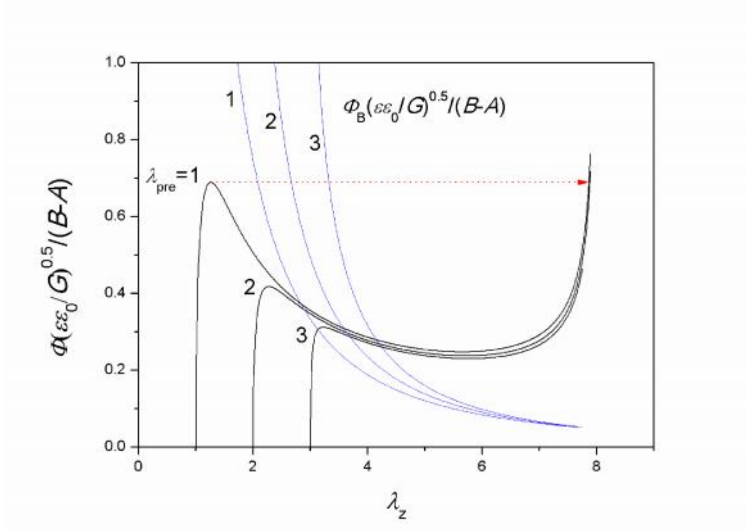

Figure 4.2 Electromechanical response curves and electrical breakdown curves of an unconstrained DE tube.

The electrical breakdown represents a scenario that the voltage-induced electric field exceeds the dielectric strength E_B of the DE, which limits the actuation performance of the DE tube actuator. Although the value of E_B was found to depend on both the thickness and stretch ratios of the DE (Huang *et al*., 2012 Kofod *et al*., 2003), it is still reasonable to use a fixed value in theoretical simulations for the simplification purpose (Li *et al*., 2011; Koh *et al*., 2011; Zhao and Suo, 2010). For the DE tube in Figure 4.1, the voltage corresponding to the electrical breakdown is determined as $\Phi_B = aE_B \ln\left(b/a\right)$. In order to comply with the format of equation (4.15), the breakdown voltage is rewritten as

$$\frac{\Phi_B}{B-A}\sqrt{\frac{\varepsilon\varepsilon_0}{G}} = \frac{da\ln\dfrac{b}{a}}{B-A}, \tag{4.18}$$

by introducing a dimensionless parameter $d = E_B\sqrt{\varepsilon\varepsilon_0/G}$ (Koh *et al*., 2011). The $\lambda_z - \Phi_B\left(\varepsilon\varepsilon_0/G\right)^{0.5}/(B-A)$ curves of the DE tube actuator with different pre-stretch ratios are also plotted in Figure 4.2. In the current work, d=3 is assumed in our numerical calculations to investigate the situation that the EB curve intersects with the unstable interval of the electromechanical response curve, which means that a premature electrical breakdown occurs during the snap-through process. In fact, the EB curve may intersect with the response curve before the EMI onset point when *d* is very small or after the unstable interval when d is exceptionally large (Koh *et al*., 2011; Zhao and Suo, 2010). By setting *d*=3, the failure of the DE tube actuator is purely governed by the premature electrical breakdown caused by the EMI if no mechanical rupture occurs and the axial stretching limit is at the onset of the EMI. Since the stretch at the onset of the EMI is very close to the pre-stretch as observed in this figure, large voltage-induced deformation of such a DE tube is inhibited by the EMI. As mentioned in the previous section, there may be still room to improve the performance of such a DE tube actuator by applying different pre-stretch to the DE tube or changing the material stretching limit J_{lim} (Lu *et al*., 2012; Koh *et al*., 2011; Pelrine *et al*., 2000). In this work, however, we will explore an alternative way to suppress the EMI and improve the performance by controlling the boundary constraints of the DE tube actuator.

4.3 Actuation of n constrained DE tube under axial stretch

To see how electromechanical response of a DE tube actuator can be affected by boundary constraints, a rigid sleeve is artificially set around the DE tube after the pre-stretch (Figure 4.3(b)). The inner radius of the sleeve r_s is set as $r_s=b_{onset}$, where b_{onset} is the outer radius of the unconstrained tube when it reaches the onset of the EMI under an electrical load. The inner surface of the sleeve is assumed to be perfectly smooth that the DE tube can slide along the sleeve without being affected by friction. After the sleeve is placed, a voltage is applied between the two surfaces of the tube, resulting in the inflation of the tube. During the inflation, the outer surface of the DE tube keeps increasing with the increase of the applied voltage until it reaches the sleeve. Before the DE tube touches the sleeve, the electromechanical response is still governed by equations (4.15) and (4.16). Once the DE tube is against the sleeve, the outer surface of the tube is no longer free and the charge Q on the outer surface cannot be expressed as that in equation (4.14). However, after obtaining $\pm_z(r)$ as that in the previous section, Q_c at the constrained state can be solved from the following condition,

$$P_{\text{pre}} = \int_a^{b_{onset}} 2\text{®} r \pm_z \left(r\right) dr \,, \tag{4.19}$$

i.e.,

$$Q_c = 2\text{ª}_z L\sqrt{\text{®££}_0}\sqrt{\frac{P_{\text{pre}} + \text{®} G J_{\text{lim}} F_2}{\ln\frac{a}{b_{onset}} + \frac{1}{2} - \frac{b_{onset}^{\;2}}{2a^2}}} \,, \tag{4.20}$$

where

$$\begin{aligned} F_2 = {} & \frac{b_{onset}^2}{4}\ln\frac{m_2 b_{onset}^4 + m_1 m_2 b_{onset}^2 - m_1^2}{m_2 a^4 + m_1 m_2 a^2 - m_1^2} - h^2\left(\ln\frac{b_{onset}}{a} + \frac{m_3}{m_2}\right) + a^2\frac{m_3}{m_2} \\ & - \frac{\left(2m_1 b_{onset}^2 + \frac{m_1 m_2 b_{onset}^2}{2} + m_1^2 - \frac{2m_1^2 m_3}{m_2}\right)}{\sqrt{4m_1^2 m_2 + m_1^2 m_2^2}}\left[\arctan\left(\frac{2m_2 b_{onset}^2 + m_1 m_2}{\sqrt{4m_1^2 m_2 + m_1^2 m_2^2}}\right) - \arctan\left(\frac{2m_2 a^2 + m_1 m_2}{\sqrt{4m_1^2 m_2 + m_1^2 m_2^2}}\right)\right] \end{aligned}$$

and P_{pre} is prescribed by equation (4.17). Substituting equation (4.20) into equation (4.6), we can obtain

$$\frac{\text{c}}{B-A}\sqrt{\frac{\text{££}_0}{G}} = \frac{\sqrt{1/\text{®}G}}{B-A}\ln\frac{b_{onset}}{a}\sqrt{\frac{P_{\text{pre}} + \text{®} G J_{\text{lim}} F_2}{\ln\frac{a}{b_{onset}} + \frac{1}{2} - \frac{b_{onset}^2}{2a^2}}} \,, \tag{4.21}$$

which governs the electromechanical response of the DE tube after the tube reaches the sleeve. Note that a can be expressed as a function of ª_z by letting $b = b_{\text{onset}}$ in equation (4.1). For a constrained DE tube shown in Figure 4.3, the electrical breakdown voltage can still be determined by equation (4.18) if the EB happens before the tube reaches the sleeve. Otherwise, the electrical breakdown voltage is determined as

$$\frac{\text{c}_B}{B-A}\sqrt{\frac{\text{££}_0}{G}} = \frac{da\ln\frac{b_{onset}}{a}}{B-A} \,. \tag{4.22}$$

The electromechanical response of a constrained DE tube is illustrated in Figure 4.4. The monotonic response curves indicate the elimination of the EMI. In comparison with Figure 4.2, it is observed that all the intersection points between the electrical breakdown curves and the electromechanical response curves have been shifted significantly to a larger axial stretch ratio. Therefore, the EB is postponed for a constrained DE tube compared to an unconstrained one. The results in this figure reflect an improvement of the actuation performance in the axial direction by constraining the DE tube boundary in the radial direction.

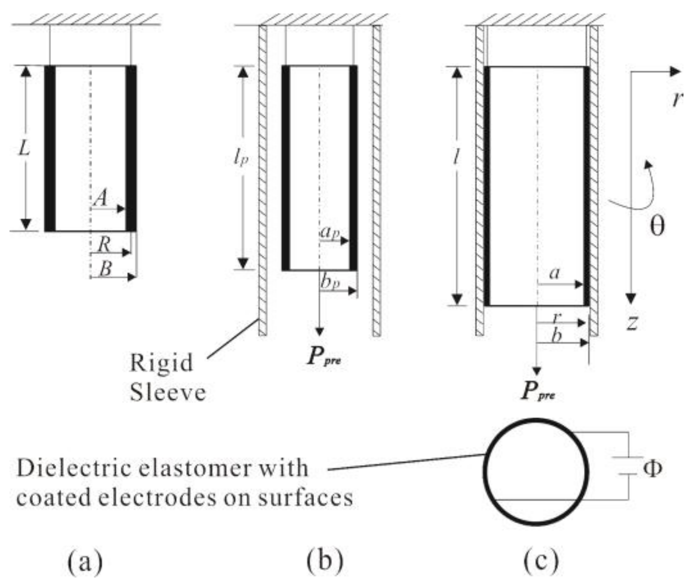

Figure 4.3 Actuation of a DE tube actuator constrained on its outer surface: (a) undeformed state; (b) a rigid sleeve is placed around the pre-stretched DE tube under force P_{pre}; (c) deformed state under a mechanical pre-stretch force P_{pre} and an electric voltage c.

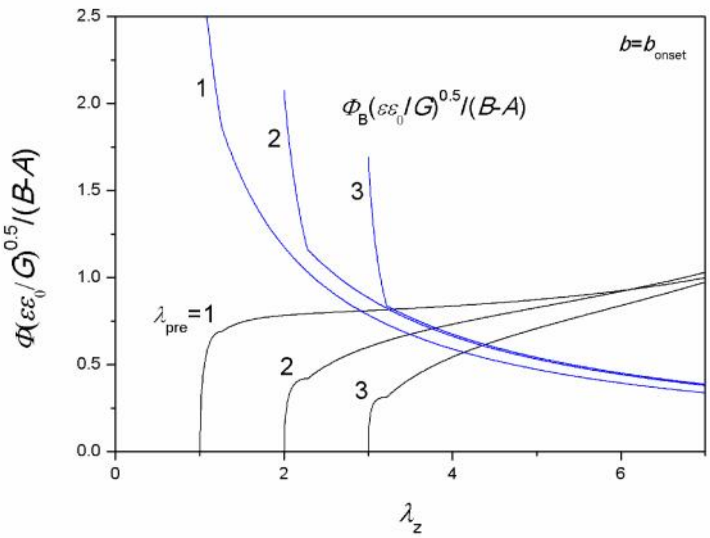

Figure 4.4 Electromechanical response curves and electrical breakdown curves of a DE tube actuator with boundary constraints on its outer surface.

In order to see how the boundary constrain improve the actuation performance of the DE tube actuator, we plot in Figure 4.5 ª$_{EB}$-ª$_{pre}$ as a function of ª$_{pre}$. Here, ª$_{EB}$ is the axial stretch ratio when the EB occurs and ª$_{EB}$-ª$_{pre}$ represents the voltage-induced stretch ratio, namely, the actuation stretch ratio. As shown in this figure, the actuation performance of the constrained DE tube is significantly improved, especially for the tube with small mechanical pre-stretch or even without pre-stretch. For example, when the pre-stretch ratio is set as ª$_{pre}$=1 (no pre-stretch), the actuation stretch ratio increases from 0.26 to 1.87 i.e., it is improved over 600%.

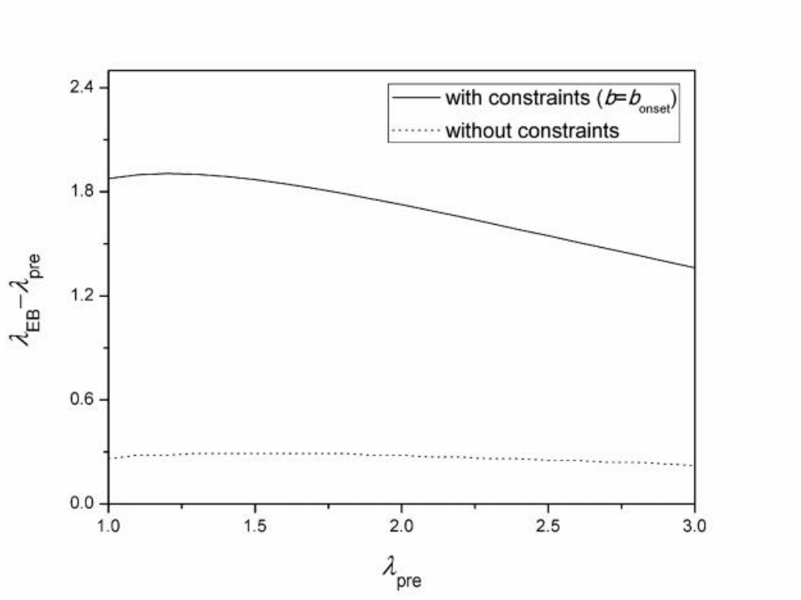

Figure 4.5 Comparison of actuation stretch at EB (λ_{EB}-λ_{pre}) for a DE tube actuator with and without boundary constraints.

It should be mentioned that the predicted performance improvement in Figure 4.5 is based on the assumption that the failure of the DE tube actuator is governed by the EB. However, as the rigid sleeve restraints the inflation of the tube, the DE tube is under uniform radial pressure generated by the rigid sleeve. Such a radial pressure may cause the tube to collapse because of mechanical buckling. Inserting equations (4.2), (4.4), (4.5) and (4.10) into equation (4.12) and conducting integration of r from a to b_{onset}, the radial pressure is determined as,

$$\sigma_{in} = \frac{Q^2}{8\pi^2\lambda_z^2 L^2 \varepsilon\varepsilon_0}\left(b_{onset}^{-2} - a^{-2}\right) + GJ_{\lim}\left\{\ln\frac{b_{onset}}{a} - \frac{1}{4}\ln\frac{m_2 a^4 + m_1 m_2 a^2 - m_1^2}{m_2 b_{onset}^4 + m_1 m_2 b_{onset}^2 - m_1^2} + \frac{2m_1 + \frac{m_1 m_2}{2}}{\sqrt{4m_1^2 m_2 + m_1^2 m_2^2}}\left[\arctan\left(\frac{2m_2 b_{onset}^2 + m_1 m_2}{\sqrt{4m_1^2 m_2 + m_1^2 m_2^2}}\right) - \arctan\left(\frac{2m_2 a^2 + m_1 m_2}{\sqrt{4m_1^2 m_2 + m_1^2 m_2^2}}\right)\right]\right\}, \quad (4.23)$$

In this case, the buckling of the constrained tube can be treated as the buckling of a thin-walled cylindrical shell under uniform radial pressure. According to studies on the stability of thin-walled cylindrical shells (Teng and Rotter, 2004; Ross, 2011; Brush and Almroth, 1975), although a great number of methods are available for estimating the critical stress of the buckling of cylindrical shells with different dimensions, some methods appear to be more accurate for some particular cases. Among these methods for buckling of cylindrical shells under uniform radial pressure, a solution based on the Donnell stability equations is relatively accurate for short or shallow cylindrical shells, in which the critical stress of buckling was given as

$$\sigma_{cr}=\frac{E_Y(b_{onset}-a)\left\{\left[\frac{\pi(b_{onset}+a)}{2L\lambda_z}\right]^2+n^2\right\}^2\left[\frac{2(b_{onset}-a)}{b_{onset}+a}\right]^2}{6n^2\left(1-\nu^2\right)(b_{onset}+a)}+\frac{2E_Y(b_{onset}-a)\left[\frac{\pi(b_{onset}+a)}{2L\lambda_z}\right]^4}{(b_{onset}+a)n^2\left\{\left[\frac{\pi(b_{onset}+a)}{2L\lambda_z}\right]^2+n^2\right\}^2}, \quad (4.24)$$

where E_Y is the Young's modulus, ν is the Poisson's ratio, and n is the number of circumferential waves into which the tube buckles (Brush and Almroth, 1975). The value of n corresponding to the minimum value of the critical stress is selected in our numerical calculation. When $\sigma_{in}=\sigma_{cr}$, buckling occurs and the axial stretch ratio at failure can be obtained by combining equations (4.24) and (4.25). Figure 4.6 plots $\lambda_{fail}-\lambda_{pre}$ as a function of λ_{pre}, where λ_{fail} refers to the axial stretch ratio at mechanical buckling for a constrained DE tube while it refers to the EB for an unconstrained DE tube. For a constrained DE tube in this case, the actuation stretch in Figure 4.6 is much smaller than that in Figure 4.5, which indicates that the actual failure mode for such a DE tube is mechanical buckling. However, the performance of the actuation is still improved by employing boundary constraints even with the consideration of the mechanical buckling, particularly when the pre-stretch is small. For example, when λ_{pre}=1, the actuation stretch ratio increases over 20%. As the pre-stretch increases to some extent, the actuation stretch of a constrained DE tube does not significantly differ from that of an unconstrained DE tube. It should be mentioned that the Donnell equations are accurate when the tube is relatively short or shallow; longer cylindrical shells are less resistant against uniform radial pressure and more susceptible to the mechanical buckling failure. When considering tubes with different dimensions, say, long tubes, one may employ other buckling solutions to obtain the critical buckling stress (Teng and Rotter, 2004; Ross, 2011; Brush and Almroth, 1975). However, the resistance against the mechanical buckling of the tubes can be enhanced by applying reinforcement to the DE tube, for example, by introducing stiffening rings to the relatively long tubes. Alternatively, using a stack of short tubes instead of a single long tube can also improve the performance of the constrained DE tube actuators. Based on the analysis above, we can conclude that applying boundary constraints to the DE tube can offer an alternative to eliminating the EMI failure and improving the actuation performance, as was also theoretically verified on a DE plate actuator (Zhou *et al*., 2013). It should be mentioned that there is no existing experimental work in literature that can directly confirm the results of the boundary constraint method as proposed in the current work. However, the simulation results in this work could be in-directly verified by the experimental observation (Huang *et al*., 2012). It was found in their work that a larger axial actuation was achieved by using stiff, parallel fibers to constrain the tube deformation in the radial direction of the DE tube actuator. In fact, both the fiber constraints employed in the work of Huang *et al*. (2012) and boundary-constraint method in the current work intend to use a similar idea to restrict the radial deformation in order to realize a larger axial strain of a DE tube under an applied voltage. It is anticipated that these two methods will lead to similar results. Nevertheless, the realization of applying boundary constrains is challenging, experimental validation against the theoretical modeling in the current work still needs to be further pursued, which is our future concentration.

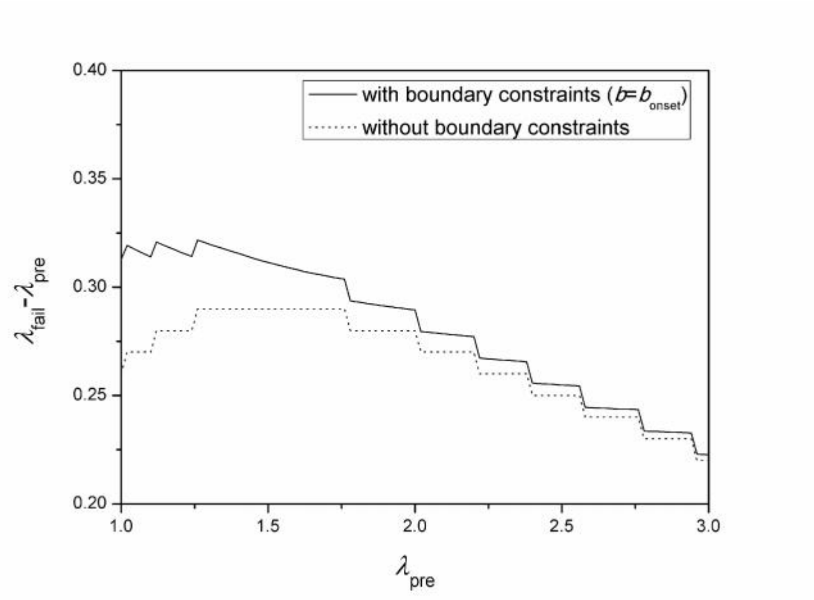

Figure 4.6 Comparison of actuation stretch at failure (a_{fail}-a_{pre}) for a DE tube actuator with and without boundary constraints.

4.4 Conclusion

This work investigates the electromechanical response of a DE tube actuator based on the Gent model for hyperelastic materials. The performance of the DE tube actuator is found to be significantly affected by the EMI, which inhibits the full actuation by causing a premature EB. In order to eliminate or suppress the EMI, a boundary-constraint method is proposed. By applying boundary constraints to the DE tube, monotonic response curves are obtained and larger axial actuation stretch can be achieved. Because of the boundary constraints, consideration has also been given to the possible mechanical buckling failure that may occur during the actuation process. Simulation results indicate that the actuation stretch can be improved by boundary constraints even if buckling failure is taken into account. However, it should also be mentioned that how to realize the boundary constraints in reality is challenging and further experiments are needed to validate the theoretical modeling results. This work is expected to provide a better understanding on the electromechanical responses of the DEs and thus lead to better design of the DE actuators with desirable actuation performance.

References

Arora, S., Ghosh, T. and Muth, J., 2007. Dielectric elastomer based prototype fiber actuators. Sens. Actuator A **136**, 321-328.

Boyce, M. C. and Arruda, E. M., 2000. Constitutive models of rubber elasticity: a review. Rubber Chem. Technol. **73**, 504–523.

Brush, D. O. and Almroth, B. O., 1975. Buckling of Bars, Plates, and Shells. McGraw-Hill, New York. pp 142-166.

Cameron, C. G., Szabo, J. P., Johnstone, S., Massey, J. and Leidner, J., 2008. Linear actuation in coextruded dielectric elastomer tubes. Sens. Actuator A **147**, 286–291.

Carpi, F. and Rossi, D. D., 2004. Dielectric elastomer cylindrical actuators: electromechanical modelling and experimental evaluation. Mater. Sci. Eng. C **24**, 555-562.

Carpi, F., Rossi, D. D., Kornbluh, R., Pelrine, R. and Sommer-Larsen, P., 2008. Dielectric Elatomers as Electromechanical Transducers. Elsevier, Amsterdam.

Carpi, F., Salaris, C. and Rossi, D. D., 2007. Folded dielectric elastomer actuators Smart Mater. Struct. **16**, S300–305.

Dorfmann, A. and Ogden, R. W., 2005. Nonlinear electroelasticity. Acta Mech. **174**, 167–183.

Gent, A. N., 1996. A new constitutive relation for rubber. Rubber Chem. Technol. **69**, 59-61.

Goulbourne, N., Mockensturm, E. and Frecker, M., 2005. A nonlinear model for dielectric elastomer membranes. J. Appl. Mech. **72**, 899-906.

Ha, S. M., Yuan, W., Pei, Q., Pelrine, R. and Stanford, S., 2006. Interpenetrating polymer networks for high-performance electroelastomer artificial muscles. Adv. Mater. **18**, 887–891.

Hong, W., 2011. Modeling viscoelastic dielectrics. J. Mech. Phys. Solids **59**, 637-650.

Huang, J., Lu, T., Zhu, J., Clarke, D. R. and Suo, Z., 2012. Large, uni-directional actuation in dielectric elastomers achieved by fiber stiffening. Appl. Phys. Lett. **100**, 211901.

Huang, J., Shian, S., Diebold, R. M., Suo, Z. and Clarke, D. R., 2012. The thickness and stretch dependence of the electrical breakdown strength of an acrylic dielectric elastomer. Appl. Phys. Lett. **101** 122905.

Huang, R. and Suo, Z., 2011. Electromechanical phase transition in dielectric elastomers. Proc. R. Soc. A **468**, 1014–1040.

Kofod, G., Sommer-Larsen, P., Kornbluh, R. and Pelrine, R., 2003. Actuation response of polyacrylate dielectric elastomers. J. Intell. Mater. Syst. Struct. **24**, 1667–1674.

Koh, S. J. A., Li, T., Zhou, J., Zhao, X., Hong, W., Zhu, J. and Suo, Z., 2011. Mechanisms of large actuation strain in dielectric elastomers. J. Polym. Sci. B **49**, 504–515.

Kollosche, M., Zhu, J., Suo, Z. and Kofod, G., 2012. Complex interplay of nonlinear processes in dielectric elastomers. Phys. Rev. E **85**, 051801.

Kornbluh, R., Pelrine, R., Pei, Q., Heydt, R., Stanford, S., Oh, S. and Eckerle, J., 2002. Electroelastomers: applications of dielectric elastomer transducers for actuation, generation and smart structures. Proc. SPIE **4698**, 254–270.

Leng, J., Liu, L., Liu, Y., Yu, Kai. And Sun, S., 2009. Electromechanical stability of dielectric elastomer. Appl. Phys. Lett. **94**, 211901.

Li, B., Liu, L. and Suo, Z., 2011. Externsion limit, polarization saturation, and snap-through instability of dielectric elastomers. International Journal of Smart and Nano Materials 2, 59-67.

Lu, T., Huang, J., Jordi, C., Kovacs, G., Huang, R., Clarke, D. R. and Suo, Z., 2012. Dielectric elastomer actuators under equal-biaxial forces, uniaxial forces, and uniaxial constraint of stiff fibers. Soft Matter **8**, 6167–6173.

McMeeking, R. M. and Landis, C. M., 2005. Electrostatic forces and stored energy for deformable dielectric materials. J. Appl. Mech. **72**, 581–590.

O'Halloran, A., O'Malley, F. and McHugh, P., 2008. A review on dielectric elastomer actuators, technology, applications and challenges. J. Appl. Phys. **104**, 071101.

Park, H. S. and Nguyen, T. D., 2013. Viscoelastic effects on electromechanical instabilities in dielectric elastomers. Soft Matter **9**, 1031-1042.

Park, H. S., Suo, Z., Zhou, J. and Klein, P. A., 2012. A dynamic finite element method for inhomogeneous deformation and electromechancial instability of dielectric elastomer transducers. Int. J. Solids Struct. **49**, 2187–2194.

Pei, Q., Rosenthal, M., Stanford, S., Prahlad, H. and Pelrine, R., 2004. Multiple-degrees-of-freedom electroelastomer roll actuators. Smart Mater. Struct. **13**, N86–92.

Pelrine, R. E., Kornbluh, R. D. and Joseph, J. P., 1998. Electrostriction of polymer dielectrics with compliant electrodes as a means of actuation. Sens. Actuators A **64**, 77-85.

Pelrine R, Kornbluh R, Joseph J, Heydt R, Pei Q and Chiba S 2000 High-field deformation of elastomeric dielectrics for actuators Materials Science and Engineering C 11 89-100

Pelrine, R., Kornbluh, R., Pei, Q. and Joseph, J., 2000. High-speed electrically actuated elastomers with greater than 100%. Science **287**, 836-839.

Pelrine, R., Kornbluh, R.D., Pei, Q., Stanford, S., Oh, S., Eckerle, J., Full, R., Rosenthal, M. and Meijer, K., 2002. Dielectric elastomer artificial muscle actuators: toward biomimetic motion. Proc. SPIE **4695**, 126-137.

Plante, J. and Dubowsky, S., 2006. Large-scale failure modes of dielectric elastomer actuators. Int. J. Solids Struct. **43**, 7727-7751.

Ross, C. T. F., 2011. Pressure Vessels: External Pressure Technology. Woodhead Publishing, Cambridge. pp 100-102.

Stoyanov, H., Kodod, G. and Gerhard, R., 2008. A co-axial dielectric elastomer actuator Advances in Science and Technology **61**, 81-84.

Suo, Z. and Zhu, J., 2009. Dielectric elastomers of interpenetrating networks. Appl. Phys. Lett. **95**, 232909.

Suo, Z., Zhao, X. and Greene, W. H., 2008. A nonlinear field theory of deformable dielectrics. J. Mech. Phys. Solids **56**, 467–486.

Teng, J. G. and Rotter, J. M., 2004. Buckling of Thin Metal Shells. Spon Press, London. pp 154-158.

Wissler, M. and Mazza, E., 2005 Modeling of a pre-strained circular actuator made of dielectric elastomers. Sens. Actuators A **120**, 184-192.

Zhao, X. and Suo, Z., 2007. Method to analyze electromechanical stability of dielectric elastomers. Appl. Phys. Lett. **91**, 061921.

Zhao, X. and Suo, Z., 2008a. Method to analyze programmable deformation of dielectric elastomer layers. Appl. Phys. Lett. **93**, 251902.

Zhao, X. and Suo, Z. 2008b. Electrostriction in elastic dielectrics undergoing large deformation. J. Appl. Phys. **104**, 123530.

Zhao, X. and Suo, Z., 2010. Theory of dielectric elastomers capable of giant deformation of actuation. Phys. Rev. Lett. **104**, 178302.

Zhao, X., Hong, W. and Suo, Z., 2007. Electromechanical hysteresis and coexistent states in dielectric elastomers. Phys. Rev. B **76**, 134113.

Zhou, J., Hong, W., Zhao, X., Zhang, Z. and Suo, Z., 2008. Propagation of instability in dielectric elastomers. Int. J. Solids Struct. **45**, 3739-3750.

Zhou, J., Jiang, L. and Khayat, R. E., 2013. Failure analysis of a dielectric elastomer plate actuator considering boundary constraints. J. Intell. Mater. Syst. Struct. **24**, 1667–1674.

Zhu, J., Cai, S. and Suo, Z., 2010a. Resonant behavior of a membrane of a dielectric elastomer. Int. J. Solids Struct. **47**, 3254-3262.

Zhu, J., Stoyanov, H., Kofod, G. and Suo, Z., 2010b. Large deformation and electromechanical instability of a dielectric elastomer tube actuator. J. Appl. Phys. **108**, 074113.

Chapter 5

5 Viscoelastic effects on frequency tuning of a dielectric elastomer membrane resonator

5.1 Introduction

Dielectric elastomers (DEs), as a category of electroactive polymers, which deform under electrical stimuli, have received significant attention due to their flexibility and capability of large deformation. Recent studies have shown that DEs hold promise for extensive potential applications, such as resonators, sensors, and actuators for robots, artificial muscles, energy harvesting systems, MEMS devices, programmable haptic surfaces, biomimetic applications, and adaptive optical elements (Huang *et al*., 2013; Carpi *et al*., 2008; Chiba *et al*., 2011; Kornbluh *et al*., 2002; Ahmadi *et al*., 2013; Lai *et al*., 2012; O'Halloran *et al*., 2008; Karsten *et al*., 2013; Anderson *et al*., 2010; Heydt *et al*., 2010).

The electromechanical coupling of DEs with quasi-static deformation has been widely studied in the literature (Pelrine *et al*., 2000; Zhu *et al*., 2010; Lu *et al*., 2012; Zhao *et al*., 2007; Zhao and Suo, 2008; Plante and Dubowsky, 2006; Wissler and Mazza, 2005; Koh *et al*., 2011; Zhao and Suo, 2010; Zhou *et al*., 2012; Huang and Suo, 2012; Zhao and Suo, 2007; Kollosche *et al*., 2012). However, relatively less work has been done on investigating their dynamic behavior. In recent years, DEs have been developed as resonators and oscillators which have been regarded as a potential alternative to the traditional silicon-based devices in MEMS (Zhang *et al*., 2005; Biggs and Hitchcock, 2010; O'Brien *et al*., 2012; Bonwit *et al.*, 2006). The merit of a DE-based resonator mainly lies in the fact that its natural frequency could be actively tuned by applying an electric voltage, while the natural frequency of a silicon-based resonator is basically fixed after fabrication (Dubois *et al*., 2008). This property not only enables DE-based resonators to have a wide range of resonant frequency but also provides a desirable solution to the challenges of traditional resonators, such as compensation for fabrication and environmental imperfection caused by aging, temperature, uniformity and contamination. Depending on specific applications, DE resonators and oscillators are designed in different shapes, such as micro-beam and membrane, on which most existing analyses for DE resonators and oscillators focus. For example, the dynamic response of axisymmetric DE membrane resonators was investigated by Mockensturn and Goulbourne (2006), Fox and Goulbourne (2008 and 2009) and Zhu *et al*. (2010) The nonlinear oscillation of spherical DE membrane resonators was studied by Zhu *et al*. (2010) and Yong *et al*. (2011) The active tuning of resonant frequency of a DE micro-beam resonator was explored by Feng *et al*. (2011) with the consideration of squeeze-film damping. Li *et al*. (2012) investigated the nonlinear oscillation of a tunable DE plate membrane resonator using a hyperelastic model.

Nevertheless, most existing studies ignored the intrinsic viscoelastic property of the DEs, which was proven to exert a significant effect on their dynamic and resonant performance (Plante and Dubowsky, 2007; Wissler and Mazza, 2005; Hong, 2011). Early studies on the viscoelasticity of DEs are limited to the linear theories and only congruous with relatively small deformation (Yang *et al*., 2005). However, most applications of DEs utilize their large-deformation capacity, for which the linear theories are not applicable. Later, a modified hyperelasticity theory was employed with an addition of the Maxwell stress to model the viscoelastic effect of the DE with finite-deformation (Plante and Dubowsky, 2007), which could only explain experimental phenomena for a particular category of cases, leaving many viscoelastic issues of DEs unsettled. Recently, based on the fully coupled field theory for elastic dielectrics by Suo *et al*. (2008) and the finite-deformation viscoelastic theory by Reese and Govindjee (1998) a model that accounts for both the finite inelastic deformation and the electromechanical coupling of the DEs was proposed by Hong (2011), which was claimed as a theoretical framework capable of adopting most finite-deformation constitutive models and evolution laws of viscoelastic solids. Park and Nguyen (2013) developed a finite formulation for the DEs involving both finite-deformation and viscoelastic effects. The dynamic performance of viscoelastic DEs under alternating mechanical load was investigated by Zhang *et al*. (2014). Wang *et al*. (2013) investigated the inhomogeneous viscoelastic deformation of an axisymmetric DE membrane subject to a combination of pressure and voltage. Based on the finite element model developed by Park and Nguyen (2013), the electrostatically driven creep and instabilities of the DEs were studied by Wang *et al*. (2014). These studies reported that the viscoelasticity had a strong effect on the dynamic performance of the DEs. Therefore, it is essential to examine the viscoelastic behavior of the DE-based resonators in order to provide a better design guideline for their potential applications.

To explain how the viscoelasticity of the DEs affects the dynamic behavior of the DE-based resonators, problem investigated by Li *et al*. (2012) for a membrane resonator with its configuration referred as the Reflex™ HIC Slide Actuator HIC-512 by Artificial Muscle Inc. (Biggs and Hitchcock, 2010) will be revisited. This configuration was designed as a haptic module for mobile handsets and expected to provide tactile effects when used as mobile devices. Without considering the viscoelasticity, the nonlinear oscillation and frequency tuning of such a DE membrane resonator were elucidated in the work of Li *et al*. (2012) based on the Gent model. By re-examining such a DE resonator, this work aims to illustrate the complex interplay of the material viscoelasticity, the pre-stretch influence and the failure modes of the DE-based resonators, thus providing a better understanding on their nonlinear and rate-dependent vibration behavior. It should be mentioned that some typical failure modes occur during the resonator oscillation, such as the electromechanical instability, the electrical breakdown and the loss of tension of the membrane. However, the electromechanical instability is not considered here since it is eliminated by the boundary constraints of the current resonator configuration (Zhou *et al*., 2013; Kollosche *et al*., 2012).

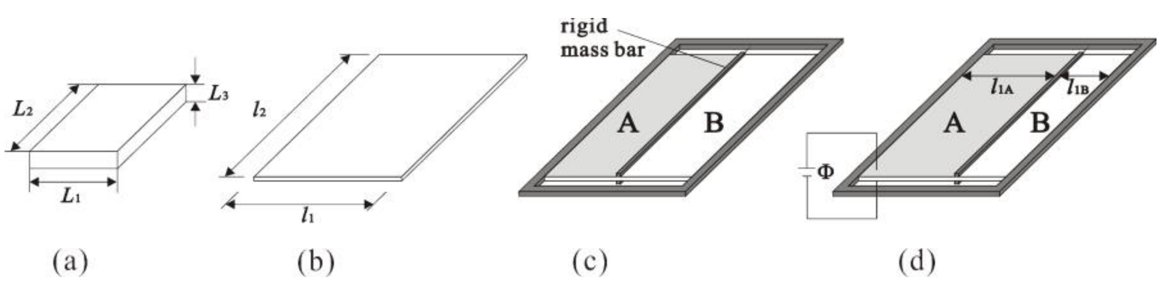

Figure 5.1 Configuration of a DE membrane resonator: (a) Undeformed state; (b) Pre-stretched state; (c) The pre-stretched membrane is bonded to a rigid frame with its two edges and sandwiched with two rigid mass bars; (d) Current state, in which membrane A is actuated by an electric voltage c.

5.2 Formulation of the problem

The schematics of a DE membrane resonator are displayed in Figure 5.1 (Biggs and Hitchcock, 2010; Li *et al.*, 2012). Figure 5.1(a) shows an undeformed state with dimensions L_1, L_2 and L_3 ($L_3 \ll L_1, L_2$). The undeformed membrane is then instantaneously pre-stretched to l_1 in 1-direction and l_2 in 2-direction with the corresponding pre-stretch ratios $a_{1\mathrm{p}} = l_1 / L_1$ and $a_{2\mathrm{p}} = l_2 / L_2$ (Figure 5.1(b)). The pre-stretched membrane is further bonded to a rigid frame with its two edges along 2-direction and clamped by two rigid bars with a mass of m, which separate the membrane into two parts: membrane A and B (Figure 5.1(c)). Part A is coated with compliant electrodes on its two surfaces as the active part, while part B acts as the passive part which deforms following the electrical stimulation of part A. The undeformed lengths of membrane A and B in 1-direction are denoted as $L_{1\mathrm{A}}$ and $L_{1\mathrm{B}}$ with the length ratio $k=L_{1\mathrm{A}}/L_{1\mathrm{B}}$. Then an electric voltage c is applied between the two electrodes of membrane A to force membrane A and B to deform to the current state with length $l_{1\mathrm{A}}$ and $l_{1\mathrm{B}}$ in 1-direction (Figure 5.1(d)). Constrained by the rigid frame and bars, membrane A is subject to the tensile forces $P_{1\mathrm{A}}$ and $P_{2\mathrm{A}}$ in 1- and 2-directions, respectively, as well as the applied voltage c, while membrane B is solely subject to the tensile forces $P_{1\mathrm{B}}$ and $P_{2\mathrm{B}}$ in the current state.

From the configuration of the resonator and its applied loads, the deformation gradients of the current state with respect to the underformed state for membrane A and B are described respectively as

$$\mathbf{F}_{\mathrm{A}} = \begin{pmatrix} a_{1\mathrm{A}} & 0 & 0 \\ 0 & a_{2\mathrm{A}} & 0 \\ 0 & 0 & a_{3\mathrm{A}} \end{pmatrix} \tag{5.1a}$$

and

$$\mathbf{F}_{\mathrm{B}} = \begin{pmatrix} a_{1\mathrm{B}} & 0 & 0 \\ 0 & a_{2\mathrm{B}} & 0 \\ 0 & 0 & a_{3\mathrm{B}} \end{pmatrix}. \tag{5.1b}$$

However, due to the intrinsic viscoelasticity of the DE, the deformation of the DE induced by the mechanical loads and the electric voltage may not be fully elastic, but consists of inelastic component as well. As originally suggested by Lee (1969), the total deformation gradients of a viscoelastic material can be multiplicatively decomposed into two parts: the elastic part and the inelastic part (Hong, 2011; Reese and Govindjee, 1998). This decomposition yields $\mathbf{F}_{\mathrm{A}} = \mathbf{F}_{\mathrm{A}}^{\mathrm{e}}\mathbf{F}_{\mathrm{A}}^{\mathrm{i}}$ and $\mathbf{F}_{\mathrm{B}} = \mathbf{F}_{\mathrm{B}}^{\mathrm{e}}\mathbf{F}_{\mathrm{B}}^{\mathrm{i}}$, where

$$\mathbf{F}_{\mathrm{A}}^{\mathrm{e}} = \begin{pmatrix} a_{1\mathrm{A}}^{\mathrm{e}} & 0 & 0 \\ 0 & a_{2\mathrm{A}}^{\mathrm{e}} & 0 \\ 0 & 0 & a_{3\mathrm{A}}^{\mathrm{e}} \end{pmatrix}, \tag{5.1c}$$

$$\mathbf{F}_{\mathrm{A}}^{\mathrm{i}} = \begin{pmatrix} a_{1\mathrm{A}}^{\mathrm{i}} & 0 & 0 \\ 0 & a_{2\mathrm{A}}^{\mathrm{i}} & 0 \\ 0 & 0 & a_{3\mathrm{A}}^{\mathrm{i}} \end{pmatrix}, \tag{5.1d}$$

$$\mathbf{F}_{\mathrm{B}}^{\mathrm{e}} = \begin{pmatrix} a_{1\mathrm{B}}^{\mathrm{e}} & 0 & 0 \\ 0 & a_{2\mathrm{B}}^{\mathrm{e}} & 0 \\ 0 & 0 & a_{3\mathrm{B}}^{\mathrm{e}} \end{pmatrix} \tag{5.1e}$$

and

$$\mathbf{F}_{\mathrm{B}}^{\mathrm{i}} = \begin{pmatrix} a_{1\mathrm{B}}^{\mathrm{i}} & 0 & 0 \\ 0 & a_{2\mathrm{B}}^{\mathrm{i}} & 0 \\ 0 & 0 & a_{3\mathrm{B}}^{\mathrm{i}} \end{pmatrix}. \tag{5.1f}$$

Here, the superscripts ‘e’ and ‘i’ represent the elastic part and the inelastic part, respectively. In this work, the DE is assumed to be incompressible for both the elastic and inelastic deformation as commonly treated in other studies (Zhu *et al*., 2010; Lu *et al*., 2012; Zhao *et al*., 2007; Plante and Dubowsky, 2006; Wissler and Mazza, 2005; Koh *et al*., 2011; Zhao and Suo, 2010; Zhou *et al*., 2013; Huang and Suo, 2012; Zhao and Suo, 2007; Hong, 2011), which gives the stretch ratios in 3-direction for both membranes A and B, i.e., $a_{3\mathrm{A}} = 1/a_{1\mathrm{A}}a_{2\mathrm{A}}$, $a^{e}_{3\mathrm{A}} = 1/a^{e}_{1\mathrm{A}}a^{e}_{2\mathrm{A}}$, $a^{i}_{3\mathrm{A}} = 1/a^{i}_{1\mathrm{A}}a^{i}_{2\mathrm{A}}$, $a_{3\mathrm{B}} = 1/a_{1\mathrm{B}}a_{2\mathrm{B}}$, $a^{e}_{3\mathrm{B}} = 1/a^{e}_{1\mathrm{B}}a^{e}_{2\mathrm{B}}$ and $a^{i}_{3\mathrm{B}} = 1/a^{i}_{1\mathrm{B}}a^{i}_{2\mathrm{B}}$.

Based on the finite-deformation viscoelastic theory proposed by Reese and Govindjee (1998), the Helmholtz free energy density W of the DE membrane in the current state can also be split into two parts: the non-equilibrium Helmholtz free energy density W^{NEQ} which is only related to the elastic deformation, and the equilibrium Helmholtz free energy density W^{EQ} which is determined by the total deformation and the electric displacement D of the DE membrane (Hong, 2011). Therefore, taking membrane A for example, we express the Helmholtz free energy density in the form

$$W_{\mathrm{A}} = W^{\mathrm{EQ}}_{\mathrm{A}}\left(a_{1\mathrm{A}}, a_{2\mathrm{A}}, D\right) + W^{\mathrm{NEQ}}_{\mathrm{A}}\left(a^{e}_{1\mathrm{A}}, a^{e}_{2\mathrm{A}}\right). \tag{5.2}$$

in which it is assumed that the electric field is always in equilibrium. This is due to the fact that the electric field reaches the equilibrium state much faster than the mechanical deformation. Following the work of Huang and Suo (2012) and Hong (2011) the equilibrium Helmholtz free energy density consists of the contributions from the total stretching and the polarization, i.e.,

$$W^{\mathrm{EQ}}_{\mathrm{A}} = W_{s}\left(a_{1\mathrm{A}}, a_{2\mathrm{A}}\right) + \frac{D^{2}}{2\pounds\pounds_{0}}, \tag{5.3}$$

where $W_{s}\left(a_{1\mathrm{A}}, a_{2\mathrm{A}}\right)$ is the strain energy density function of the DE and $D^{2}/2\pounds\pounds_{0}$ is the Helmholtz free energy related to the polarization. Also, the voltage-induced electric displacement D and the electric field E satisfy the material law $D = \pounds\pounds_{0}E$ (Zhao *et al*., 2007; Huang and Suo, 2012), where $\pounds_{0}$ is the permittivity of the vacuum and £ is the relative dielectric constant of the DE. Assuming uniform distribution of the electric field in the DE (Lu *et al*., 2012; Koh *et al*., 2011), E is further associated with the applied voltage c as $E = \text{c}\,\text{a}_{1A}\text{a}_{2A} / L_3$. Therefore, substitution of equation (5.3) into equation (5.2) gives

$$W_A = W_s\left(\text{a}_{1A}, \text{a}_{2A}\right) + W_A^{NEQ}\left(\text{a}_{1A} / \text{a}^{\text{i}}_{1A}, \text{a}_{2A} / \text{a}^{\text{i}}_{2A}\right) + \frac{\text{££}_0}{2}\left(\frac{\text{c}}{L_3}\right)^2 \text{a}^2_{1A}\text{a}^2_{2A} \,. \tag{5.4}$$

During the actuation process of the resonator, the variation of the kinetic variables δa_{1A} and δa_{1A} of membrane A results in the corresponding variation of the Helmholtz free energy, which equals to the work done by the tensile forces and the inertia force,

$$\begin{aligned} L_{1A}L_2L_3\left(\frac{\partial W_A}{\partial \text{a}_{1A}}\text{¢}\text{a}_{1A} + \frac{\partial W_A}{\partial \text{a}_{2A}}\text{¢}\text{a}_{2A}\right) &= P_{1A}L_{1A}\text{¢}\text{a}_{1A} + P_{2A}L_2\text{¢}\text{a}_{2A} - L_2L_3\frac{L^3_{1A}}{3}\text{°}\frac{d^2\text{a}_{1A}}{dt^2}\text{¢}\text{a}_{1A} \\ &\quad - L_{1A}L_2\frac{L_3^3}{3}\text{°}\frac{d^2\left(\text{a}^{-1}_{1A}\text{a}^{-1}_{2A}\right)}{dt^2}\text{¢}\left(\text{a}^{-1}_{1A}\text{a}^{-1}_{2A}\right) \end{aligned} \,, \tag{5.5}$$

where ° is the density of the DE membrane. Since the membrane is very thin $\left(L_3 \ll L_1\right)$, the last term in equation (5.5) could be omitted (Li *et al*., 2012). Neglecting the last term in equation (5.5) and substituting equation (5.4) into equation (5.5), we obtain

$$\begin{aligned} &\left\{L_A L_2 L_3\left[\frac{\partial W_s}{\partial \text{a}_{1A}} + \frac{\partial W_A^{NEQ}}{\partial \text{a}^{\text{e}}_{1A}}\left(\text{a}^{\text{i}}_{1A}\right)^{-1} + \text{££}_0\left(\frac{\text{c}}{L_3}\right)^2 \text{a}_{1A}\text{a}^2_{2A}\right] - P_{1A}L_{1A} + L_2L_3\frac{L_1^3}{3}\text{°}\frac{d^2\text{a}_{1A}}{dt^2}\right\}\text{¢}\text{a}_{1A} \\ &+\left\{L_A L_2 L_3\left[\frac{\partial W_s}{\partial \text{a}_{2A}} + \frac{\partial W_A^{NEQ}}{\partial \text{a}^{\text{e}}_{2A}}\left(\text{a}^{\text{i}}_{2A}\right)^{-1} + \text{££}_0\left(\frac{\text{c}}{L_3}\right)^2 \text{a}_{2A}\text{a}^2_{1A}\right] - P_{2A}L_2\right\}\text{¢}\text{a}_{2A} = 0 \end{aligned} \,. \tag{5.6}$$

Because δa_{1A} and δa_{2A} are any arbitrary small variation of the stretch ratios, equation (5.6) requires

$$L_A L_2 L_3\left[\frac{\partial W_s}{\partial \text{a}_{1A}} + \frac{\partial W_A^{NEQ}}{\partial \text{a}^{\text{e}}_{1A}}\left(\text{a}^{\text{i}}_{1A}\right)^{-1} + \text{££}_0\left(\frac{\text{c}}{L_3}\right)^2 \text{a}_{1A}\text{a}^2_{2A}\right] - P_{1A}L_{1A} + L_2L_3\frac{L_1^3}{3}\text{°}\frac{d^2\text{a}_{1A}}{dt^2} = 0 \,, \tag{5.7}$$

$$L_A L_2 L_3 \left[\frac{\partial W_s}{\partial \lambda_{2A}} + \frac{\partial W_A^{NEQ}}{\partial \lambda_{2A}^e} \left(\lambda_{2A}^i \right)^{-1} + \varepsilon\varepsilon_0 \left(\frac{\Phi}{L_3} \right)^2 \lambda_{2A} \lambda_{1A}^2 \right] - P_{2A} L_2 = 0 . \tag{5.8}$$

Once W_s and W_A^{NEQ} are specified, the deformation of the membrane A can be described by equations (5.7) and (5.8) in terms of the tensile forces and the electrical voltage. In this work, the Gent model (Gent, 1996) is adopted, in which the strain energy density function is related to the total stretching of the DE as

$$W_s = -\frac{G^{EQ} J_{lim}}{2} \ln\left(1 - \frac{\lambda_{1A}^2 + \lambda_{2A}^2 + \lambda_{1A}^{-2}\lambda_{2A}^{-2} - 3}{J_{lim}} \right), \tag{5.9}$$

where G^{EQ} is the equilibrium shear modulus as introduced in the work of Hong (2011) and J_{lim} is a dimensionless parameter determined by the stretching limit of the DE. As previously stated, the non-equilibrium Helmholtz free energy density is simply a function of the elastic deformation of the DE. Therefore, we can also assume the non-equilibrium Helmholtz energy density as a strain energy density function that is simply related to the elastic stretching of the DE following the finite-deformation viscoelasticity theory for dielectrics developed in the work of Hong (2011), i.e.,

$$W_A^{NEQ} = -\frac{G^{NEQ} J_{lim}}{2} \ln\left[1 - \frac{\left(\lambda_{1A}^e\right)^2 + \left(\lambda_{2A}^e\right)^2 + \left(\lambda_{1A}^e \lambda_{2A}^e\right)^{-2} - 3}{J_{lim}} \right], \tag{5.10}$$

where G^{NEQ} is the non-equilibrium shear modulus. Substituting equations (5.9) and (5.10) into equations (5.7) and (5.8) results in

$$\frac{P_{1A}}{G L_2 L_3} = \frac{\beta J_{lim}\left(\lambda_{1A} - \lambda_{1A}^{-3}\lambda_{2A}^{-2}\right)}{J_{lim} - \lambda_{1A}^2 - \lambda_{2A}^2 - \lambda_{1A}^{-2}\lambda_{2A}^{-2} + 3} + \frac{(1-\beta) J_{lim}\left[\lambda_{1A}\left(\lambda_{1A}^i\right)^{-2} - \lambda_{1A}^{-3}\lambda_{2A}^{-2}\left(\lambda_{1A}^i\right)^2\left(\lambda_{2A}^i\right)^2 \right]}{J_{lim} - \left(\frac{\lambda_{1A}}{\lambda_{1A}^i}\right)^2 - \left(\frac{\lambda_{2A}}{\lambda_{2A}^i}\right)^2 - \left(\frac{\lambda_{1A}\lambda_{2A}}{\lambda_{1A}^i\lambda_{2A}^i}\right)^{-2} + 3} + \frac{L_{1A}^2}{3G}\rho\frac{d^2\lambda_{1A}}{dt^2} - \frac{\varepsilon\varepsilon_0}{G}\left(\frac{\Phi}{L_3}\right)^2 \lambda_{1A}\lambda_{2A}^2, \tag{5.11}$$

$$\frac{P_{2A}}{G L_A L_3} = \frac{\beta J_{lim}\left(\lambda_{2A} - \lambda_{2A}^{-3}\lambda_{1A}^{-2}\right)}{J_{lim} - \lambda_{1A}^2 - \lambda_{2A}^2 - \lambda_{1A}^{-2}\lambda_{2A}^{-2} + 3} + \frac{(1-\beta) J_{lim}\left[\lambda_{2A}\left(\lambda_{2A}^i\right)^{-2} - \lambda_{2A}^{-3}\lambda_{1A}^{-2}\left(\lambda_{1A}^i\right)^2\left(\lambda_{2A}^i\right)^2 \right]}{J_{lim} - \left(\frac{\lambda_{1A}}{\lambda_{1A}^i}\right)^2 - \left(\frac{\lambda_{2A}}{\lambda_{2A}^i}\right)^2 - \left(\frac{\lambda_{1A}\lambda_{2A}}{\lambda_{1A}^i\lambda_{2A}^i}\right)^{-2} + 3} - \frac{\varepsilon\varepsilon_0}{G}\left(\frac{\Phi}{L_3}\right)^2 \lambda_{2A}\lambda_{1A}^2 . \tag{5.12}$$

where two material parameters $G = G^{EQ} + G^{NEQ}$ and are introduced. Physically, ¡ is an indicator of the fraction of the polymer networks that has time-independent deformation (Bergstrom and Boyce, 1998). ¡=1 represents an elastic material, while ¡=0 represents a viscous fluid for limiting cases.

Similarly, the deformation of the passive membrane B is described as

$$\frac{P_{1B}}{GL_2L_3} = \frac{\text{¡}\, J_{\lim}\left(a_{1B} - a_{1B}^{-3}a_{2B}^{-2}\right)}{J_{\lim} - a_{1B}^{2} - a_{2B}^{2} - a_{1B}^{-2}a_{2B}^{-2} + 3} + \frac{(1-\text{¡})\,J_{\lim}\left[a_{1B}\left(a^{i}_{1B}\right)^{-2} - a_{1B}^{-3}a_{2B}^{-2}\left(a^{i}_{1B}\right)^{2}\left(a^{i}_{2B}\right)^{2}\right]}{J_{\lim} - \left(\frac{a_{1B}}{a^{i}_{1B}}\right)^{2} - \left(\frac{a_{2B}}{a^{i}_{2B}}\right)^{2} - \left(\frac{a_{1B}a_{2B}}{a^{i}_{1B}a^{i}_{2B}}\right)^{-2} + 3} + \frac{L_{1B}^{2}}{3G} \circ \frac{d^{2}a_{1B}}{dt^{2}}, \quad (5.13)$$

$$\frac{P_{2B}}{GL_BL_3} = \frac{\text{¡}\, J_{\lim}\left(a_{2B} - a_{2B}^{-3}a_{1B}^{-2}\right)}{J_{\lim} - a_{1B}^{2} - a_{2B}^{2} - a_{1B}^{-2}a_{2B}^{-2} + 3} + \frac{(1-\text{¡})\,J_{\lim}\left[a_{2B}\left(a^{i}_{2B}\right)^{-2} - a_{2B}^{-3}a_{1B}^{-2}\left(a^{i}_{1B}\right)^{2}\left(a^{i}_{2B}\right)^{2}\right]}{J_{\lim} - \left(\frac{a_{1B}}{a^{i}_{1B}}\right)^{2} - \left(\frac{a_{2B}}{a^{i}_{2B}}\right)^{2} - \left(\frac{a_{1B}a_{2B}}{a^{i}_{1B}a^{i}_{2B}}\right)^{-2} + 3}. \quad (5.14)$$

Due to the actuation of the membrane A, the resonator is modeled with the oscillation of the rigid bars, for which the equation of motion is expressed as

$$\frac{P_{1A}}{GL_2L_3} - \frac{P_{1B}}{GL_2L_3} + \frac{mL_{1A}}{GL_2L_3}\frac{d^{2}a_{1A}}{dt^{2}} = 0, \quad (5.15)$$

in which *m* is the total mass of the two rigid bars.

In particular, when the resonator is static in the current state, the inertia terms in equations (5.11) and (5.13) vanish and the forces on the two the sides of the rigid bars are balanced off, i.e. $P_{1A} / GL_2L_3 = P_{1B} / GL_2L_3$, which yields

$$\begin{aligned} &\frac{\text{¡}\, J_{\lim}\left(a_{1A} - a_{1A}^{-3}a_{2A}^{-2}\right)}{J_{\lim} - a_{1A}^{2} - a_{2A}^{2} - a_{1A}^{-2}a_{2A}^{-2} + 3} + \frac{(1-\text{¡})\,J_{\lim}\left[a_{1A}\left(a^{i}_{1A}\right)^{-2} - a_{1A}^{-3}a_{2A}^{-2}\left(a^{i}_{1A}\right)^{2}\left(a^{i}_{2A}\right)^{2}\right]}{J_{\lim} - \left(\frac{a_{1A}}{a^{i}_{1A}}\right)^{2} - \left(\frac{a_{2A}}{a^{i}_{2A}}\right)^{2} - \left(\frac{a_{1A}a_{2A}}{a^{i}_{1A}a^{i}_{2A}}\right)^{-2} + 3} - \frac{\text{££}_0}{G}\left(\frac{\text{c}}{L_3}\right)^{2} a_{1A}a_{2A}^{2} \\ &= \frac{\text{¡}\, J_{\lim}\left(a_{1B} - a_{1B}^{-3}a_{2B}^{-2}\right)}{J_{\lim} - a_{1B}^{2} - a_{2B}^{2} - a_{1B}^{-2}a_{2B}^{-2} + 3} + \frac{(1-\text{¡})\,J_{\lim}\left[a_{1B}\left(a^{i}_{1B}\right)^{-2} - a_{1B}^{-3}a_{2B}^{-2}\left(a^{i}_{1B}\right)^{2}\left(a^{i}_{2B}\right)^{2}\right]}{J_{\lim} - \left(\frac{a_{1B}}{a^{i}_{1B}}\right)^{2} - \left(\frac{a_{2B}}{a^{i}_{2B}}\right)^{2} - \left(\frac{a_{1B}a_{2B}}{a^{i}_{1B}a^{i}_{2B}}\right)^{-2} + 3}. \end{aligned} \quad (5.16)$$

When ¡ =1, equations (5.11) to (5.16) model a purely elastic DE membrane, which recover the formulation in the work of Li *et al*. (2012). In the current study, L_2 is set to be much longer than L_1 so that we can assume $\lambda_{2A}=\lambda_{2B}=\lambda_{2p}$ until the loss of tension in 2-direction, i.e., when $P_{2A} \le 0$ or $P_{2B} \le 0$, wrinkling occurs in the membrane. In the undeformed state, the length ratio of membrane A to B in 1-direction is taken as $L_{1A}/L_{1B}=k$. In the current state, the stretch ratios for these two membrane parts satisfy $\lambda_{1B}=\lambda_{1p}+k(\lambda_{1p}-\lambda_{1A})$.

To obtain the inelastic stretch ratios in the equations above, the evolution equation proposed by Reese and Govindjee (1998) is adopted in the current work. Taking membrane A for example, the deformation gradient tensors defined above must satisfy the following equation

$$-\frac{1}{2}\mathbf{F}_{\mathrm{A}}\frac{d\left[(\mathbf{C}_{\mathrm{A}}^{\mathrm{i}})^{-1}\right]}{dt}\mathbf{F}_{\mathrm{A}}^{\mathrm{T}}\cdot\left(\mathbf{b}_{\mathrm{A}}^{\mathrm{e}}\right)^{-1}=\gamma^{-1}:\boldsymbol{\sigma}^{\mathrm{NEQ}}. \tag{5.17}$$

where $\mathbf{C}_{\mathrm{A}}^{\mathrm{i}}=\left(\mathbf{F}_{\mathrm{A}}^{\mathrm{i}}\right)^{\mathrm{T}}\mathbf{F}_{\mathrm{A}}^{\mathrm{i}}$, $\mathbf{b}_{\mathrm{A}}^{\mathrm{e}}=\mathbf{F}_{\mathrm{A}}^{\mathrm{e}}\left(\mathbf{F}_{\mathrm{A}}^{\mathrm{e}}\right)^{\mathrm{T}}$, $\boldsymbol{\sigma}^{\mathrm{NEQ}}=2\mathbf{F}_{\mathrm{A}}^{\mathrm{e}}\frac{\partial W^{\mathrm{NEQ}}}{\partial\mathbf{C}_{\mathrm{A}}^{\mathrm{e}}}\left(\mathbf{F}_{\mathrm{A}}^{\mathrm{e}}\right)^{\mathrm{T}}$, $\mathbf{C}_{\mathrm{A}}^{\mathrm{e}}=\left(\mathbf{F}_{\mathrm{A}}^{\mathrm{e}}\right)^{\mathrm{T}}\mathbf{F}_{\mathrm{A}}^{\mathrm{e}}$ and γ^{-1} is an isotropic rank-four mobility tensor. In addition, equation (5.17) requires γ^{-1} to be positive-definite. Due to the assumption that the DE membrane is incompressible, γ^{-1} takes the form (Reese and Govindjee, 1998)

$$\gamma^{-1}=\frac{1}{2\eta_v}\left(\mathbf{I}^4-\frac{1}{3}\mathbf{I}\otimes\mathbf{I}\right), \tag{5.18}$$

where η_v is the shear viscosity, $\mathbf{I}^4$ is the fourth order symmetric identity tensor and $\mathbf{I}$ is the second order identity tensor. Substituting $\mathbf{F}_{\mathrm{A}}$, $\mathbf{F}_{\mathrm{A}}^{\mathrm{i}}$, $\mathbf{F}_{\mathrm{A}}^{\mathrm{e}}$, W^{NEQ} and equation (5.18) into equation (5.17) results in the expression of the time-dependent inelastic stretch ratios of membrane A,

$$\frac{d\lambda^{v}_{1A}}{d\tau}=\frac{J_{\lim}\lambda^{v}_{1A}}{6\left[J_{\lim}-\left(\frac{\lambda_{1A}}{\lambda^{v}_{1A}}\right)^{2}-\left(\frac{\lambda_{2p}}{\lambda^{v}_{2A}}\right)^{2}-\left(\frac{\lambda_{1A}}{\lambda^{v}_{1A}}\right)^{-2}\left(\frac{\lambda_{2p}}{\lambda^{v}_{2A}}\right)^{-2}+3\right]}\left[2\left(\frac{\lambda_{1A}}{\lambda^{v}_{1A}}\right)^{2}-\left(\frac{\lambda_{2p}}{\lambda^{v}_{2A}}\right)^{2}-\left(\frac{\lambda_{1A}\lambda_{2p}}{\lambda^{v}_{1A}\lambda^{v}_{2A}}\right)^{-2}\right], \quad (5.19)$$

$$\frac{d\lambda^{v}_{2A}}{d\tau}=\frac{J_{\lim}\lambda^{v}_{2A}}{6\left[J_{\lim}-\left(\frac{\lambda_{1A}}{\lambda^{v}_{1A}}\right)^{2}-\left(\frac{\lambda_{2p}}{\lambda^{v}_{2A}}\right)^{2}-\left(\frac{\lambda_{1A}}{\lambda^{v}_{1A}}\right)^{-2}\left(\frac{\lambda_{2p}}{\lambda^{v}_{2A}}\right)^{-2}+3\right]}\left[2\left(\frac{\lambda_{2p}}{\lambda^{v}_{2A}}\right)^{2}-\left(\frac{\lambda_{1A}}{\lambda^{v}_{1A}}\right)^{2}-\left(\frac{\lambda_{1A}\lambda_{2p}}{\lambda^{v}_{1A}\lambda^{v}_{2A}}\right)^{-2}\right], \quad (5.20)$$

where $\tau = tG^{\mathrm{NEQ}}/\eta_v$ is the viscoelastic relaxation time. Similarly, we can obtain the time-dependent inelastic stretch ratios for membrane B as follows,

$$\frac{d\lambda^{v}_{1B}}{d\tau}=\frac{J_{\lim}\lambda^{v}_{1B}}{6\left[J_{\lim}-\left(\frac{\lambda_{1B}}{\lambda^{v}_{1B}}\right)^{2}-\left(\frac{\lambda_{2p}}{\lambda^{v}_{2B}}\right)^{2}-\left(\frac{\lambda_{1B}}{\lambda^{v}_{1B}}\right)^{-2}\left(\frac{\lambda_{2p}}{\lambda^{v}_{2B}}\right)^{-2}+3\right]}\left[2\left(\frac{\lambda_{1B}}{\lambda^{v}_{1B}}\right)^{2}-\left(\frac{\lambda_{2p}}{\lambda^{v}_{2B}}\right)^{2}-\left(\frac{\lambda_{1B}\lambda_{2p}}{\lambda^{v}_{1B}\lambda^{v}_{2B}}\right)^{-2}\right], \quad (5.21)$$

$$\frac{d\lambda^{v}_{2B}}{d\tau}=\frac{J_{\lim}\lambda^{v}_{2B}}{6\left[J_{\lim}-\left(\frac{\lambda_{1B}}{\lambda^{v}_{1B}}\right)^{2}-\left(\frac{\lambda_{2p}}{\lambda^{v}_{2B}}\right)^{2}-\left(\frac{\lambda_{1B}}{\lambda^{v}_{1B}}\right)^{-2}\left(\frac{\lambda_{2p}}{\lambda^{v}_{2B}}\right)^{-2}+3\right]}\left[2\left(\frac{\lambda_{2p}}{\lambda^{v}_{2B}}\right)^{2}-\left(\frac{\lambda_{1B}}{\lambda^{v}_{1B}}\right)^{2}-\left(\frac{\lambda_{1B}\lambda_{2p}}{\lambda^{v}_{1B}\lambda^{v}_{2B}}\right)^{-2}\right]. \quad (5.22)$$

It should be mentioned that the DE membranes have to be in tension during the operation of the resonator since membranes cannot sustain any compression. As a result, we have to ensure that $P_{1\mathrm{A}}/GL_2L_3 > 0$, $P_{2\mathrm{A}}/GL_AL_3 > 0$, $P_{1\mathrm{B}}/GL_2L_3 > 0$ and $P_{2B}/GL_BL_3 > 0$ during the actuation process. Furthermore, considerations should also be given to the electrical breakdown (EB) that may occur during the actuation of membrane A, which represents a failure mode when the voltage-induced electric field in membrane A exceeds its dielectric strength E_{EB}. At the EB point of membrane A, the corresponding applied voltage Φ_{B} is determined as (Koh *et al*., 2011; Zhou *et al*., 2013)

$$\frac{\Phi_{\mathrm{B}}}{L_3}\sqrt{\frac{\varepsilon\varepsilon_0}{G}} = d\,\lambda^{-1}_{1\mathrm{A}}\lambda^{-1}_{2\mathrm{A}}\,, \quad (5.23)$$

where $d = E_{\mathrm{EB}}\sqrt{££_0 / G}$ is a material parameter. Although the value of d may vary for different DE materials, we use a medium value d=5 (Koh *et al*., 2011) in this work for simulation purpose.

5.3 Natural frequency of the DE membrane resonator

Substituting equations (5.11) and (5.13) into the motion equation (5.15) of the rigid bars and noting that $a_{1\mathrm{B}}=a_{1\mathrm{p}}+k(a_{1\mathrm{p}}-a_{1\mathrm{A}})$ and $a_{2\mathrm{A}}=a_{2\mathrm{B}}=a_{2\mathrm{p}}$, we obtain

$$\frac{d^2 a_{1\mathrm{A}}}{dt^2} + g\left(a_{1\mathrm{A}}, a^{i}_{1\mathrm{A}}, a^{i}_{2\mathrm{A}}, a^{i}_{1\mathrm{B}}, a^{i}_{2\mathrm{B}}, \mathrm{c}\right) = 0, \tag{5.24}$$

where

$$g\left(a_{1\mathrm{A}}, a^{i}_{1\mathrm{A}}, a^{i}_{2\mathrm{A}}, a^{i}_{1\mathrm{B}}, a^{i}_{2\mathrm{B}}, \mathrm{c}\right) = \sim \left\{ \frac{i\, J_{\lim}\left(a_{1\mathrm{A}} - a^{-3}_{1\mathrm{A}} a^{-2}_{2\mathrm{A}}\right)}{J_{\lim} - a^2_{1\mathrm{A}} - a^2_{2\mathrm{A}} - a^{-2}_{1\mathrm{A}} a^{-2}_{2\mathrm{A}} + 3} + \frac{(1-i)\, J_{\lim}\left[a_{1\mathrm{A}}\left(a^{i}_{1\mathrm{A}}\right)^{-2} - a^{-3}_{1\mathrm{A}} a^{-2}_{2\mathrm{A}}\left(a^{i}_{1\mathrm{A}}\right)^2\left(a^{i}_{2\mathrm{A}}\right)^2\right]}{J_{\lim} - \left(\frac{a_{1\mathrm{A}}}{a^{i}_{1\mathrm{A}}}\right)^2 - \left(\frac{a_{2\mathrm{A}}}{a^{i}_{2\mathrm{A}}}\right)^2 - \left(\frac{a_{1\mathrm{A}} a_{2\mathrm{A}}}{a^{i}_{1\mathrm{A}} a^{i}_{2\mathrm{A}}}\right)^{-2} + 3} \right.$$

$$\left. - \frac{i\, J_{\lim}\left(a_{1\mathrm{B}} - a^{-3}_{1\mathrm{B}} a^{-2}_{2\mathrm{B}}\right)}{J_{\lim} - a^2_{1\mathrm{B}} - a^2_{2\mathrm{B}} - a^{-2}_{1\mathrm{B}} a^{-2}_{2\mathrm{B}} + 3} - \frac{(1-i)\, J_{\lim}\left[a_{1\mathrm{B}}\left(a^{i}_{1\mathrm{B}}\right)^{-2} - a^{-3}_{1\mathrm{B}} a^{-2}_{2\mathrm{B}}\left(a^{i}_{1\mathrm{B}}\right)^2\left(a^{i}_{2\mathrm{B}}\right)^2\right]}{J_{\lim} - \left(\frac{a_{1\mathrm{B}}}{a^{i}_{1\mathrm{B}}}\right)^2 - \left(\frac{a_{2\mathrm{B}}}{a^{i}_{2\mathrm{B}}}\right)^2 - \left(\frac{a_{1\mathrm{B}} a_{2\mathrm{B}}}{a^{i}_{1\mathrm{B}} a^{i}_{2\mathrm{B}}}\right)^{-2} + 3} - \frac{££_0}{G}\left(\frac{\mathrm{c}}{L_3}\right)^2 a_{1\mathrm{A}} a^2_{2\mathrm{A}} \right\}$$

and $\sim = 1/\left(\frac{L^2_{1A}}{3G}\circ + \frac{L^2_{1B}}{3G}k\circ + \frac{mL_{1A}}{GL_2L_3}\right)$.

The natural frequency of the DE resonator will be determined following the standard method employed in existing studies for nonlinear vibration analysis of both elastic and viscoelastic DE resonators (Zhu *et al*., 2010; Li *et al*., 2012; Zhang *et al*., 2014). At time t, with a small perturbation of amplitude $\Delta(t)$, the total stretch ratio of membrane A in 1-direction is expressed as

$$a_{1\mathrm{A}}(t) = a'_{1\mathrm{A}} + \Delta(t), \tag{5.25}$$

where a'_{1A} takes the value of a_{1A} in the kinetic equilibrium state before the perturbation is applied. Due to the instant and small amplitude of the perturbation, it is assumed that the inelastic stretch ratios remain the same as those in the kinetic equilibrium state. Meanwhile, function $g\left(a_{1A}, a^{i}_{1A}, a^{i}_{2A}, a^{i}_{1B}, a^{i}_{2B}, c\right)$ is expanded into Taylor series up to the first order as,

$$g\left(a_{1A}, a^{i}_{1A}, a^{i}_{2A}, a^{i}_{1B}, a^{i}_{2B}, c\right) = g\left(a'_{1A}, a^{i}_{1A}, a^{i}_{2A}, a^{i}_{1B}, a^{i}_{2B}, c\right) + \frac{\partial g\left(a'_{1A}, a^{i}_{1A}, a^{i}_{2A}, a^{i}_{1B}, a^{i}_{2B}, c\right)}{\partial a_{1A}} a \,. \tag{5.26}$$

Combining equations. (5.24), (5.25) and (5.26) leads to

$$\frac{d^2 a}{dt^2} + \frac{\partial g\left(a'_{1A}, a^{i}_{1A}, a^{i}_{2A}, a^{i}_{1B}, a^{i}_{2B}, c\right)}{\partial a_{1A}} a = 0\,. \tag{5.27}$$

From equation (5.27), the natural frequency of the DE membrane resonator is determined as

$$\mu_n^2 = \frac{\partial g\left(a'_{1A}, a^{i}_{1A}, a^{i}_{2A}, a^{i}_{1B}, a^{i}_{2B}, c\right)}{\partial a_{1A}}\,. \tag{5.28}$$

According to equation (5.28), the natural frequency of the resonator depends on the inelastic stretch ratios. Therefore, the natural frequency of the resonator is time-dependent and can be determined by solving the set of differential-algebraic equations (5.16), (5.19), (5.20), (5.21), (5.22) and (5.28) when the pre-stretches of the membrane and the applied voltage are prescribed.

5.3 Results and discussion

To illustrate the process of the actuation and natural frequency tuning of the DE membrane resonator, a scenario where the pre-stretching, framing and clamping of the DE membrane are instantaneously completed, and a voltage is then applied at a loading rate of $r = dc^*/d^2$ to membrane A is first considered, where $c^* = c\sqrt{££_0/G}/L_3$ is the dimensionless voltage. Figure 5.2 depicts the typical electromechanical response of the resonator (ª$_{1A}$ – c *) for different values of viscoelastic material parameter ¡ when the voltage loading rate, the length ratio and the pre-stretch ratios are set as r = 0.3, k = 1, ª$_{1p}$ = 2 and ª$_{2p}$ = 4, respectively. Under the same conditions, Figure 5.3 shows the dimensionless natural frequency $\Omega_n = \mu_n / \sqrt{\sim}$ of the resonator as a function of the dimensionless voltage c *. In Figures 5.2 and 5.3, the curves with 0 < ¡ < 1 correspond to a viscoelastic membrane while the curves with ¡ = 1 are for a purely elastic membrane. Also, in these two figures, the applied voltage is increased from 0 to the point where the resonator fails by the loss of tension, either in 1-direction (denoted by the dots) or in 2-direction (denoted by the triangles). It is observed that the electromechanical response in Figure 5.2 is monotonic while the frequency in Figure 5.3 is non-monotonic with respect to the voltage. During the actuation, the stiffness of the membrane keeps changing, which is indicated by the variation of the slope of the stretch-voltage curves in Figure 5.2. The variation of the membrane stiffness is due to both the stress relaxation and the electromechanical coupling for a viscoelastic DE, while such a variation is only in response to the electromechanical coupling for an elastic DE. For a small voltage, the stiffness of the membrane decreases, and the membrane approaches a softer state as the applied voltage increases. Correspondingly, the natural frequency of the membrane drops as shown in Figure 5.3. As the voltage continues to increase, the electromechanical response curve reaches an inflection point at which voltage level the natural frequency reaches a minimum. Beyond this voltage, the membrane becomes stiffer (as the slope decreases) and the natural frequency rises sharply until the membrane fails. Because the stress in a viscoelastic membrane is relaxed by the inelastic deformation during the actuation, a larger ª$_{1A}$ is induced by the same applied voltage compared to that of a purely elastic membrane. In other words, a viscoelastic membrane approaches different states of stiffness of the material faster than a purely elastic membrane during the actuation. It is also observed from these two figures that the critical electric voltage corresponding to the failure point of the resonator decreases as ¡ decreases (or the material viscosity increases). The trends for ¡= 1 in Figures 5.2 and 5.3 are in agreement with those in the work of Li *et al*. (2012). It is found that, if a higher electrical loading rate is used instead of r = 0.3, the electromechanical response for the DE membrane is essentially uninfluenced by the values of χ. This is illustrated in Figure 5.4 for r = 10. The reason behind this insensitivity to the material viscosity is due to the fact that the material has no sufficient time to relax before failure occurs. Comparing the results in Figures 5.2 and 5.4, it is also found that the electrical loading rate significantly influences the critical electric voltage corresponding to the failure of a viscoelastic resonator, i.e., with the increase of the loading rate, the critical voltage gets higher.

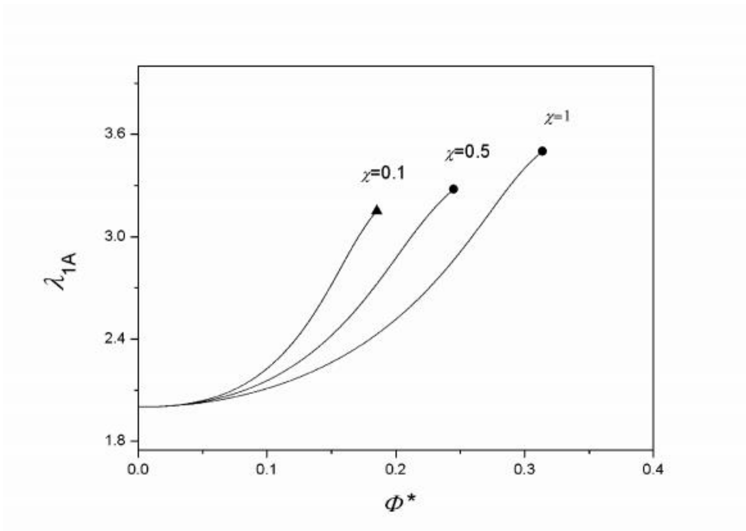

Figure 5.2 Electromechanical response $\left(\lambda_{1A} - \Phi^*\right)$ of a DE membrane resonator for k = 1, λ_{1p} = 2, λ_{2p} = 4 and different values of χ. The voltage is applied at the rate of r = 0.3.

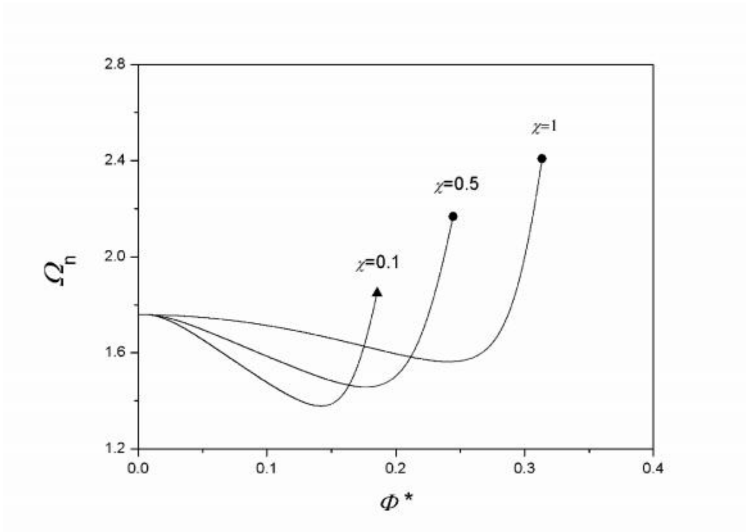

Figure 5.3 The dimensionless natural frequency of a DE membrane resonator for k = 1, λ_{1p} = 2, λ_{2p} = 4 and different values of χ. The voltage is applied at the rate of r = 0.3.

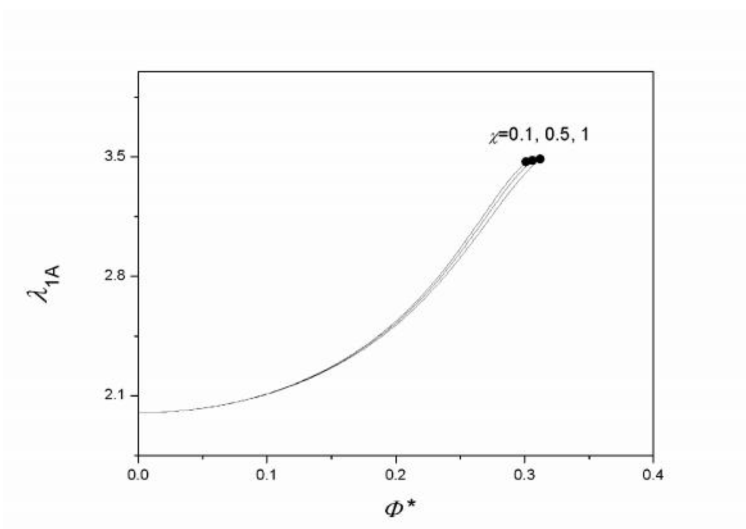

Figure 5.4 Electromechanical response $\left(\lambda_{1A} - \Phi^*\right)$ of a DE membrane resonator for k = 1, λ_{1p} = 2, λ_{2p} = 4 and different values of χ. The voltage is applied at the rate of r = 10.

In Figures 5.2, 5.3 and 5.4, the voltage was assumed to be applied immediately after the pre-stretching, framing and clamping processes of the membrane. However, in reality, the voltage may not be immediately applied. In this case, upon setting c = 0, equation (5.28) indicates that the natural frequency of the resonator becomes solely a function of the inelastic deformation induced by the pre-stretch. Figure 5.5 typically illustrates how the natural frequency t_n can change with time under pre-stretched conditions in the presence and absence of the electrical loading. The applied voltage is also shown for reference. Figure 5.5(a) depicts the variation of the natural frequency in the initial time interval, during which no voltage is applied. At ^{2}= 0, the DE membrane with ¡= 0.5 is assumed to be instantaneously pre-stretched ($^a{}_{1p}$ = 2 and $^a{}_{2p}$ = 4), framed and clamped with the rigid mass bars (the length ratio *k* = 1). From Figure 5.5(a), it is observed that the natural frequency first drops to a minimum, then rises, and eventually reaches a constant value. During this process, the stress in the membrane relaxes over time under a constant pre-stretch condition. When the deformation of the membrane becomes fully inelastic, the natural frequency becomes steady state. After a sufficient long time period for the membrane to fully relax, for example, at ^{2} =9, a voltage is applied to membrane A. Figure 5.5(b) shows the change of the natural frequency of the resonator during the actuation interval. As illustrated in this figure, the membrane deforms again and the natural frequency of the resonator varies with both the inelastic deformation and the applied voltage, according to equation (5.28). During the actuation, the voltage is increased at a very high rate (*r* = 10 for example), until the dimensionless voltage reaches a certain prescribed value c_p* (= 0.2 at ^{2} = 9.02 in this case). When the applied voltage is maintained at c_p*, as illustrated in Figure 5.5(c), the natural frequency of the resonator will continue to change until the membrane is in thermodynamic equilibrium again. It is observed that the natural frequency increases and eventually reaches a final steady value. This value is the actual natural frequency of the DE membrane resonator after the tuning process. Combining Figures 5.5(a), 5.5(b) and 5.5(c), Figure 5.5(d) summarizes the entire tuning process, and exhibits the variation of the natural frequency from the pre-stretching stage to the point where the frequency reaches a final steady value. From Figure 5.5(d), three main stages of the natural frequency tuning can be identified: the initial evolution stage under pre-stretched conditions in the absence of the electrical loading, the actuation stage, and the final evolution stage under a prescribed electrical loading. In addition, the difference between the final steady value and the initial steady value of the natural frequency in Figure 5.5(d) represents the frequency tuned by the applied voltage. The effect of the electrical loading rate on the frequency tuning process is also illustrated in Figure 5.5(d) by changing the loading rate to an extremely small value r = 0.05 and a moderate value r = 0.3. By comparing these results in Figure 5.5(d), it is found that the starting point of the final evolution is delayed when the electrical loading rate is decreased. A higher loading rate results in a higher instant frequency during the final evolution process. However, the final steady values of the natural frequency under the prescribed voltage are the same for different loading rates. It is thus concluded that the frequency tuned by the applied voltage is independent of the electrical loading rate. It should be mentioned that this prescribed voltage c_p^* = 0.2 for the frequency tuning is selected as a safe operation voltage without causing any failure of the DE membrane (i.e., the loss-of-tension or the electrical breakdown). Recalling the results in Figures 5.2 and 5.4 that the electrical loading rate influences the critical voltage, we expect that the safe operation voltage range and the tunable frequency range vary with the loading rate and will discuss this issue later.

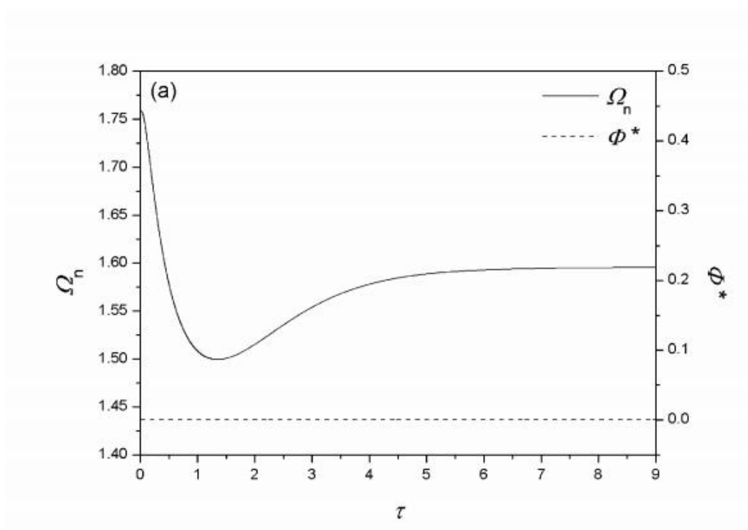

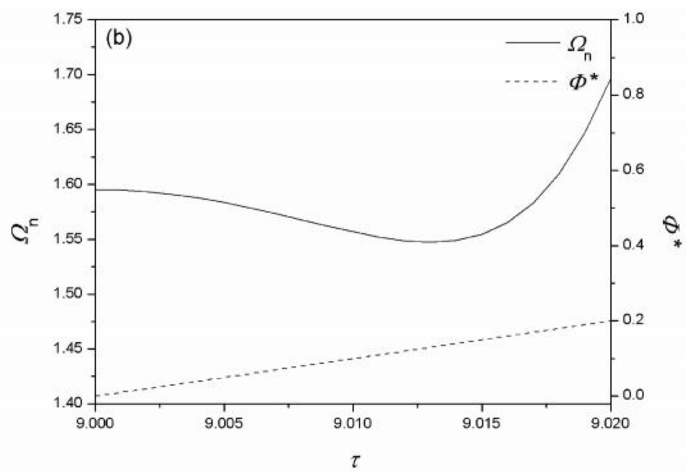
(b)
Ω_n
Φ*
1.75
1.70
1.65
1.60
1.55
1.50
1.45
1.40
1.0
0.8
0.6
0.4
0.2
0.0
9.000
9.005
9.010
9.015
9.020
τ

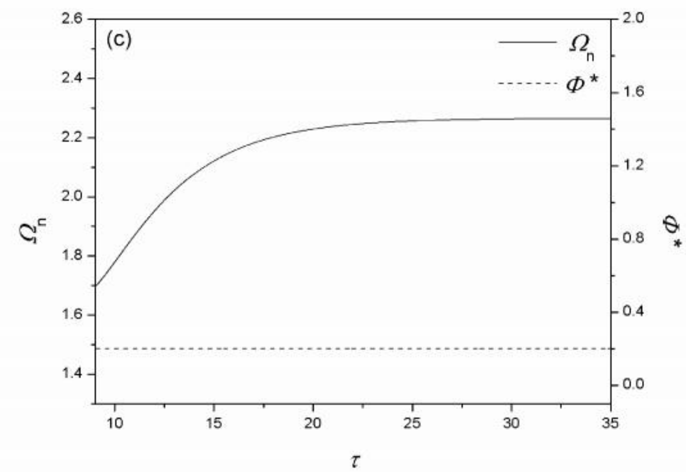
(c)
Ω_n
Φ*
2.6
2.4
2.2
2.0
1.8
1.6
1.4
2.0
1.6
1.2
0.8
0.4
0.0
10
15
20
25
30
35
τ

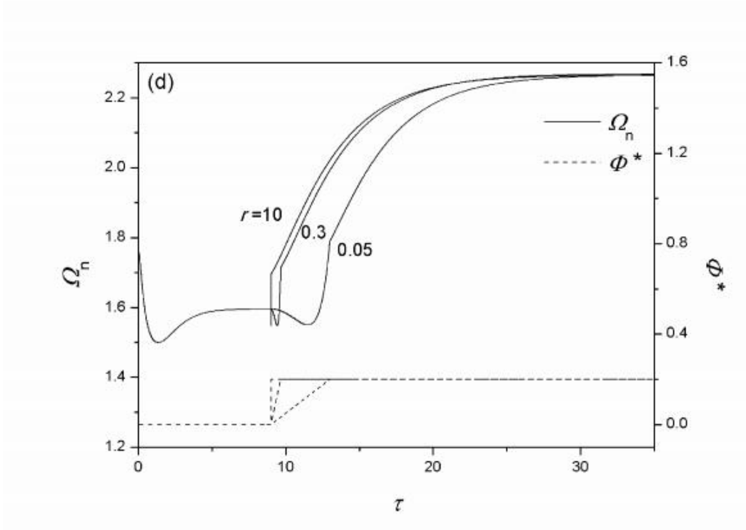

Figure 5.5 Variation of the natural frequency of a DE membrane resonator in the presence and absence of electrical loading, for k = 1, a_{1p} = 2 and a_{2p} = 4. The applied voltage is shown in dashed line. (a) The initial evolution stage under pre-stretched conditions in the absence of the electrical load; (b) The actuation stage (the voltage is applied at the rate of r = 10); (c) The evolution stage under a prescribed electrical loading; (d) Natural frequency tuning process (the voltage is applied at the rate of r = 10, r = 0.3 and r = 0.05).

The frequency tuning process in Figure 5.5(d) is governed by six parameters, namely the pre-stretch ratios a_{1p} and a_{2p}, the prescribed dimensionless voltage c_p*, the viscoelasticity parameter ¡, the length ratio k, and the electrical loading rate r. Here, we introduce the tuned frequency Δt_n as the difference between the final and initial steady values of the natural frequency (see Figure 5.5(d)), which is simply a function of c_p* when the values of r, ¡, k, a_{1p} and a_{2p} are fixed. Under different electrical loading rates (r = 10 and r = 0.05 for example), Figure 5.6(a) illustrates how Δt_n changes with c_p* for a viscoelastic DE resonator (¡ = 0.5) with k = 1, a_{1p} = 2, a_{2p} = 4. Figure 5.6(b) depicts the $\Delta t_n - c_p{}^*$ dependence for an elastic DE resonator (¡ = 1). The values of the voltage c_p* range from 0 to the point where the membrane fails either by the loss-of-tension in the membrane or by the electrical breakdown of the DE. Typically, the Δt_n curve displays a minimum. Therefore, one can denote the Δt_n -range between the minimum $\left(\Delta t_n^{\min}\right)$ and the failure level $\left(\Delta t_n^{f}\right)$ as the *tunable* frequency range of the DE membrane resonator. The voltage range between 0 and the failure point is defined as the *safe* operation voltage range. Consequently, once the material and geometrical parameters of the resonator are given, the tunable frequency range and the safe operation voltage range of the resonator can be determined. For applications of DE resonators with any configurations, these two ranges are very important since they can identify the range of electrical loading limit and the performance of a DE resonator. Figure 5.6(a) shows that the tunable frequency range corresponds entirely to the safe operation range since the minimum is essentially nonexistent. It is also found in Figure 5.6(a) that both the tunable frequency range and the safe operation voltage range of the viscoelastic DE resonator become larger if the electrical loading rate is higher. This is due to the fact that a higher electrical loading rate raises the critical electric voltage at which the material fails by the loss of tension as shown in Figures 5.2 and 5.4. A pronounced minimum is predicted for a purely elastic membrane (¡= 1), as shown in Figure 5.6(b). Moreover, the tunable frequency range for a viscoelastic DE membrane resonator (¡= 0.5) is larger than that of a purely elastic DE membrane resonator (¡= 1), while the safe operation voltage range of the viscoelastic resonator is much narrower. Therefore, neglecting the viscoelastic effect of the DE may lead to substantial errors in predicting the dynamic performance of the DE resonator.

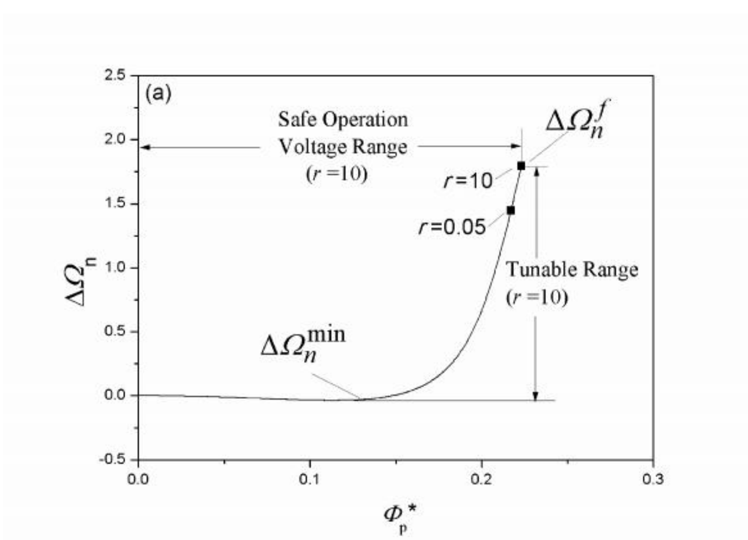

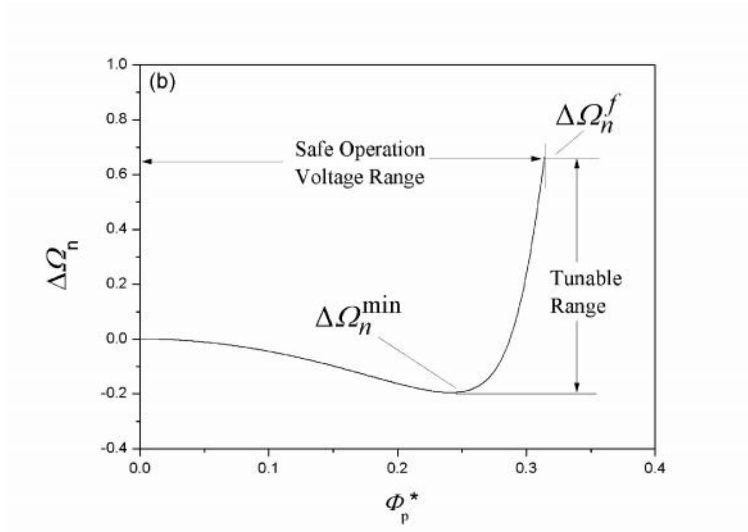

Figure 5.6 Tunable frequency range and safe operation voltage range of a DE membrane resonator with prescribed parameters k = 1, ª$_{1p}$ = 2, ª$_{2p}$ = 4. (a) ¡ = 0.5 (the voltage is applied at the rate of r = 10 and r = 0.05); (b) ¡ = 1 (the voltage is applied at the rate of r = 10).

In Figure 5.6, each tunable frequency range corresponds to a set of material and geometrical parameters (¡ l:k, ª$_{1p}$ and ª$_{2p}$) when the electrical loading rate is fixed. Therefore, when the material of the resonator is selected (¡ is fixed), a different set of geometrical parameters k, ª$_{1p}$ and ª$_{2p}$ will result in a different tunable frequency range. Figure 5.7 depicts the change of the tunable natural frequency range of a viscoelastic DE membrane resonator (¡ = 0.5) for different geometrical parameters when the loading rate is set as r = 0.3. In Figures 5.7(a) and 5.7(b), we set k = 2 and plot $\Delta t_n^{\min}$ and Δt_n^f for any combinations of ª$_{1p}$ and ª$_{2p}$, ranging from 1 to 4. As shown in Figures 5.7(a) and 5.7(b), by choosing certain pre-stretch ratios, the $\Delta t_n^{\min}$ can be lowered to -0.2, while Δt_n^f can be raised to about 3. To investigate how the aspect ratio k affects the tunable natural frequency range, we also plot $\Delta t_n^{\min}$ and Δt_n^f for k = 1 in Figures 5.7(c) and 5.7(d), and k = 0.3 in Figures 5.7(e) and 5.7(f), respectively. As indicated in Figure 5.7, the maximum value of the Δt_n^f increases as the value of k increases, while no obvious trend for $\Delta t_n^{\min}$ is observed as *k* varies. In addition, the tunable frequency range is dominated by the up-tuning side for any examined values of *k*. Therefore, such a DE membrane resonator appears to be more suitable for applications in which the frequency needs to be raised. We also examined the combined effects of the loading rate r with the pre-stretches a_{1p} and a_{2p} upon the frequency tuning. It was found that with the considered range of the pre-stretches in Figure. 5.7, a higher loading rate increases Δt_n^{f} but has no effect on $\Delta t_n^{\min}$. This is consistent with the conclusion drawn from Figure 6(a), while these results are not plotted here to keep the clarity of the 3D figures.

Finally, it should be mentioned that during the natural frequency tuning process, the deformation of the membrane can be inhomogeneous. For example, the pre-stretching, framing and clamping process may cause inhomogeneous deformation in the membrane, particularly in the vicinity of the clamps. Also, the voltage-induced deformation can be inhomogeneous if the voltage is applied at a relatively low rate. However, for illustration purpose, we assumed homogeneous deformation with the aim to provide a theoretical prediction of the trend of the natural frequency tuning process when considering material viscoelasticity.

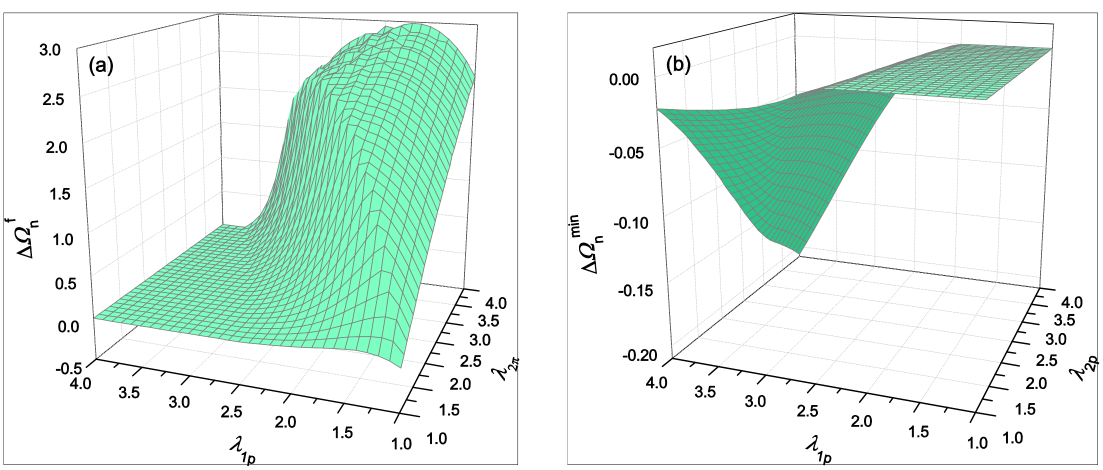

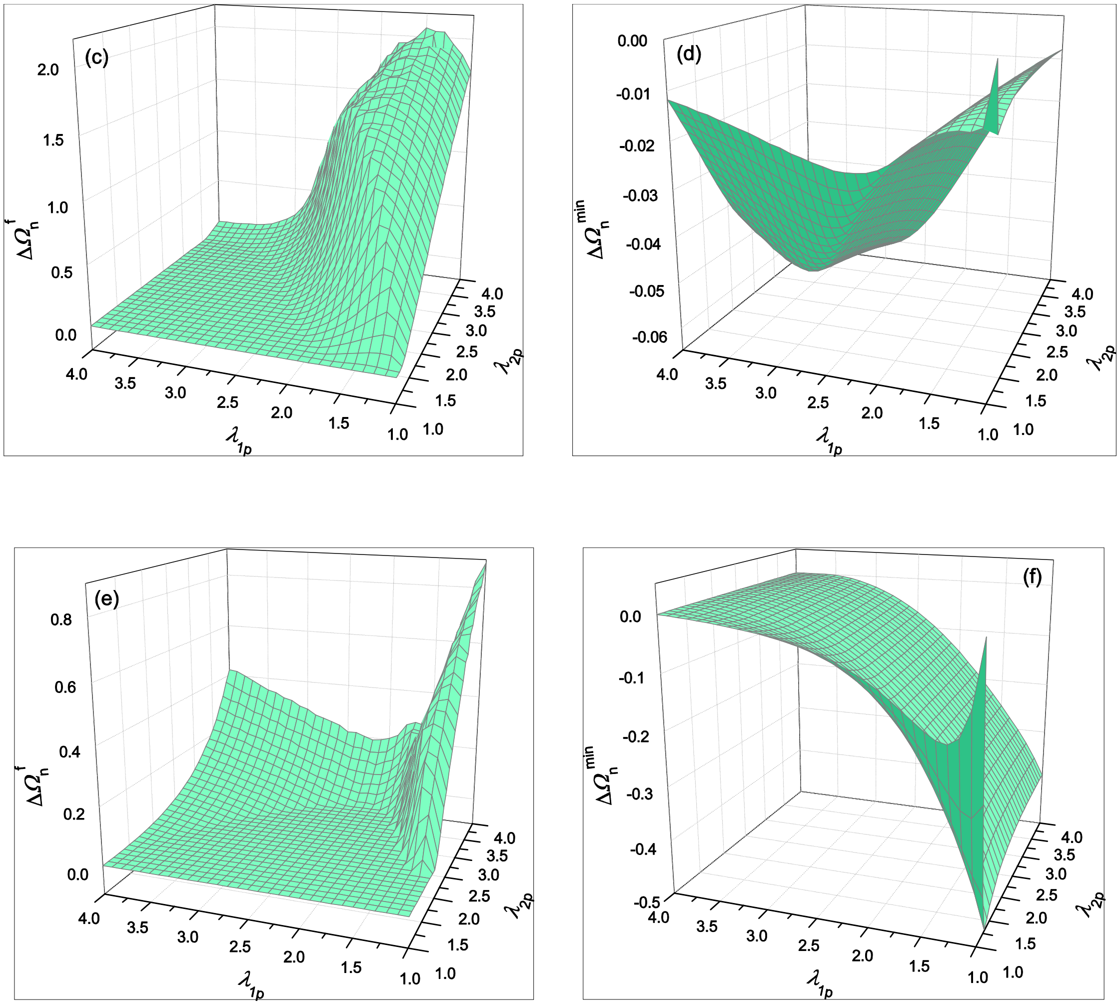

Figure 5.7 Δt_n^{min} and Δt_n^{f} of the tunable frequency range of a viscoelastic DE membrane resonator (¡ = 0.5) for various combinations of the pre-stretch ratios. In actuation interval, the voltage is applied at the rate of r = 0.3. (a) Δt_n^{f} for k= 2; (b) Δt_n^{min} for k = 2; (c) Δt_n^{f} for k = 1; (d) Δt_n^{min} for k = 1; (e) Δt_n^{f} for k = 0.3; (f) Δt_n^{min} for k = 0.3.

5.4 Conclusion

By studying the in-plane oscillation and the actuation of a DE membrane resonator, this work aims to provide a better understanding of the influence of material viscoelasticity on the natural frequency tuning of a DE resonator. Based on the finite-deformation viscoelasticity theory for dielectrics and the Gent model for hyperelasticity, a comparison of the natural frequency variation between a purely elastic DE membrane resonator and a viscoelastic DE membrane resonator is presented. The natural frequency of a purely elastic DE membrane resonator is solely changed by the applied voltage, while the natural frequency of a viscoelastic DE membrane resonator is time-dependent and affected by both the applied voltage and the inelastic deformation. With the consideration of possible failure modes such as the loss of tension and the electrical breakdown, the natural frequency tuning process, the tunable frequency range and the safe operation voltage range of a viscoelastic DE membrane resonator are investigated through parametric studies. Due to the material viscoelasticity, the electrical loading rate is found to influence both the tunable frequency range and the safe operation voltage range of the viscoelastic DE resonators. The study suggests that a viscoelastic DE resonator tends to be more suitable for applications in which the natural frequency needs to be tuned up, and provides the extent of the viscoelastic effect on the dynamic performance of DE-based resonators, as well as guidance for further experimental work.

References

Ahmadi, S., Gooyers, M., Soleimani, M. and Menon, C., 2013. Fabrication and electromechanical examination of a spherical dielectric elastomer actuator. Smart Mater. Struct. **22**, 115004.

Anderson, I. A., Hale, T., Gisby, T., Inamura, T., McKay, T., O'Brien, S. W. and Calius, E. P., 2010. A thin membrane artificial muscle rotary motor. Appl. Phys. A **98**, 75-83.

Bergstrom, J. S. and Boyce, M. C., 1998. Constitutive modeling of the large strain time-dependent behavior of elastomers. J. Mech. Phys. Solids **46**, 931–954.

Biggs, S. J. and Hitchcock, R. N., 2010. Artificial muscle actuators for haptic displays: system design to match the dynamics and tactile sensitivity of the human fingerpad. Proc. SPIE **7642**, 76420I.

Bonwit, N., Heim, J., Rosenthal, M., Dunchenon, C. and Beavers, A., 2006. Design of commercial applications of EPAM technology. Proc. SPIE **6168**, 616805.

Carpi, F., Rossi, D. D., Kornbluh, R., Pelrine, R. and Sommer-Larsen, P., 2008. Dielectric Elatomers as Electromechanical Transducers. Elsevier, Amsterdam.

Chiba, S., Waki, M., Kornbluh, R. and Pelrine, R., 2011. Current status and future prospects of power generators using dielectric elastomers. Smart Mater. Struct. **20**, 124006.

Dubois, P., Rosset, S., Niklaus, M., Dadras, M. and Shea, H., 2008. Voltage control of the resonance frequency of dielectric electroactive polymer (DEAP) membranes. J. Microelectromech. Syst. **17**, 1072-1081.

Feng, C., Jiang, L. and Lau, W. M., 2011. Dynamic characteristics of a dielectric elastomer-based microbeam resonator with small vibration amplitude. J. Micromech. Microeng. **21**, 095002.

Fox, J. W. and Goulbourne, N. C., 2008. On the dynamic electromechanical loading of dielectric elastomer membranes. J. Mech. Phys. Solids **56**, 2669-2686.

Fox, J. W. and Goulbourne, N. C., 2009. Electric field-induced surface transformations and experimental dynamic characteristics of dielectric elastomer membranes. J. Mech. Phys. Solids **57**, 1417-1436.

Gent, A. N., 1996. A new constitutive relation for rubber. Rubber Chem. Technol. **69**, 59-61.

Heydt, R., Kornbluh, R., Eckerle, J. and Pelrine, R., 2006. Sound radiation properties of dielectric elastomer electroactive polymer loadspeakers. Proc. SPIE **6168**, 61681M.

Hong, W., 2011. Modeling viscoelastic dielectrics. J. Mech. Phys. Solids **59**, 637-650.

Huang, J., Shian, S., Suo, Z. and Clarke, D. R., 2013. Dielectric elastomer generator with equi-biaxial mechanical loading for energy harvesting. Proc. SPIE **8687**, 86870Q.

Huang, R. and Suo, Z., 2011. Electromechanical phase transition in dielectric elastomers. Proc. R. Soc. A **468**, 1014–1040.

Karsten, R., Flittner, K., Haus, H. and Schlaak, H. F., 2013. Development of an active isolation mat based on dielectric elastomer stack actuators for mechanical vibration cancellation. Proc. SPIE **8687**, 86870Y.

Koh, S. J. A., Li, T., Zhou, J., Zhao, X., Hong, W., Zhu, J. and Suo, Z., 2011. Mechanisms of large actuation strain in dielectric elastomers. J. Polym. Sci. B **49**, 504–515.

Kollosche, M., Zhu, J., Suo, Z. and Kofod, G., 2012. Complex interplay of nonlinear processes in dielectric elastomers. Phys. Rev. E **85**, 051801.

Kornbluh, R., Pelrine, R., Pei, Q., Heydt, R., Stanford, S., Oh, S. and Eckerle, J., 2002. Electroelastomers: applications of dielectric elastomer transducers for actuation, generation and smart structures. Proc. SPIE **4698**, 254–270.

Lai, W., Bastawros, A. F. and Hong, W., 2012. Out-of-plane motion of a planar dielectric elastomer actuator with distributed stiffeners. Proc. SPIE **8340**, 834011.

Lee, E. H., 1969. Elastic-plastic deformation at finite strains. J. Appl. Mech. **36**, 1-6.

Li, T., Qu, S. and Yang, W., 2012. Electromechanical and dynamic analyses of tunable dielectric elastomer resonator. Int. J. Solids Struct. **49**, 3754-3761.

Lu, T., Huang, J., Jordi, C., Kovacs, G., Huang, R., Clarke, D. R. and Suo, Z., 2012. Dielectric elastomer actuators under equal-biaxial forces, uniaxial forces, and uniaxial constraint of stiff fibers. Soft Matter **8**, 6167–6173.

Mockensturm, E. M. and Goulbourne, N., 2006. Dynamic response of dielectric elastomers. Int. J. Nonlinear Mech. **41**, 388-395.

O'Brien, B. M., Rosset, S., Shea, H. R. and Anderson, I. A., 2012. Cutting the fat: artificial muscle oscillators for lighter, cheaper and slimmer devices. Proc. SPIE **8340**, 834008.

O'Halloran, A., O'Malley, F. and McHugh, P., 2008. A review on dielectric elastomer actuators, technology, applications and challenges. J. Appl. Phys. **104**, 071101.

Park, H. S. and Nguyen, T. D., 2013. Viscoelastic effects on electromechanical instabilities in dielectric elastomers. Soft Matter **9**, 1031-1042.

Pelrine, R., Kornbluh, R., Pei, Q. and Joseph, J., 2000. High-speed electrically actuated elastomers with greater than 100%. Science **287**, 836-839.

Plante, J. and Dubowsky, S., 2006. Large-scale failure modes of dielectric elastomer actuators. Int. J. Solids Struct. **43**, 7727-7751.

Plante, J. and Dubowsky, S., 2007. On the performance mechanisms of dielectric elastomer actuators. Sens. Actuators A **137**, 96-109.

Reese, S. and Govindjee, S., 1998. A theory of finite viscoelasticity and numerical aspects. Int. J. Solids Struct. **35**, 3455-3482.

Suo, Z., Zhao, X. and Greene, W. H., 2008. A nonlinear field theory of deformable dielectrics. J. Mech. Phys. Solids **56**, 467–486.

Wang, H., Lei, M. and Cai, S., 2013. Viscoelastic deformation of a dielectric elastomer membrane subject to electromechanical loads. J. Appl. Phys. **113**, 213508.

Wang, J., Nguyen, T. D. and Park, H. S., 2013. Electrostatically driven creep in viscoelastic dielectric elastomers. J. Appl. Mech. **81**, 051006.

Wissler, M. and Mazza, E., 2005 Modeling of a pre-strained circular actuator made of dielectric elastomers. Sens. Actuators A **120**, 184-192.

Wissler, M. and Mazza, E., 2005b Modeling and simulation of elastomer actuators. Smart Mater. Struct. **14**, 1396-1402.

Yang, E., Frecker, M. and Mockensturm, E., 2005. Viscoelastic model of dielectric elastomer membranes. Proc. SPIE **5759**, 82-93.

Yong, H., He, X. and Zhou, Y., 2011. Dynamics of a thick-walled dielectric elastomer spherical shell. Int. J. Eng. Sci. **49**, 792-800.

Zhang, G., Gaspar, J., Chu, V. and Conde, J. P., 2005. Electrostatically actuated polymer microresonators. Appl. Phys. Lett. **87**, 104104.

Zhang, J., Chen, H., Sheng, J., Liu, L., Wang, Y. and Jia, S., 2013. Dynamic performance of dissipative dielectric elastomers under alternating mechanical load. Appl. Phys. A **116**, 59-67.

Zhao, X. and Suo, Z. 2008. Electrostriction in elastic dielectrics undergoing large deformation. J. Appl. Phys. **104**, 123530.

Zhao, X. and Suo, Z., 2007. Method to analyze electromechanical stability of dielectric elastomers. Appl. Phys. Lett. **91**, 061921.

Zhao, X. and Suo, Z., 2010. Theory of dielectric elastomers capable of giant deformation of actuation. Phys. Rev. Lett. **104**, 178302.

Zhao, X., Hong, W. and Suo, Z., 2007. Electromechanical hysteresis and coexistent states in dielectric elastomers. Phys. Rev. B **76**, 134113.

Zhou, J., Jiang, L. and Khayat, R. E., 2013. Failure analysis of a dielectric elastomer plate actuator considering boundary constraints. J. Intell. Mater. Syst. Struct. **24**, 1667–1674.

Zhu, J., Cai, S. and Suo, Z., 2010a. Resonant behavior of a membrane of a dielectric elastomer. Int. J. Solids Struct. **47**, 3254-3262.

Zhu, J., Cai, S. and Suo, Z., 2010b. Nonlinear oscillation of a dielectric elastomer balloon. Polym. Int. **59**, 378-383.

Zhu, J., Stoyanov, H., Kofod, G. and Suo, Z., 2010c. Large deformation and electromechanical instability of a dielectric elastomer tube actuator. J. Appl. Phys. **108**, 074113.

Chapter 6

6 Investigation on the performance of a viscoelastic dielectric elastomer membrane generator

6.1 Introduction

Among most promising electroactive polymers for transduction technologies, dielectric elastomers (DEs) are attractive for energy harvesting applications due to their flexibility, large deformation capacity and high energy density compared with piezoelectric and electromagnetic materials. Recently, various prototypes of dielectric elastomer generators (DEGs) have been developed to harvest electricity by scavenging mechanical energy from diverse sources including ocean waves (Kornbluh *et al*., 2012; Jean *et al*., 2012; Chiba *et al*., 2011), wind and human movements (Kornbluh *et al*., 2012; Carpi *et al*., 2008; Jean-Mistral *et al*., 2008; Jean-Mistral *et al*., 2012). As an inverse operation mode of dielectric elastomer actuators (Pelrine *et al*., 2000), DEGs convert mechanical energy into electrical energy by transferring charges from low to high voltage in harvesting circuits when the DE is stretched and shrinks back during electromechanical cycles (Pelrine *et al*., 2001).

The energy harvesting performance of DEGs with different designs and materials has been reported in quite a few experimental works since the DEG was first proposed by Pelrine *et al.* (2001). From those studies (Kornbluh *et al*., 2012; Pelrine *et al*., 2001; McKay *et al*., 2010a; McKay *et al*., 2010b; McKay *et al*., 2011; Huang *et al*., 2013; Kaltseis *et al*., 2011), it was found that the both the energy density achieved per cycle and the average efficiency of the DEGs are quite scattered. For example, the very first prototype of a plate DEG proposed by Pelrine *et al*. (2001) has an energy density up to 400 J/kg. The DEGs with integrated self-priming circuits can provide electrical energy with density from 2.8J/kg to 12.6 J/kg (McKay *et al*., 2010a; McKay *et al*., 2010b; McKay *et al*., 2011). An energy density of 300 J/kg has been achieved from the DEG embedded in shoes, which can harvest mechanical energy from human body movement

(Kornbluh *et al*., 2012). The sea trial of an ocean wave DEG developed by Kornbluh *et al*. (2012) shows an energy density of about 50 J/kg. By applying equi-biaxial loading, Huang *et al.* (2013) have experimentally demonstrated that an energy density of 560 J/kg can be achieved from a membrane DEG. They also found that an average efficiency of the first nine cycles reaches up to 27%, which was significantly improved from 7.5% of a balloon-like DEG (Kaltseis *et al*., 2011) using the same dielectric elastomer. Recently, by optimizing the electromechanical harvesting cycle, Shian *et al*. (2014) have achieved an even higher energy density of 780J/kg with a similar efficiency as that in the work of Huang *et al*. (2013) Although some of these values of energy density are already at least one order of magnitude higher than those of piezoelectric and electromagnetic generators, they are still far less than the theoretical maximum energy density values predicted in the literature (1700 J/kg) (Koh *et al*., 2011).

As argued in earlier studies on DEGs, the performance of the DEGs is not only limited by various failure modes such as electrical breakdown (EB) and loss of tension, but is also strongly affected by the material properties and other mechanisms such as material extensibility, material viscoelasticity, current leakage and loading configurations (Huang *et al*., 2013; Koh *et al*., 2009; Koh *et al*., 2011; Hoffstadt *et al*., 2013). The energy harvesting mechanism of a DEG, in fact, lies in the cyclic change of the capacitance, which is realized by stretching the DE and allowing it to recover. The larger the deformation of the DE is, the more the capacitance changes and thus higher energy density is achieved. Moreover, the capacitance change could also be maximized by changing loading configurations as demonstrated by Huang *et al*. (2013). Particularly, it was reported by Huang *et al*. (2013) that the efficiency of the DEG is mainly limited by the viscous loss if the DEG operates in the safe range where electrical breakdown does not occur. However, most existing modeling works on the DEGs ignore the intrinsic viscoelasticity of the elastomers and only consider their hyperelastic properties (Koh *et al*., 2009; Koh *et al*., 2011; Hoffstadt *et al*., 2013), which leaves many issues unsettled and may need further investigation. During the energy harvesting cycles of the DEGs, it is expected that the material viscoelasticity results in the change of the performance with the stretching and shrinking rates of the elastomer, as well as the stretch ratios. Since the DEGs may undergo large deformation in the energy harvesting process, it is essential to examine their finite-deformation viscoelastic behavior. Among the viscoelastic models, a particular one proposed by Hong (2011) based on the fully coupled field theory for dielectrics by Suo *et al*. (2011) and the finite-deformation viscoelastic theory by Reese and Govindjee (1998), accounts for both the large inelastic deformation and the electromechanical coupling of the dielectric elastomers. Such a model is expected to make reliable prediction on the dynamic performance of the DEGs under general loads and constraints. Recently, based on these theories, Foo *et al*. (2012) investigated the dissipative process of the DEGs; Li *et al*. (2012) examined the viscoelastic deformation of the DEGs considering inhomogeneous deformation; Park and Nguyen (2013) developed finite element formulation for the DEs and Wang *et al*. (2014) further investigated the electrostatically driven creep and instabilities of the DEs.

Given the significant discrepancy of the energy density between the experimental results and the theoretical prediction, the energy harvesting performance of the DEGs may have large room for improvement with optimal design of the harvesting system. Adopting Hong's viscoelastic model (Hong 2011), this work presents a parametric study on the energy harvesting performance of a membrane DEG and aims to provide increased understanding on the effects of the material viscoelasticity, the failure modes, the bias voltage in the harvesting circuit, and the mechanical loading configurations on the energy harvesting process, thus leading to better guidance on the optimal design of the DEGs. We also propose a hypothesis on the fatigue life of the dielectric elastomers under cyclic loading condition to interpret the discrepancy between the theoretical modeling and the experimental observation.

6.2 Model and formulation of viscoelastic DEGs

The schematics of a typical DE membrane generator are shown in Figure 6.1. Figure 6.1(a) illustrates a typical energy harvesting circuit of the generator (Huang *et al*., 2013), which mainly consists of three parts: the power supply battery, the large harvesting capacitor and the DE membrane coated with compliant electrodes on its top and bottom surfaces (i.e., a DE capacitor). In an energy harvesting cycle or an electromechanical cycle, the DE membrane is continuously deformed, causing the change in its capacitance, and thus delivering charges from the low-voltage (Φ_L) power supply to the high-voltage (Φ_H) harvesting capacitor. The two diodes work as switches to only allow charge flow in one direction. In this case, charges (Q_{in}) flow from the power supply to the DE membrane when $\Phi < \Phi_L$, and charges (Q_{out}) flow from the membrane to the harvesting capacitor when $\Phi > \Phi_H$, the latter being the charges harvested by the generator. In other words, the diodes connect and disconnect these three parts automatically, depending on the level of voltage Φ applied across the DE membrane. Figure 6.1(b) displays the DE membrane in the undeformed state with length L, thickness H and a mass of m. When subjected to a voltage Φ between the electrodes and stretching in 1- and 2-directions, the membrane deforms to the state with thickness h, length l_1 and l_2 (Figure 6.1(c)). Due to the voltage across the DE membrane, charges accumulate on the two electrodes, i.e., $\pm Q = C\Phi$, where C is the capacitance of the DE membrane and it varies during the energy harvesting cycle.

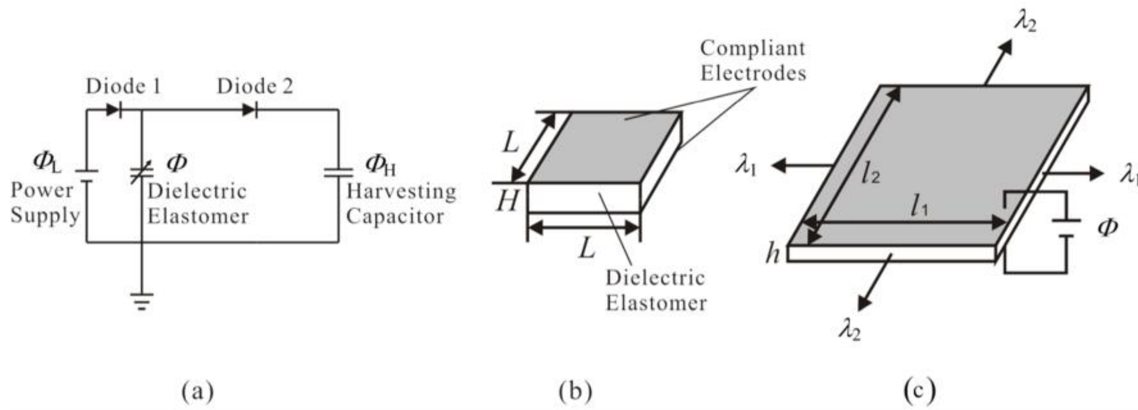

Figure 6.1 Schematics of a dielectric elastomer generator (DEG): (a) energy harvesting circuit diagram; (b) undeformed state of the dielectric elastomer membrane; (c) deformed state of the dielectric elastomer membrane when subject to voltage Φ and in-plane stretching.

During the energy harvesting cycles, the homogeneous deformation of the membrane is denoted by the stretch ratios, which are defined as $\lambda_1=l_1/L$, $\lambda_2=l_2/L$ and $\lambda_3=h/H$. The deformation gradient is thus expressed as

$$\mathbf{F}=\begin{pmatrix}\lambda_1 & 0 & 0\\ 0 & \lambda_2 & 0\\ 0 & 0 & \lambda_3\end{pmatrix}.$$

Following the work of Reese and Govindjee (1998) and Hong (2011), the stretch ratios of the deformed DE membrane are further multiplicatively decomposed into an elastic part and an inelastic part, i.e., $\mathbf{F}=\mathbf{F}^{\mathrm{e}}\mathbf{F}^{\mathrm{i}}$, with $\mathbf{F}^{e}=\begin{pmatrix}\lambda_1^{\mathrm{e}} & 0 & 0\\ 0 & \lambda_2^{\mathrm{e}} & 0\\ 0 & 0 & \lambda_3^{\mathrm{e}}\end{pmatrix}$ and $\mathbf{F}^{i}=\begin{pmatrix}\lambda_1^{\mathrm{i}} & 0 & 0\\ 0 & \lambda_2^{\mathrm{i}} & 0\\ 0 & 0 & \lambda_3^{\mathrm{i}}\end{pmatrix}$, where the superscripts "e" and "i" represent elastic and inelastic, respectively.

As commonly adopted in the literature (Koh *et al*., 2011; Hong 2011; Foo *et al*., 2012; Zhao and Suo, 2007; Zhou *et al*., 2014), the dielectric elastomer is assumed to be incompressible for both the elastic and inelastic deformations. Thus, the stretch ratios satisfy $\lambda_3=1/\lambda_1\lambda_2$, $\lambda_3^{\mathrm{e}}=1/\lambda_1^{\mathrm{e}}\lambda_2^{\mathrm{e}}$ and $\lambda_3^{\mathrm{i}}=1/\lambda_1^{\mathrm{i}}\lambda_2^{\mathrm{i}}$. Furthermore, the Helmholtz free energy density W of the membrane is split into two parts: A non-equilibrium part W^{NEQ} related only to the elastic deformation, and an equilibrium part W^{EQ} in response to both the total deformation and the applied electric voltage Φ, i.e.,

$$W=W^{\mathrm{EQ}}\left(\lambda_1,\lambda_2,\Phi\right)+W^{\mathrm{NEQ}}\left(\lambda_1^{\mathrm{e}},\lambda_2^{\mathrm{e}}\right). \tag{6.1}$$

It should be mentioned that the electric field is assumed to be in equilibrium as the electric field always reaches the equilibrium state much faster than the mechanical deformation (Hong, 2011). According to the work by Huang and Suo (2012), the equilibrium Helmholtz free energy density W^{EQ} takes the form

$$W^{\mathrm{EQ}}=W_{s}\left(\lambda_1,\lambda_2\right)+\frac{\varepsilon\varepsilon_0}{2}\left(\frac{\Phi}{H}\right)^2\lambda_1^2\lambda_2^2, \tag{6.2}$$

where $W_s(\lambda_1, \lambda_2)$ is the strain energy density function of the elastomer and the second term is the Helmholtz free energy associated with the polarization; ε_0 is the permittivity of the vacuum and ε is the relative dielectric constant of the DE. Accounting for the finite deformation of the DE, the Gent model (Gent 1996) is adopted in the current work with the strain energy density given as

$$W_s = -\frac{G^{\mathrm{EQ}} J_{\mathrm{lim}}^{\mathrm{EQ}}}{2} \ln\left(1 - \frac{\lambda_1^2 + \lambda_2^2 + \lambda_1^{-2}\lambda_2^{-2} - 3}{J_{\mathrm{lim}}^{\mathrm{EQ}}}\right), \tag{6.3}$$

where G^{EQ} is the equilibrium shear modulus and $J_{\mathrm{lim}}^{\mathrm{EQ}}$ is a dimensionless parameter determined by the extensibility of the elastomer. Since the non-equilibrium Helmholtz free energy is only determined by the elastic deformation of the elastomer, following Hong (2011), it is assumed that the non-equilibrium Helmholtz energy density also takes the same form of the strain energy density function, i.e.,

$$W^{\mathrm{NEQ}} = -\frac{G^{\mathrm{NEQ}} J_{\mathrm{lim}}^{\mathrm{NEQ}}}{2} \ln\left[1 - \frac{\left(\lambda_1^e\right)^2 + \left(\lambda_2^e\right)^2 + \left(\lambda_1^e \lambda_2^e\right)^{-2} - 3}{J_{\mathrm{lim}}^{\mathrm{NEQ}}}\right], \tag{6.4}$$

where G^{NEQ} is the non-equilibrium shear modulus and $J_{\mathrm{lim}}^{\mathrm{NEQ}}$ is a constant related to the limiting stretch of the elastic part.

Due to the stretching of the elastomer membrane, tensile forces in 1- and 2- direction (P_1 and P_2) are induced during the electromechanical cycles of the DEG. Moreover, the variation of the total stretch ratios $\delta\lambda_1$ and $\delta\lambda_2$ of the elastomer results in the change of the total Helmholtz free energy, which is equal to the work done by the tensile forces, i.e.,

$$L^2 H \left(\frac{\partial W}{\partial \lambda_1}\delta\lambda_1 + \frac{\partial W}{\partial \lambda_2}\delta\lambda_2\right) = P_1 L \delta\lambda_1 + P_2 L \delta\lambda_2 . \tag{6.5}$$

Inserting equations (6.1), (6.2), (6.3) and (6.4) into equation (6.5) and considering the fact that δa_1 and δa_2 are any arbitrary small variations, we obtain

$$\frac{P_1}{GLH} = \frac{\text{¡}\, J_{\lim}^{\mathrm{EQ}}\left(\text{a}_1 - \text{a}_1^{-3}\text{a}_2^{-2}\right)}{J_{\lim}^{\mathrm{EQ}} - \text{a}_1^2 - \text{a}_2^2 - \text{a}_1^{-2}\text{a}_2^{-2} + 3} + \frac{(1-\text{¡})\, J_{\lim}^{\mathrm{NEQ}}\left[\text{a}_1\left(\text{a}_1^{\mathrm{i}}\right)^{-2} - \text{a}_1^{-3}\text{a}_2^{-2}\left(\text{a}_1^{\mathrm{i}}\right)^2\left(\text{a}_2^{\mathrm{i}}\right)^2\right]}{J_{\lim}^{\mathrm{NEQ}} - \left(\frac{\text{a}_1}{\text{a}_1^{\mathrm{i}}}\right)^2 - \left(\frac{\text{a}_2}{\text{a}_2^{\mathrm{i}}}\right)^2 - \left(\frac{\text{a}_1\text{a}_2}{\text{a}_1^{\mathrm{i}}\text{a}_2^{\mathrm{i}}}\right)^{-2} + 3} - \frac{\text{££}_0}{G}\left(\frac{\Phi}{H}\right)^2 \text{a}_1\text{a}_2^2, \tag{6.6}$$

$$\frac{P_2}{GLH} = \frac{\text{¡}\, J_{\lim}^{\mathrm{EQ}}\left(\text{a}_2 - \text{a}_2^{-3}\text{a}_1^{-2}\right)}{J_{\lim}^{\mathrm{EQ}} - \text{a}_1^2 - \text{a}_2^2 - \text{a}_1^{-2}\text{a}_2^{-2} + 3} + \frac{(1-\text{¡})\, J_{\lim}^{\mathrm{NEQ}}\left[\text{a}_2\left(\text{a}_2^{\mathrm{i}}\right)^{-2} - \text{a}_2^{-3}\text{a}_1^{-2}\left(\text{a}_1^{\mathrm{i}}\right)^2\left(\text{a}_2^{\mathrm{i}}\right)^2\right]}{J_{\lim}^{\mathrm{NEQ}} - \left(\frac{\text{a}_1}{\text{a}_1^{\mathrm{i}}}\right)^2 - \left(\frac{\text{a}_2}{\text{a}_2^{\mathrm{i}}}\right)^2 - \left(\frac{\text{a}_1\text{a}_2}{\text{a}_1^{\mathrm{i}}\text{a}_2^{\mathrm{i}}}\right)^{-2} + 3} - \frac{\text{££}_0}{G}\left(\frac{\Phi}{H}\right)^2 \text{a}_2\text{a}_1^2. \tag{6.7}$$

where $G = G^{\mathrm{EQ}} + G^{\mathrm{NEQ}}$ is the instantaneous shear modulus, and the material parameter $\text{¡} = G^{\mathrm{EQ}}/G$ indicates the fraction of the polymer networks that have time-independent behavior (Bergstrom and Boyce, 1998). Correspondingly, the material is a viscous fluid when $\text{¡}=0$, while $\text{¡}=1$ represents a purely elastic material.

The inelastic stretch ratios a_1^i and a_2^i in equations (6.6) and (6.7) can be obtained through the evolution equation proposed by Reese and Govindjee (1998):

$$-\frac{1}{2}\mathbf{F}\,\frac{d\left[(\mathbf{C}^{\mathrm{i}})^{-1}\right]}{dt}\mathbf{F}^{\mathrm{T}} \cdot \left(\mathbf{b}^{\mathrm{e}}\right)^{-1} = \gamma^{-1} : \boldsymbol{\sigma}^{\mathrm{NEQ}}, \tag{6.8}$$

where $\mathbf{C}^{\mathrm{i}} = \left(\mathbf{F}^{\mathrm{i}}\right)^{\mathrm{T}}\mathbf{F}^{\mathrm{i}}$, $\mathbf{b}^{\mathrm{e}} = \mathbf{F}^{\mathrm{e}}\left(\mathbf{F}^{\mathrm{e}}\right)^{\mathrm{T}}$, $\boldsymbol{\sigma}^{\mathrm{NEQ}} = 2\mathbf{F}^{\mathrm{e}}\frac{\partial W^{\mathrm{NEQ}}}{\partial \mathbf{C}^{\mathrm{e}}}\left(\mathbf{F}^{\mathrm{e}}\right)^{\mathrm{T}}$, $\mathbf{C}^{\mathrm{e}} = \left(\mathbf{F}^{\mathrm{e}}\right)^{\mathrm{T}}\mathbf{F}^{\mathrm{e}}$ and γ^{-1} is an isotropic rank-four mobility tensor. Here γ^{-1} takes the form

$$\text{¥}^{-1} = \frac{1}{2\text{¦}_v}\left(\mathbf{I}^4 - \frac{1}{3}\mathbf{I}\otimes\mathbf{I}\right), \tag{6.9}$$

where η_v is the shear viscosity, $\mathbf{I}^4$ is the fourth order symmetric identity tensor and $\mathbf{I}$ is the second order identity tensor. Expanding equation (6.8) for the current case gives the inelastic stretch ratios as

$$\frac{d\lambda_1^i}{dt}=\frac{J_{\text{lim}}^{\text{NEQ}}\lambda_1^i}{6\tau\left[J_{\text{lim}}^{\text{NEQ}}-\left(\frac{\lambda_1}{\lambda_1^i}\right)^2-\left(\frac{\lambda_2}{\lambda_2^i}\right)^2-\left(\frac{\lambda_1}{\lambda_1^i}\right)^{-2}\left(\frac{\lambda_2}{\lambda_2^i}\right)^{-2}+3\right]}\left[2\left(\frac{\lambda_1}{\lambda_1^i}\right)^2-\left(\frac{\lambda_2}{\lambda_2^i}\right)^2-\left(\frac{\lambda_1\lambda_2}{\lambda_1^i\lambda_2^i}\right)^{-2}\right], \quad (6.10)$$

$$\frac{d\lambda_2^i}{dt}=\frac{J_{\text{lim}}^{\text{NEQ}}\lambda_2^i}{6\tau\left[J_{\text{lim}}^{\text{NEQ}}-\left(\frac{\lambda_1}{\lambda_1^i}\right)^2-\left(\frac{\lambda_2}{\lambda_2^i}\right)^2-\left(\frac{\lambda_1}{\lambda_1^i}\right)^{-2}\left(\frac{\lambda_2}{\lambda_2^i}\right)^{-2}+3\right]}\left[2\left(\frac{\lambda_2}{\lambda_2^i}\right)^2-\left(\frac{\lambda_1}{\lambda_1^i}\right)^2-\left(\frac{\lambda_1\lambda_2}{\lambda_1^i\lambda_2^i}\right)^{-2}\right], \quad (6.11)$$

where $\tau=\eta_v/G^{\text{NEQ}}$ is defined as the viscoelastic relaxation time. Experiments have suggested that elastomers have a wide range of multiple relaxation times. To demonstrate particular ideas, we only assumed a single relaxation time τ =1s (based on the time scale of the energy harvesting cycles) in our simulation for simplification purpose, similar to the work of Foo *et al*. (2012). It can be observed from equations (6.10) and (6.11) that the inelastic stretch ratios $\lambda_1^i(t)$ and $\lambda_2^i(t)$ of the DE membrane can be obtained if $\lambda_1(t)$ and $\lambda_2(t)$ are given. When $\lambda_1^i(t)$, $\lambda_2^i(t)$, $\lambda_1(t)$ and $\lambda_2(t)$ are known, then the tensile forces P_1 and P_2 can be obtained as a function of time t by combining equations (6.6) and (6.7). The initial conditions are $\lambda_1(0)=\lambda_2(0)=\lambda_1^i(0)=\lambda_2^i(0)=1$ without pre-stretch, or $\lambda_1(0)=\lambda_1^i(0)=\lambda_{\text{pre1}}$ and $\lambda_2(0)=\lambda_2^i(0)=\lambda_{\text{pre2}}$ with λ_{pre1} and λ_{pre2} as the pre-stretch ratios.

During the electromechanical cycles, the applied electric voltage on the DE may cause the electrical breakdown (EB) of the material, which is a typical failure mode of the dielectric elastomers when the electric field induced in the membrane exceeds its dielectric strength E_{EB}. Following Zhou *et al.* (2013), and Koh *et al.* (2011) the breakdown voltage Φ_B is determined as,

$$\frac{\text{c}_{\text{B}}}{H}\sqrt{\frac{££_0}{G}} = d\,\text{a}_1^{-1}\text{a}_2^{-1}\,, \tag{6.12}$$

where $d = E_{\text{EB}}\sqrt{££_0 / G}$ is a material parameter which may vary for different materials.[31] Such a failure mode must be avoided during the operation of the DEG. In this work, a medium value d=2 is selected for simulation purpose.

6.3 Model and formulation of viscoelastic DEGs

In this section, the model established above will be employed to analyze the complex energy harvesting mechanism of the DEG with equi-biaxial loading configuration ($\text{a}_1 = \text{a}_2 = \text{a}$, $\text{a}_1^{\text{i}} = \text{a}_2^{\text{i}} = \text{a}^{\text{i}}$), which demonstrates the highest energy density yet reported from the experimental work in the literature (Huang *et al*., 2013; Shian *et al*., 2014). My simulation results are then compared with the experiment results obtained by Huang *et al.* (2013). When the DE membrane is under (triangular) cyclic loading (see the λ variation with time in Figure 6.4), Figure 6.2 shows the four intervals of a typical energy harvesting cycle for both the voltage-stretch response curve and the charge-stretch response curve. As shown in Figure 6.2(a), in interval 1, starting from the condition when the voltage across the dielectric elastomer is at the high-voltage of the harvesting capacitor, i.e., $\text{c} = \text{c}_H = 5\text{kV}$ in this case, the membrane is then stretched at a rate of $d\text{a}/dt = 4.2$, which results in the increase of the capacitance ($C = ££_0\text{a}^4L^2/H$) and the decrease of the voltage across the DE membrane. As the stretching continues, the voltage across the DE membrane keeps decreasing until it reaches the level of the low-voltage power supply, i.e., $\text{c} = \text{c}_L = 2\text{kV}$ in this case, where the DE membrane is then connected to the power supply. In interval 2, the membrane is further stretched to the prescribed maximum stretch ratio, $\text{a}_{\text{max}} = 5.4$, during which time the charges (Q_{in}) flow from the power supply to the membrane while the voltage remains constant. During interval 3, the stretch is decreased and the DE membrane shrinks back at a rate of $-d\text{a}/dt = -4.2$. Once the DE membrane begins to shrink, its capacitance decreases. Consequently, the voltage across the DE membrane increases and the membrane is disconnected from the power supply. At the end of interval 3, the voltage across the DE membrane increases back to the level of the high-voltage of the harvesting capacitor ($c = c_H$), and the membrane is connected to the harvesting capacitor again. In interval 4, the membrane continues to recover and some charges (Q_{out}) on the DE membrane are transferred to the harvesting capacitor. The corresponding variation of the charges on the two electrodes of the DE membrane during the four intervals of the electromechanical cycle is reported in Figure 6.2(b). In fact, the starting point and the ending point of a cycle may not always be coincident due to the loss of tension of the DE. It should be mentioned that over 10 cycles are examined in our simulation and a complete cycle (cycle 6) is selected to show in Figure 6.2 for illustration purpose. This issue will be further discussed later. In this simulation, the geometrical parameters and the material constants are selected as H = 0.5 mm, L = 35 mm, mass density ° = 960 kg/m3, G = 600 kPa, ¡ = 0.5, £=3.5, $J_{\mathrm{lim}}^{\mathrm{NEQ}} = 55$, and $J_{\mathrm{lim}}^{\mathrm{EQ}} = 110$.[21, 32-34]

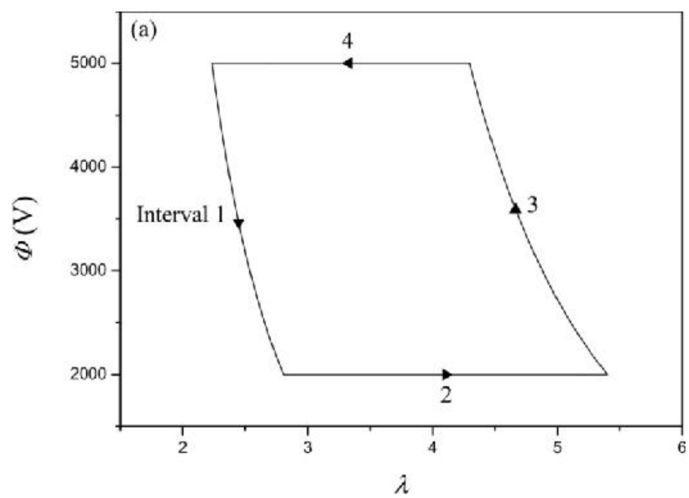

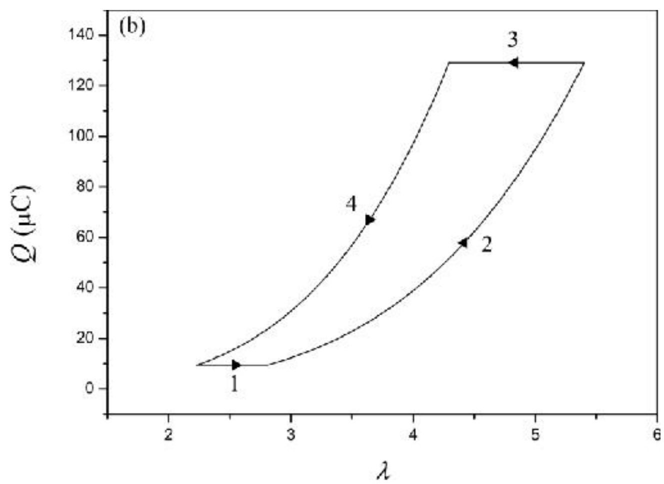

Figure 6.2 A typical energy harvesting cycle of the DEG. (a) The voltage-stretch response curve, (b) the charge-stretch response curve.

Furthermore, from the voltage-stretch response curve and the charge-stretch response curve for an energy harvesting cycle in Figure 6.2, the net electrical energy $\mathrm{a}E_e$ harvested as well as the energy density E_{D} can be obtained, i.e., $\mathrm{a}E_{\mathrm{e}} = Q_{\mathrm{out}}\mathrm{c}_{\mathrm{H}} - Q_{\mathrm{in}}\mathrm{c}_{\mathrm{L}}$ and $E_{\mathrm{D}} = \mathrm{a}E_{\mathrm{e}} / m$. As mentioned before, the harvested electrical energy is converted from the mechanical work done during the stretching-shrinking process. Therefore, to determine the harvesting efficiency of the DEG, the mechanical work also needs to be determined. Figure 6.3 depicts the equi-biaxial force P induced by stretching as a function of the displacement of the membrane L (a:-1.2) for the first two energy harvesting cycles (Note that the membrane is pre-stretched to $\mathrm{a}_{\mathrm{pre}} = 1.2$ before the first cycle). Due to the material viscous character, the force P drops to 0 (where loss of tension occurs) before the DE membrane recovers to the starting point for both cycles 1 and 2. Since the membrane cannot sustain any compression, the membrane is stretched again once P = 0. Also, during a harvesting cycle, the difference between the work done by the equi-biaxial force P on the loading path and the unloading path is the mechanical energy consumed by the membrane, which is denoted as $\mathrm{a}E_{\mathrm{m}}$. Part of the consumed energy will be converted to the electrical energy while the rest may be dissipated due to the viscous character of the material, the possible plastic deformation, and the friction in reality. Thus, the efficiency

¦ of the DEG for a single cycle is defined as $¦ = \mathrm{a}E_{\mathrm{e}} / \mathrm{a}E_{\mathrm{m}}$, which is the ratio of the electrical energy harvested to the mechanical energy consumed in the cycle.

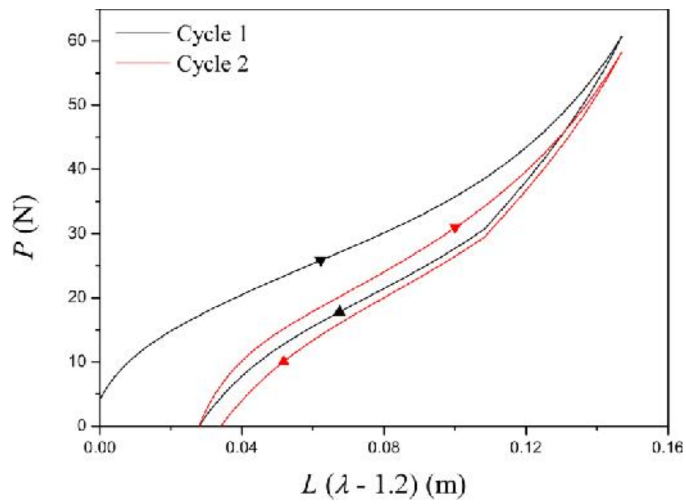

Figure 6.3 The equi-biaxial force P versus the displacement of the DE for the first two energy harvesting cycles.

From Figure 6.3, it is also noticed that the first two cycles do not overlap, which indicates that energy harvesting cycles of the DEG may not be the same at the beginning of the energy harvesting process. To investigate whether steady cycles of the DEG can be achieved as the harvesting process continues, we plot the total stretch ratio and the inelastic stretch ratio of the membrane for the first ten cycles in Figure 6.4. It is observed that the harvesting cycles become identical after a few cycles, i.e., steady energy harvesting cycles can be achieved in our simulation, which is essential for the long-term use of the DEG. This steady harvesting performance can also be validated from the variation of the energy density shown in Figure 6.5 and the variation of the efficiency depicted in figure 6 for the first ten cycles, i.e., both the energy density and the efficiency become constant as the harvesting process continues in our simulation. It is also observed that the energy density and the efficiency demonstrated in Figures 6.5 and 6.6 are higher than the experimental measurements in the work by Huang *et al.* (2013) This might be mainly due to the fact that the current leakage, the energy dissipated through the possible plastic deformation, and the friction in reality are not considered in the current simulation.

In addition, due to the particular experiment setup, loss of tension was not avoided in the work by Huang *et al.* (2013), which may also cause more energy dissipation.

As experiments suggest (Huang *et al.*, 2013), the first key factor that affects the energy density and the efficiency of the generator is the material viscosity of the DE. Figure 6.7 depicts the variation of the energy density and the efficiency as a function of the material parameter ¡ that indicates the viscosity of a DE (Note that the energy density and efficiency of a steady cycle for each ¡ value are shown in Figure 6.7). It is found that with the increase of the material viscosity, i.e., the decrease the material parameter ¡, the energy density of the DEG increases (Figure 6.7(a)). However, the efficiency does not follow a monotonic rule (Figure 6.7(b)). This non-monotonic behavior is due to the fact that the material viscosity also influences the total mechanical work consumed in addition to the energy dissipated during the energy harvesting cycle, which gives a combined effect on the efficiency of the DEG. Nevertheless, the efficiency will eventually reaches unity for pure elastic materials (when ¡ =1) since only energy dissipation due to the viscosity is considered in our modeling.

It can also be observed that the trends demonstrated in Figures 6.5 and 6.6 are in agreement with the results by Huang *et al.* (2013) for the first few cycles during the energy harvesting process. However, it is found by Huang *et al.* (2013) that the harvested energy of the DEG drops down suddenly after a few cycles, instead of becoming constant as shown in Figures 6.5 and 6.6. Since the typical failure modes of the DEG (such as electrical breakdown and loss of tension) have been taken into account in the current simulation model and they were not reported in the work of Huang *et al.* (2013) as the cause of the sudden drop of the efficiency. Therefore, the performance degradation of the DEG may be caused by a new failure mode that has not been investigated thus far. It can be clearly noticed from the work of Huang *et al.* (2013) that the current leakage dramatically increased after a few cycles. In general, the current leakage of a capacitor increases when cracks nucleate and grow in the capacitor, which was commonly observed from both ceramic-based and DE-based capacitors (Yeung *et al*., 1994; Chan *et al*., 1995; Teverovsky, 2012; Muffoletto *et al*., 2012; Gisby *et al*., 2010). In these studies, it was found that the cracks can cause current leakage, but not necessarily a short circuit unless the cracks are large to some extent. Also, when the cracks are small, they may not be easily detectable, but they are inevitable to cause current leakage. It is thus reasonable to propose that under cyclic loading condition, fatigue cracks may nucleate in the dielectric elastomer and cause current leakage of the DE, thus leading to the performance degradation of the DEG. As shown in the work by Verron and Adriyana (2008), the fatigue life of rubbers ranges from a few cycles to thousands of cycles depending on the loading conditions. In the work of Huang *et al.* (2013), the authors sought to maximize the performance of the generator with loading condition close to the mechanical and electrical limits of the elastomer, without particularly considering the lifetime of the DEG. Therefore, under this limiting loading situation, crack nucleation could occur just after a few cycles of operation. Therefore, we hypothesize that the performance degradation of the DEG in reality is attributed to the fatigue cracks that commonly happens to any rubber-like material under cyclic loading condition, which may substantially restrict the performance of the DEGs. Accordingly, the discrepancy between our simulation results and the experimental results necessitates the consideration of the fatigue failure mode in the theoretical model.

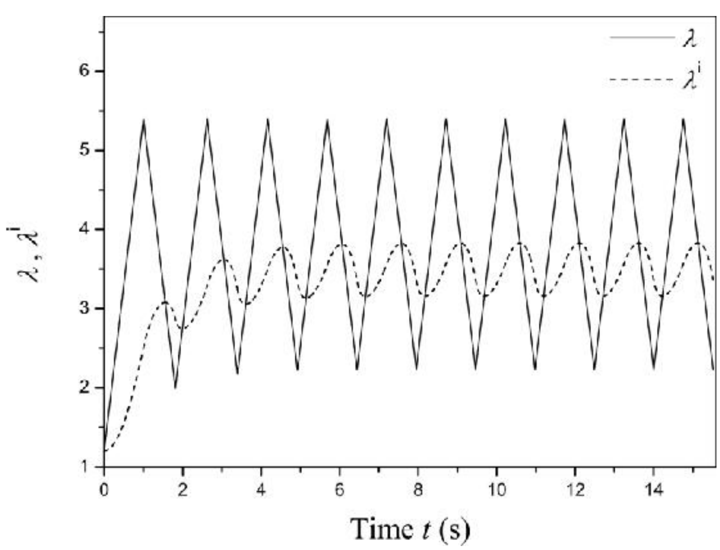

Figure 6.4 The deformation of the DE during the energy harvesting process.

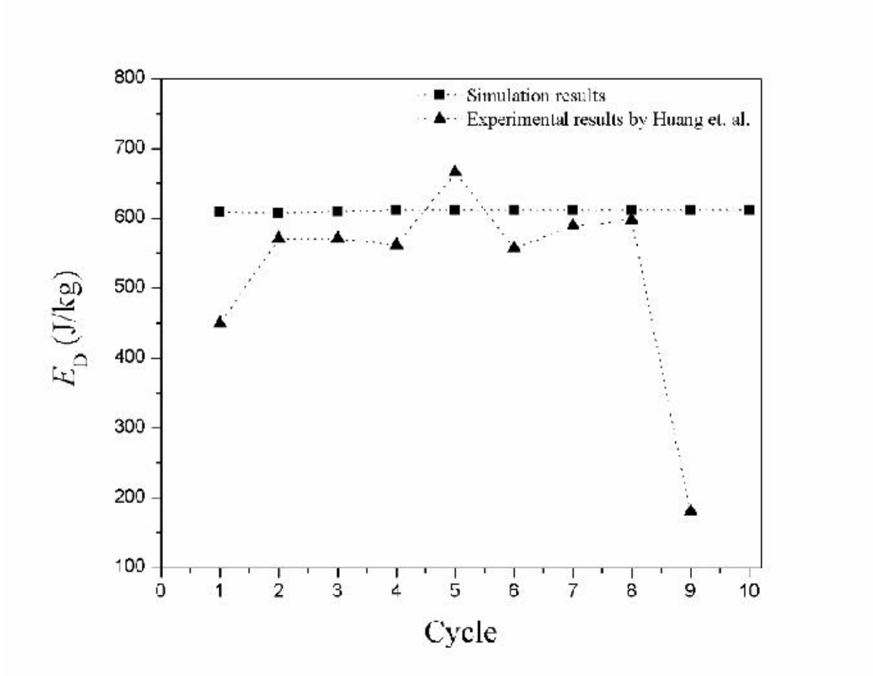

Figure 6.5 Variation of the energy density of the DEG during the energy harvesting process.

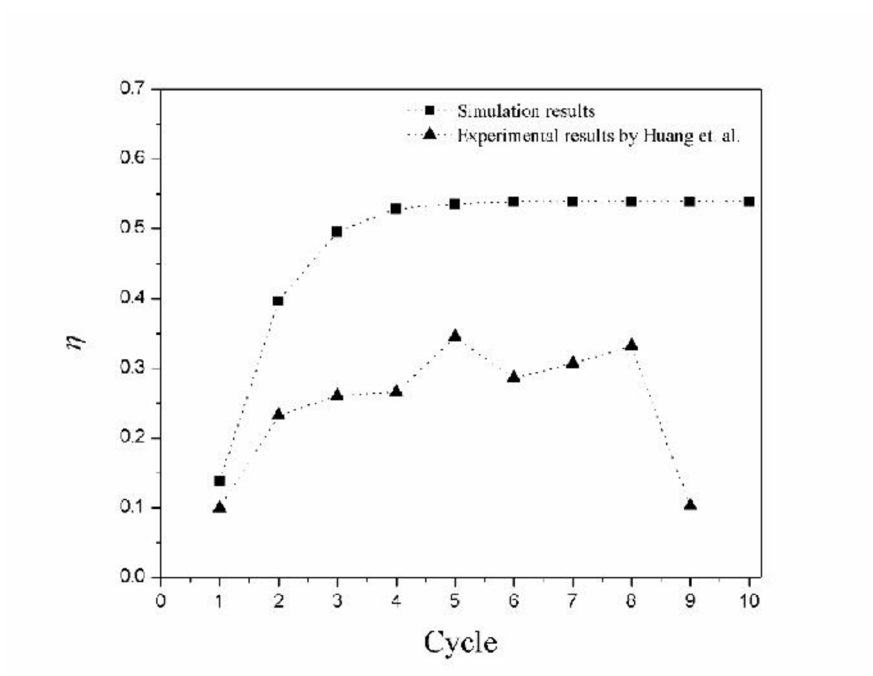

Figure 6.6 Variation of the efficiency of the DEG during the energy harvesting process.

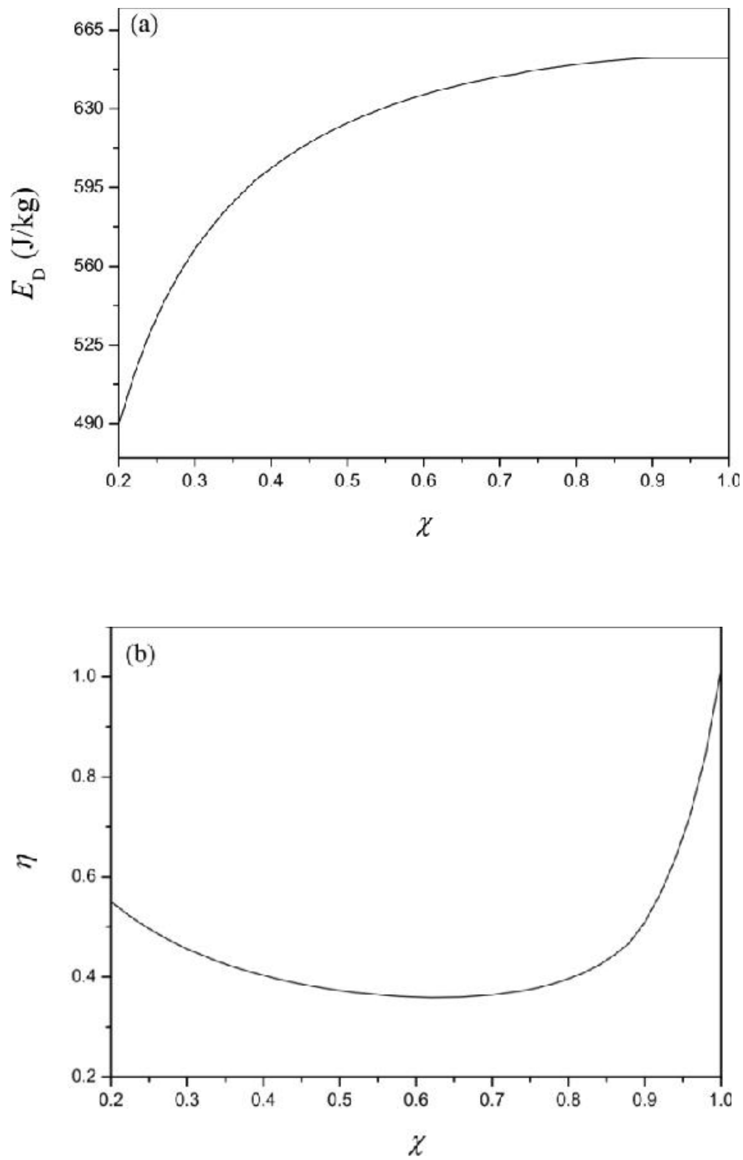

Figure 6.7 Variation of the energy density and the efficiency of the DEG as a function of ¡. (a) Energy density, (b) efficiency.

To determine the fatigue life of the DE, the crack nucleation criterion recently proposed by Verron and Adriyana (2008) is adopted in this work, in which the fatigue life (i.e., the onset of the fatigue crack nucleation) predictor for the DE is expressed as

$$\mathrm{p}^* = \left| \int_{\text{cycle}} \min\left(\left(d\mathrm{p}_{\mathrm{i}}^{\mathrm{ND}} \right)_{i=1,2,3}, 0 \right) \right|, \tag{6.13}$$

where $\left(d\mathrm{p}_{\mathrm{i}}^{\mathrm{ND}}\right)_{i=1,2,3}$ are the principal stresses of $d\boldsymbol{\Sigma}^{\mathrm{ND}}$, and

$$\boldsymbol{\Sigma}^{\mathrm{ND}} = \left[\det\left(\mathbf{F}^{\mathrm{i}}\right)\right]^{-1} W\mathbf{I} - \left(\mathbf{F}^{\mathrm{e}}\right)^{\mathrm{T}} \left[\det\left(\mathbf{F}^{\mathrm{i}}\right)\right]^{-1} \frac{\partial W}{\partial \mathbf{F}} \left(\mathbf{F}^{\mathrm{i}}\right)^{\mathrm{T}} \tag{6.14}$$

is the configurational stress tensor (or Eshelby stress tensor (Eshelby, 1975)) for a viscoelastic DE (Andriyana and Verron, 2005), which can be obtained from the deformation fields of the elastomer. Based on the concept of cracking energy density (Mars, 2002), this predictor is applicable for multiaxial loading conditions compared with the conventional fatigue crack nucleation predictors. According to the work by Verron and Adriyana (2008), the value of p^* for a steady loading cycle can be summarized as a linear function of $\ln(N_{\mathrm{f}})$, where N_{f} is the number of cycles of the fatigue life. Therefore, we assume that the predictor of the fatigue life of the DE follows

$$\mathrm{p}^* = a\ln(N_{\mathrm{f}}) + b\,, \tag{6.15}$$

where a and b depend on the material properties. As suggested by Verron and Adriyana (2008), when p^* takes a particularly small value $\mathrm{p}^* \approx 0$, the value of N_{f} is exceptionally large, which means a life-time use of the device (we assume $N_{\mathrm{f}} = 10^7$ here for example). Moreover, from the experiment results by Huang *et al.* (2013), the harvesting current starts to drop from the sixth cycle and we assume that the crack nucleation occurs at that instant. The corresponding fatigue life predictor is calculated according to equation (6.13) as $\mathrm{p}^* = 13.67MPa$ under the same loading condition as in the work of Huang *et al.* (2013). Combining the results in the works of Verron and Adriyana (2008), and Huang *et al.* (2013), a and b in equation (6.15) can be obtained, which gives

$$\mathrm{p}^* = -0.95\ln(N_{\mathrm{f}}) + 15.37 \tag{6.16}$$

for the material VH4905 studied in the work of Huang *et al.* (2013). Similarly, for other rubber-like materials, the fatigue life predictor (16) could also be determined if experimental data are available to represent the onset of the crack nucleation.

With the fatigue life taken into consideration, we can comprehensively evaluate the performance of the DEG. For a given DE membrane, the generator efficiency ¦, as observed from other works (Huang *et al*., 2013; Kaltseis *et al*., 2011; Foo *et al*., 2012), may be affected by various factors, such as the loading configuration, the maximum stretch ratio, the rate of deformation and the bias voltage. Figure 6.8 depicts the efficiency of the DEG as a function of the prescribed maximum stretch ratio a_{max} with the consideration of the possible failure modes, i.e., the loss of tension, the electrical breakdown and the fatigue life of the dielectric elastomer. The loading parameters are set as a_{pre}=1.2, $da/dt=2$, $c_L=2\text{kV}$ and $c_H=5\text{kV}$. Here, we introduce ac as the difference between the dimensionless breakdown voltage c_{EB} and the dimensionless applied voltage across the DE, i.e., $ac=(c_{EB}-c)\sqrt{££_0/(GH^2)}$ (see Figure 6.8(a)). When Δc = 0, the DE fails by the electrical breakdown. We also introduce $ap^*(N_f)$ as the difference between the value of the predictor for certain fatigue life N_f (according to equation (6.16)) and that of a steady cycle during the energy harvesting process (according to equation (6.13)), i.e., $ap^*(N_f)=p^*(N_f)-p^*$, (see Figure 6.8(b)). When $ap^*(N_f)=0$, the fatigue life of the DEG is N_f. It is observed from Figure 6.7 that the generator efficiency could be improved with the increase of the maximum stretch ratio. However, the maximum stretch ratio that could be applied to the DEG is limited by both the electrical breakdown and the fatigue failure modes of the dielectric elastomer. For example, under the current loading condition, the maximum applied stretching ratio is determined as 6.7 in Figure 6.8(a) when only the electrical breakdown is accounted for. Accordingly, the maximum efficiency of the DEG could reach up to about 48%. However, the performance of the DEG is further compromised by considering the fatigue failure of the dielectric elastomer as shown in Figure 6.8(b). It is observed that with the increase of the fatigue life expectancy, both the applicable maximum stretch ratio and the efficiency of the DEG decrease. For example, if the DEG is designed with a fatigue life expectancy of $N_f = 10^5$ for example, the maximum efficiency of the DEG is approximately 25% at $\lambda_{max} = 3.65$. However, with the decrease of the fatigue life expectancy to $N_f = 10$, the DEG efficiency could reach up to 35% with a maximum stretch ratio $\lambda_{max} = 5.2$. It is thus concluded that the DEG performance is limited by all these possible failure modes of the dielectric elastomer, which must be incorporated in the modeling and the optimal design of the DEGs.

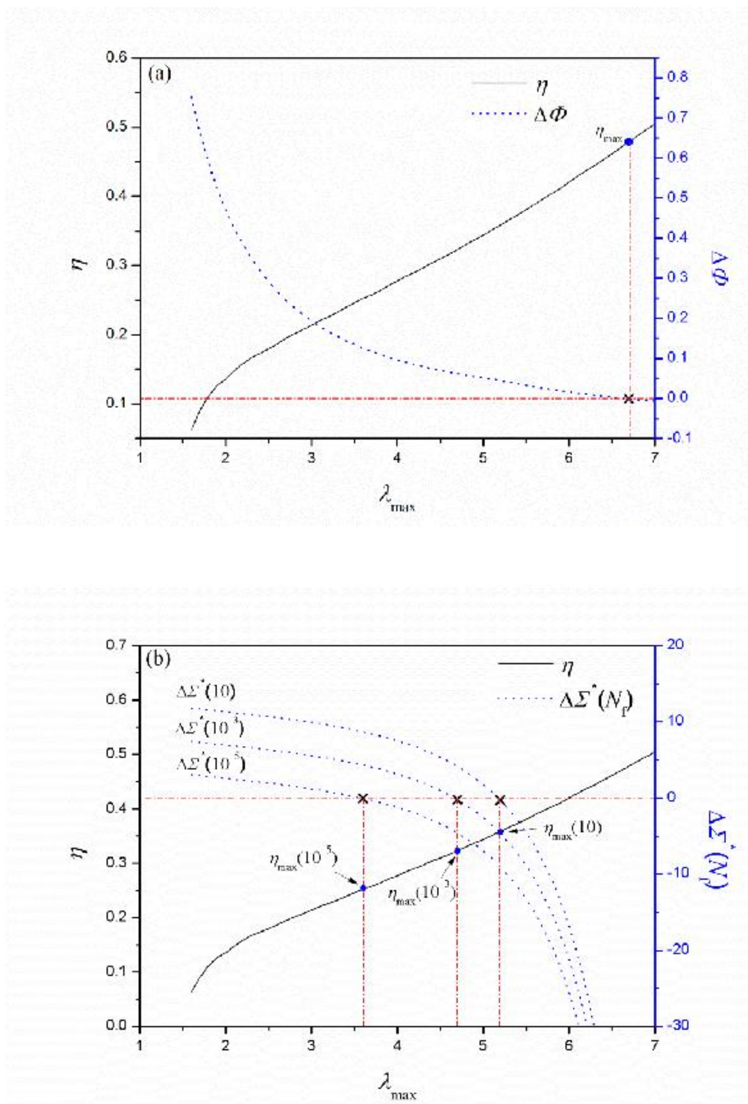

Figure 6.8 Effect of the pre-determined maximum stretch λ_{max} on the efficiency. (a) Considering the electrical breakdown failure, (b) considering the fatigue life of the DE.

Along with the maximum stretch ratio a_{max}, the rate of deformation $d a / dt$ also affects the efficiency of the DEG. Figure 6.9 attempts to demonstrate the trend of the efficiency change with the maximum stretch ratios and the rates of deformation without explicitly considering the lifetime of the DEG. However, the other possible failure modes, i.e., the loss of tension and the electrical breakdown are all avoided in the simulation process. The other loading parameters are set as a_{pre}=1.2, $c_L = 2\text{kV}$ and $c_H = 5\text{kV}$. It is observed from Figure 6.9 that for any fixed rate of deformation, the efficiency of the DEG rises when the maximum stretch ratio increases, which is also demonstrated in Figure 6.8. The reason behind this is mainly linked to the well-boosted harvested electrical energy as a_{max} is increased, since the capacitance C is proportional to a^4. However, for a fixed maximum stretching ratio a_{max}, the efficiency drops to a minimum then rises up with the increase of the rate of deformation. The rate of deformation affects the efficiency mainly through its effect on the inelastic deformation of the DE, which governs the energy dissipation and changes the stiffness of the DE during the electromechanical cycles. The efficiency trend in Figure 6.9 as a function of the rate of deformation is an outcome of the combined effects of the rate of deformation on the dissipated energy and the mechanical work consumed. Therefore, when optimizing the performance of the DEGs, both the maximum prescribed stretching ratio and the rate of deformation are significant factors need to be considered. In order to consider the fatigue life of the DEG, Figure 6.10 depicts $ap^*\left(10^5\right)$ as a function of the maximum stretch ratio a_{max} and the rate of deformation $d a / dt$. Here, the DEG is designed to have a particular life expectancy, i.e., $N_f = 10^5$. It is found that the fatigue life of the DEG is dominated by the maximum stretch ratio while the change of the rate of deformation only exerts slight effect on the fatigue life. When a_{max} takes a small value, $ap^*\left(10^5\right) > 0$ regardless of the value of the rate of deformation, implying that the DEG has an expected fatigue life of 10^5 cycles no matter what the rate of deformation is used. Combining Figures 6.9 and 6.10, theoretically, the efficiency can be improved to large extend with an exceptional high rate of deformation without compromising the fatigue life requirement. However, how to realize such a high rate of deformation may be very challenging in realistic applications.

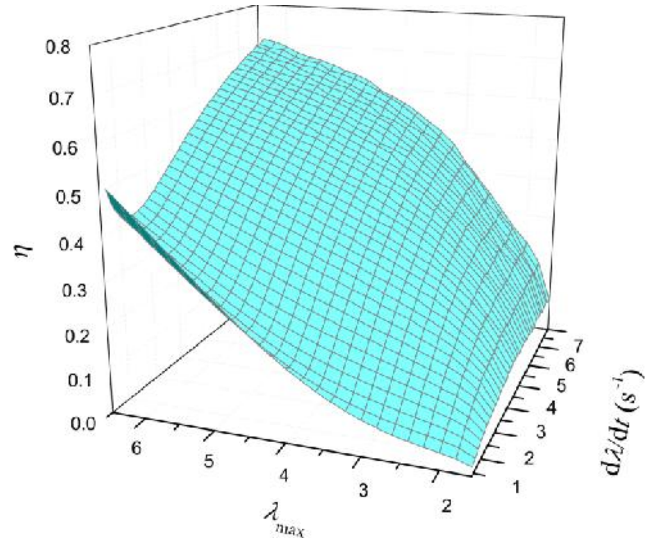

Figure 6.9 Effect of the rate of deformation and the maximum stretch ratio on the efficiency

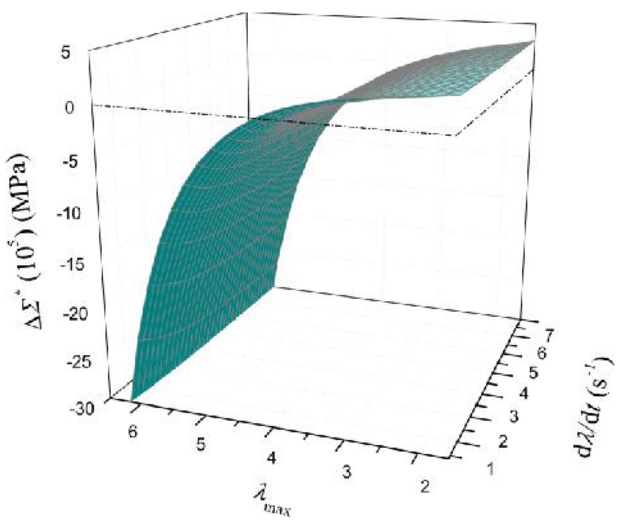

Figure 6.10 Fatigue life consideration of the DEG as a function of the rate of deformation and the maximum stretch ratio ($N_{\mathrm{f}} = 10^5$).

Another factor that may affect the efficiency of the DEG is the bias voltage, namely c_L and c_H. Without considering the lifetime of the DEG, Figure 6.11 illustrates the change of the efficiency for different values of c_L and c_H, in which the other loading parameters are set as $d a / dt = 2$, $a_{max} = 3.5$ and a_{pre}=1.2. In our simulation, it is ensured that the generator is under the loading within the safe range that loss of tension and electrical breakdown does not occur. Overall, the efficiency rises with the increase of c_L and c_H. However, when c_L is relatively low (say c_L = 1kV), the efficiency slightly rises and drops as c_H is increased. Also, when c_H takes a relative low value (say c_H = 6kV), the efficiency rises to a peak and then drops down as c_L is increased. As for the fatigue life, Figure 6.12 depicts $ap^*\left(10^5\right)$ as a function of c_L and c_H. It is observed that the fatigue life of the DEG is mainly determined by c_L. When c_L increases, the fatigue life is shortened, while only slight change of the fatigue life is observed when c_H increases with a fixed c_L. Combining the results shown in Figures 6.9 and 6.11, it is concluded that the higher efficiency of the DEG could be achieved by increasing the prescribed maximum stretch ratio and choosing proper bias voltages. However, when comparing Figures 6.10 and 6.12, it is found that choosing proper bias voltage appears to be a more desirable method to improve the efficiency, since it does not significantly shorten the fatigue life of the device.

It should be mentioned that I aim to conduct a comprehensive study to theoretically evaluate the performance of a dielectric elastomer membrane generator in the current work. Based on the viscoelasticity theory and the hypothesis on fatigue failure of the dielectric elastomers, the simulation results are in a similar trend as observed in the experimental work and could interpret some experimental scenarios. Therefore, the current modeling work could be claimed to offer useful guidance for the design and optimization of the DEGs. However, further experimental validation, particularly the fatigue testing of dielectric elastomers, is a future concentration. In addition, the characterization of the material properties, such as the viscosity and the material extensibility, will also benefit the quantitative evaluation on the performance of the DEGs.

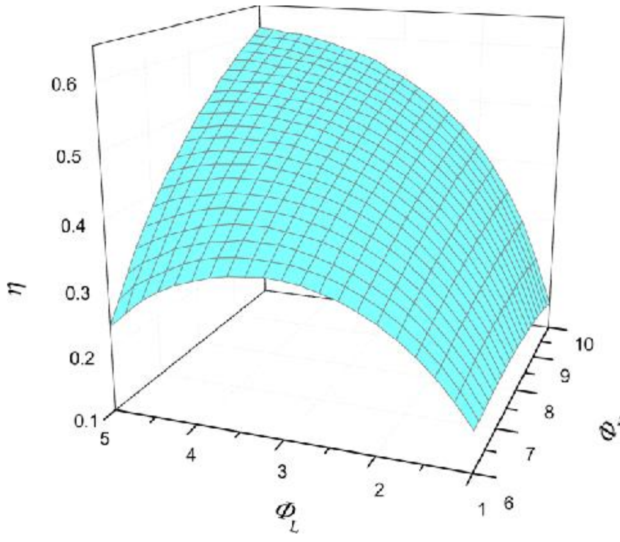

Figure 6.11 Effect of the bias voltage on the efficiency.

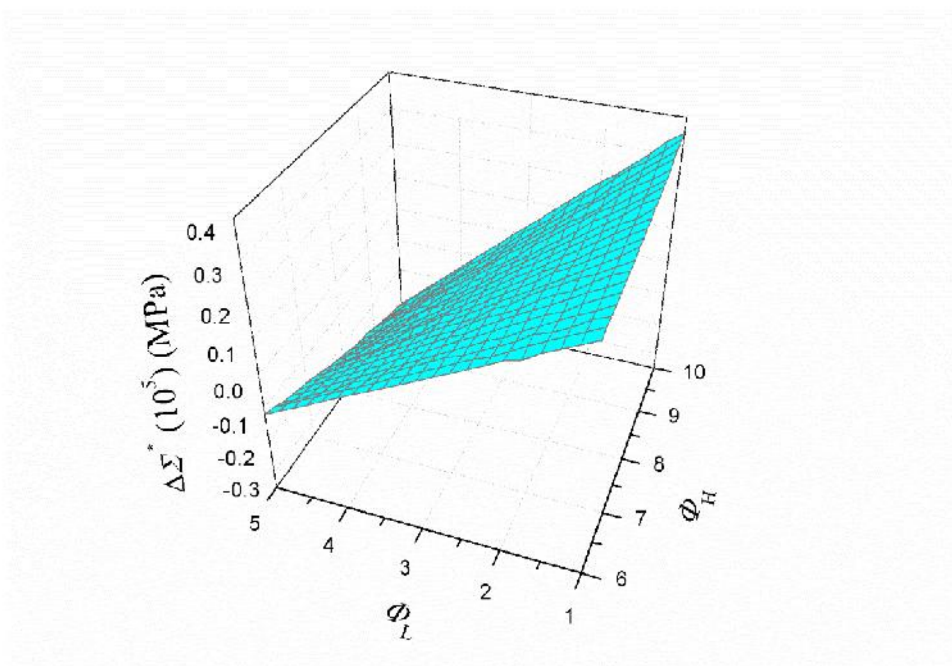

Figure 6.12 Fatigue life consideration of the DEG as a function of the bias voltage. ($N_f = 10^5$).

6.4 Conclusions

Based on the finite-deformation viscoelasticity theory for dielectric elastomers, this work investigates the energy harvesting performance of a dielectric elastomer membrane generator under equi-biaxial loading condition. By comparing our simulation results with the experimental results in the work of Huang *et al*. (2013) and considering the possible failure modes and extreme loading condition in their experiment, I propose a hypothesis that the sudden degradation of the performance of the DEG in the work of Huang *et al*. (2013) is linked to the early onset of the fatigue cracks. Furthermore, in addition to the typical failure modes that may occur during the energy harvesting cycles, such as electrical breakdown and loss of tension which are commonly incorporated in the literature, this work first considers the fatigue life of the DE-based devices under cyclic loading. The simulation results in the current work conclude that the efficiency of the DEG can be improved by increasing the rate of deformation and the maximum stretch ratio, and choosing a proper bias voltage. However, the fatigue life expectancy of the device compromises the performance of the DEG, i.e., higher fatigue life expectancy results in a lower efficiency of the DEG. It is also found that choosing proper bias voltages can largely improve the efficiency without significantly shortening the fatigue life of the DEG. This work is expected to provide a general approach for comprehensively evaluating the performance of the DEGs, as well as guidance on optimal design of the DEGs.

References

3M VHB^{TM} tape specialty tapes technical data, 2014.

Andriyana, A. and Verron, E., Effect of the hysteretic response of elastomers on the fatigue life. *Constitutive Models for Rubber IV: Proceedings of the fourth European Conference on Constitutive Models for Rubber*, ed P. Austrell and L. Kari, CRC Press, Stockholm, Sweden, pp 31-36.

Bergstrom, J. S. and Boyce, M. C., 1998. Constitutive modeling of the large strain time-dependent behavior of elastomers. J. Mech. Phys. Solids **46**, 931–954.

Carpi, F., Rossi, D. D., Kornbluh, R., Pelrine, R. and Sommer-Larsen, P., 2008. Dielectric Elatomers as Electromechanical Transducers. Elsevier, Amsterdam.

Chan, Y. C., Wang, Y., Gui Z. L. and Li, L. T., 1995. Thermal effects on the dielectric and electrical properties of relaxor ferroelectric ceramic-based MLCs. *Electronic Manufacturing Technology Symposium, Proceedings of 1995 Japan International, 18th IEEE/CPMT international*, 328-333.

Chiba, S., Waki, M., Kornbluh, R. and Pelrine, R., 2011. Current status and future prospects of power generators using dielectric elastomers. *Smart Mater. Struct*. **20**, 124006.

Eshelby, J. D., 1975. The elastic energy-momentum tensor. *J. Elasticity* **5**, 321-335.

Foo, C. C., Koh, S. J. A., Keplinger, C., Kaltseis, R., Bauer, S. and Suo, Z., 2012a. Performance of dissipative dielectric elastomer generators. J. Appl. Phys. **111**, 094107.

Foo, C. C., Cai, S., Koh, S. J. A., Bauer, S. and Suo, Z., 2012b. Model of dissipative dielectric elastomers. J. Appl. Phys. **111**, 034102.

Gent, A. N., 1996. A new constitutive relation for rubber. Rubber Chem. Technol. **69**, 59-61.

Gisby, T. A., Xie, S. Q., Calius E. P. and Anderson, I. A., 2010. Leakage current as a predictor of failure in dielectric elastomer actuators. *Proc. of SPIE* **7642**, 764213.

Hoffstadt, T., Graf, C. and Maas, J., 2013. Optimization of the energy harvesting control for dielectric elastomer generators. *Smart Mater. Struct*. **22**, 094028.

Hong, W., 2011. Modeling viscoelastic dielectrics. J. Mech. Phys. Solids **59**, 637-650.

Huang, J., Shian, S., Diebold, R. M., Suo, Z. and Clarke, D. R., 2012. The thickness and stretch dependence of the electrical breakdown strength of an acrylic dielectric elastomer. *Appl. Phys. Lett*. **101**, 122905.

Huang, J., Shian, S., Suo, Z. and Clarke, D. R., 2013. Maximizing the energy density of dielectric elastomer generators using equi-biaxial laoding. Adv. Funct. Mater. **23**, 5056-5061.

Huang, R. and Suo, Z., 2011. Electromechanical phase transition in dielectric elastomers. Proc. R. Soc. A **468**, 1014–1040.

Jean, P., Wattez, A., Ardoise, G., Melis, C., Van Kessel, R., Fourmon, A., Barrabino, E., Heemskerk, J. and Queau, J. P., 2012. Standing wave tuve electro active polymer wave energy converter. *Proc. of SPIE* **8340**, 83400C.

Jean-Mistral, C., Basrour, S. and Chaillout, J., 2008. Dielectric polymer: scavenging energy from human motion. *Proc. of SPIE* **6927**, 692716.

Jean-Mistral, C., Vu Cong T. and Sylvestre, A., 2012. Advances for dielectric elastomer generators: replacement of high voltage supply by electret *Appl. Phys. Lett*. **101**, 162901.

Kaltseis, R., Keplinger, C., Baumgartner, R., Kaltenbrunner, M., Li, T., Machler, P., Schwodiauer, R., Suo Z. and Bauer, S., 2011. Method for measuring energy generation and efficiency of dielectric elastomer generators. *Appl. Phys. Lett*. **99**, 162904.

Koh, S. J. A., Keplinger, C., Li, T., Bauer S. and Suo, Z., 2011. Dielectric elastomer generators: how much energy ban be converted? *IEEE-ASME T. Mech*. **16**, 33-41.

Koh, S. J. A., Li, T., Zhou, J., Zhao, X., Hong, W., Zhu, J. and Suo, Z., 2011. Mechanisms of large actuation strain in dielectric elastomers. J. Polym. Sci. B **49**, 504–515.

Koh, S. J. A., Zhao X. and Suo, S., 2009. Maximal energy that can be converted by a dielectric elastomer generator. *Appl. Phys. Lett*. **94**, 262902.

Kornbluh, R. D., Pelrine, R., Prahlad, H., Wong-Foy, A., McCoy, B., Kim, S., Eckerle, J. and Low, T., 2012. Dielectric elastomers: stretching the capabilities of energy harvesting. *MRS Bull.* **37**, 246-253.

Li, T., Qu, S. and Yang, W., 2012. Energy harvesting of dielectric elastomer generators concerning inhomogeneous fields and viscoelastic deformation. J. Appl. Phys. **112**, 034119.

Mars, W. V., 2002. Cracking energy density as a predictor of fatigue life under multiaxial conditions. *Rubber Chem. Technol*. **75**, 1-17.

McKay, T. G., O'Brien, B. M., Calius E. P. and Anderson, I. A., 2011. Soft generators using dielectric elastomer. *Appl. Phys. Lett*. **98**, 142903.

McKay, T. G., O'Brien, B. M., Calius E. P. and Anderson, I. A., 2010b. Self-priming dielectric elastomer generators. *Smart Mater. Struct*. **19**, 055025.

McKay, T., O'Brien, B., Calius, E. and Anderson, I., 2010a. An integrated, self-priming dielectric elastomer generator. Appl. Phys. Lett. **97**, 062911.

Muffoletto, D. P., Burke K. M. and Zirnheld, J. L., Partial discharge analysis of prestretched and unstretched acrylic elastomers for dielectric elastomer actuators (dea). *Proc. of SPIE* **8340**, 834021.

Park, H. S. and Nguyen, T. D., 2013. Viscoelastic effects on electromechanical instabilities in dielectric elastomers. Soft Matter **9**, 1031-1042.

Pelrine, R., Kornbluh, R. D., Eckerle, J., Jeuck, P., Oh, S., Pei, Q. and Stanford, S., 2001. Dielectric elastomers: generator mode fundamentals and applications. Proc. SPIE **4329**, 148-156.

Pelrine, R., Kornbluh, R., Pei, Q. and Joseph, J., 2000. High-speed electrically actuated elastomers with greater than 100%. Science **287**, 836-839.

Reese, S. and Govindjee, S., 1998. A theory of finite viscoelasticity and numerical aspects. Int. J. Solids Struct. **35**, 3455-3482.

Shian, S., Huang, J., Zhu, S. and Clarke, D. R., 2014. Optimizing the electrical energy conversion cycle of dielectric elastomer generators. Adv. Mater. **26**, 6617-6621.

Suo, Z., Zhao, X. and Greene, W. H., 2008. A nonlinear field theory of deformable dielectrics. J. Mech. Phys. Solids **56**, 467–486.

Teverovsky, A., 2012. Breakdown voltages in ceramic capacitors with cracks. *IEEE Transactions on Dielectrics and Electrical Insulation* **19**, 1448-1455.

Verron E. and Andriyana, A., 2008. Definition of a new predictor for multiaxial fatigue crack nucleation in rubber. *J. Mech. Phys. Solids* **56**, 417-443.

Wang, J., Nguyen, T. D. and Park, H. S., 2014. Electrostatically driven creep inviscoelastic dielectric elastomers. *J. Appl. Mech.* **81**, 213508.

Yeung, F., Chan, Y. C., Wang, Y., Gui Z. L. and Li, L. T., 1994. Thermal shock resistance of miniaturized multilayer ceramic capacitors. *J Mater Sci: Mater Electron* **5**, 339-343.

Zhao, X. and Suo, Z., 2007. Method to analyze electromechanical stability of dielectric elastomers. Appl. Phys. Lett. **91**, 061921.

Zhou, J., Jiang, L. and Khayat, R. E., 2013. Failure analysis of a dielectric elastomer plate actuator considering boundary constraints. J. Intell. Mater. Syst. Struct. **24**, 1667–1674.

Zhou, J., Jiang, L. and Khayat, R. E., 2014. Viscoelastic effects on frequency tuning of a dielectric elastomer membrane resonator. J. Appl. Phys. **115**, 124106.

Chapter 7

7 Conclusions and future work

7.1 Conclusions

Compared with conventional smart materials in actuation (piezoelectric crystals and ceramics for example) which are known for their high load capacity and small deformation, dielectric elastomers are characterized by their softness, flexibility and large deformation capability. These properties make dielectric elastomers an interesting alternative to conventional technologies in transduction. In order to make full potential applications of these soft matters with reliable design, it is necessary to have a better understanding on their electromechanical coupling behavior. However, modeling the electromechanical coupling of dielectric elastomers is challenging due to their large deformation, nonlinear material behavior, diverse failure modes and geometric configurations. Moreover, the effects of the material viscoelasticity on the actuation, dynamic and energy harvesting performance of DEs are also rather complicated to understand. With particular considerations of these material properties and the typical failure modes of DEs, this work developed theoretical models to tackle the as-mentioned challenges for the application of DE transducers and provided guidelines for their optimal design. The contributions of this thesis include:

1. Based on the Gent hyperelastic model, this work investigated the electromechanical response and the typical failure modes of a DE plate actuator and a DE tube actuator. By studying the complex interplay among the electromechanical response, the electrical breakdown failure and the electromechanical instability, a boundary-constraint method was proposed to eliminate EMI during the voltage-control actuation process and improve the voltage-induced deformation of the actuators. Moreover, the possible mechanical buckling failure caused by the boundary constraints was also examined.

2. Adopting the finite-deformation viscoelasticity theory for dielectric elastomers, this work studied the in-plane oscillation and the natural frequency tuning of a viscoelastic DE membrane resonator. To demonstrate the effects of the material viscoelasticity, comparisons of the frequency tuning process, the tunable frequency range and the safe operation voltage range between a resonator with a viscoelastic membrane and a purely elastic membrane was presented. In addition, the influence of the electrical loading rate on the frequency tuning and the tuned frequency of the resonator was also examined.

3. With the finite-deformation viscoelasticity model, this work also investigated the energy harvesting performance of a viscoelastic DE membrane generator with an equi-biaxial loading configuration. By examining the consumed mechanical energy and harvested electrical energy, possible avenues to improve the energy conversion efficiency of viscoelastic DE generators were uncovered. To reveal the mechanisms behind the current leakage phenomenon of DE generators, the fatigue life of the DE-based devices under cyclic loading was considered for the first time in the literature.

Based on our modeling work and simulation results, some concluding remarks of this work are listed below:

1. The comparison of the electromechanical response between constrained and unconstrained DE actuators shows that applying boundary constraints to the DE actuator can eliminate the electromechanical instability and improve the actuation deformation. This boundary-constraint method is theoretically verified on a DE plate actuator and a DE tube actuator.

2. For viscoelastic DE oscillators and resonators, their dynamic performance is strongly influenced by the material viscoelasticity and neglecting the viscoelastic effects can lead to substantial error in determining the natural frequency of DE-based vibration devices.

3. Our simulation results show that the natural frequency of a viscoelastic DE membrane resonator is governed by the applied voltage, the total deformation and the inelastic deformation, and thus time-dependent.

4. It is also found that the electrical loading rate affects the tunable frequency range and the safe operation voltage range of viscoelastic DE resonators. However, tuned natural frequency does not vary with the electrical loading rate when the voltage level is within the safe range.

5. For viscoelastic DE generators for energy harvesting, their energy conversion efficiency can be improved by increasing the maximum stretch ratio and the rate of deformation, and choosing an optimized bias voltage.

6. It is also concluded that the fatigue life expectancy of the DE generators compromises their energy conversion efficiency. In other words, extending the fatigue life of the DE generators is at the cost of their energy conversion efficiency.

7.2 Future work

This work presents a general methodology to improve the actuation deformation of DE actuators and develops models to investigate the dynamic and energy harvesting performance of DE resonators and generators. The modeling work and simulation results are expected to be helpful for predicting the performance of these DE-based devices and benefit their optimal design. However, there also exist some limitation of the developed model and some other aspects of DE-based devices to be further studied. Consequently, some suggestions for our future work are offered below:

1. Further considerations need to be given to the electrical breakdown failure, which is a typical failure mode for all DEs and strongly depends on the dielectric strength of the material. Like most of the theoretical works on DEs in the literature, we assumed a constant dielectric strength in our models in this work, whereas experiments suggest that the dielectric strength of DEs changes with several factors such as the stretch ratios, the thickness and the temperature. Therefore, it will be essential to

develop a theoretical model with the consideration of the dependence of the dielectric strength on these factors and combine it with our recent models to provide more accurate predictions on the performance of DE-based devices.

2. For DE generators, experimental work has shown that their performance can be improved not only by the loading parameters but also by using an alternative loading path. In the current work, the “rectangular” loading path has been examined by mathematical modeling, while other possible loading paths (the “triangular” loading path, for example) can be further explored in the future work. It is thus can provide a guidance on choosing an optimal loading condition for improving the mechanical-electrical conversion efficiency of DE generators.

3. Due to the material viscoelasticity, loss-of-tension of DEs may occur under cyclic loading condition, which can make the DE wrinkle and difficult to control. Dielectric elastomer composites (dielectric elastomers with reinforced stiff fibers for example) may be a solution to this issue and pave the way to more controllable DE-based devices. Further theoretical study may be pursued to model the performance of DE composites-based devices for better controllable performance.

4. The tunable waveguide is another recent application of DEs in dynamics. With the application of the voltage, the range of the filtering frequencies of a DE waveguide can be actively tuned. Although this recent application of DEs is very promising, very few studies on investigating the DE waveguides exist in the literature, particularly with the consideration of the material viscoelasticity that may also significantly influence their performance. In order to offer guidelines for the development and design of DE waveguides, it is essential to first develop models incorporating the material viscoelasticity to describe the electroelastic wave propagation in deformed DEs.

Curriculum Vitae

Name:	Jianyou Zhou
Post-secondary Education and Degrees:	South China University of Technology Guangzhou, Guangdong, China 2006-2010 B.Eng.
	The University of Western Ontario London, Ontario, Canada 2010-2011 M.Eng. 2011-2015 Ph.D.
Honours and Awards:	Western Graduate Research Scholarship 2011-2015
Related Work Experience	Teaching Assistant/Research Assistant The University of Western Ontario 20011–2015

Publications:

1. Zhou, J., Jiang, L. and Khayat, R. E. (2015). Dynamic analysis of a tunable viscoelastic dielectric elastomer oscillator under external excitation. Submitted to *Smart Materials and Structures*.

2. Zhou, J., Jiang, L. and Khayat, R. E. (2015). Investigation on the performance of a viscoelastic dielectric elastomer membrane generator. *Soft Matter*. 11: 2983-2992

3. Zhou, J., Jiang, L. and Khayat, R. E. (2014). Viscoelastic effects on frequency tuning of a dielectric elastomer membrane resonator. *Journal of Applied Physics*. 115: 124106.

4. Zhou, J., Jiang, L. and Khayat, R. E. (2014). Electromechanical response and failure modes of a dielectric elastomer tube actuator with boundary constraints. *Smart Materials and Structures*. 23: 045028.

5. Zhou, J., Jiang, L. and Khayat, R. E. (2013). Failure analysis of a dielectric elastomer plate actuator considering boundary constraints. *Journal of Intelligent Material Systems and Structures*. 24: 1667-1674.

6. Zhou, J., Jiang, L. and Khayat, R. E., Dynamic analyses of a viscoelastic dielectric elastomer oscillator. Proceedings of the 25th Canadian Congress of Applied Mechanics, London, Canada, May 31-June 4, 2015.

7. Zhou, J., Jiang, L. and Khayat, R. E., Frequency tuning of a viscoelastic dielectric elastomer (DE) membrane resonator, 17th U.S. National Congress on Theoretical and Applied Mechanics, Michigan State University, East Lansing, USA, June 2014.

8. Zhou, J., Jiang, L.Y. and Khayat, R. E., Electromechanical response and instability of dielectric elastomer actuators, Proceedings of The Canadian Society for Mechanical Engineering International Congress 2014, Toronto, Canada, June 1-4, 2014.